Using Umbrella Integration to Find Minimum Free Energy Paths

Von der Fakultät Chemie der Universität Stuttgart zur Erlangung der Würde eines Doktors der Naturwissenschaften (Dr. rer. nat.) genehmigte Abhandlung

Vorgelegt von

Matthias Ulrich Bohner

aus Geislingen an der Steige

Hauptberichter	Prof. Dr. Johannes Kästner
Mitberichter	Prof. Dr. Bernd Engels
Prüfungsvorsitzender	Prof. Dr. Joris van Slageren
Tag der Mündlichen Prüfung:	4. Dezember 2014

Institut für Theoretische Chemie
Universität Stuttgart

2015

CONTENTS

Abstract:

The analysis of the detailed mechanism of chemical reactions is a key task of computational chemistry. The detailed knowledge may help to improve known processes or even contribute to the development of new ones. In this way ecological and economic demands can be reduced. Furthermore, the course of a reaction path also plays an important role in the action of drugs. Understanding the binding of the active ingredient to receptors, such as proteins, can make it possible to optimize drugs by reducing side effects, or even to find new effects. Unfortunately, chemical reactions are usually too fast to observe intermediate states by experimental methods. This is where theoretical chemistry joins the game.

In theoretical chemistry we combine the coordinates of all atoms with the configuration space. The potential energy forms a hypersurface in this space. Minima represent stable or metastable states. Saddle points represent transition states which are the most unfavourable configurations occurring on the most favourable path between two minima. If the path of a reaction is known, all intermediate states can be observed by theoretical methods. However, these calculations are usually computationally costly. This is the reason why, in contrast to experimental methods, it is in general impossible to sample the whole configuration space. This would in most cases exceed the available computational resources. It is therefore necessary to use techniques enabling a reaction path to be found without sampling the whole configuration space.

In the case of a thermodynamic ensemble, e. g. the contents of a test tube, statistical information has to be included. The corresponding potential is the so-called free energy landscape, for which some degrees of freedom of the configuration space are thermostatistically integrated out. Consequently this function includes statistical and energetic properties. The free energy can in general only be calculated by statistical simulations (Monte–Carlo or molecular dynamics). Unfortunately, the transition states in which we have a special interest are rarely sampled. Special methods have to be applied to get sufficient sampling as well in areas of these rare events.

In this work a non-physical quadratic potential is used to bias the equation of motion of the particles while doing molecular dynamics simulations. In this way unfavourable areas in the configuration space can also be sampled sufficiently. This technique is called *umbrella sampling*. The bias is applied to one or more coordinates which describe the reaction and therefore are called reaction coordinates. An umbrella sampling run will result in a distribution of the reaction coordinates. The expectation value of this distribution will be located close to the minimum of the bias function without in general corresponding to it. The difference between the minimum of the bias function and the expectation value can be used to calculate the gradient of the underlying free energy surface. Similarly, the covariance of the distribution of the reaction coordinate can be used to calculate the Hessian of the free energy surface. This method of interpreting the data gained by umbrella sampling is called *umbrella integration*.

At first these values are used for an iterative search of the saddle points, which represent the transition states. From these configurations, free energy paths can be constructed by following the gradient down to the minima. This algorithm was successfully tested for the alanine dipeptide system.

This simple method has the disadvantages that it works serially and that one needs good initial guesses for the saddle points in order to find them. Therefore, in a second part of the work, the established method of nudged elastic band optimization (NEB) is extended for use in the free energy surface. NEB optimization searches for a reaction path. This path is discretized into a number configurations, so-called images. For the sake of equal distribution of the images along the path a non-physical spring force between the images is used. The force, which is actually minimized during the NEB optimisation, consists of the projection of the real force of the underlying potential perpendicular to the path, and the projection of the spring force parallel to the path.

An optimizer is developed which archives quadratic convergence of NEB optimizations in the noise-free potential energy surface of some test systems. This optimiser uses gradients and Hessians at each step. For the free energy surface both values can be calculated by umbrella integration as mentioned above. NEB optimizations within the free energy are performed in this work in the following way: at first a guess path is assumed, e. g. a straight line between two points in the configuration space, usually minima. This path is discretized into a number of images. Molecular dynamics umbrella sampling simulations are performed on each image. The gradient and Hessian from the umbrella integration are fed into the newly developed NEB optimizer. This way one does not need good starting guesses for the saddle points but an interpolation between the much more easily accessible minima is sufficient. Furthermore, the need for independent molecular dynamics runs at each image makes the method intrinsically parallel. The whole method is applied to the well-studied alanine dipeptide system and compared with the results from the serial method. Subsequently the algorithm is applied to a much more costly system of binding a ligand to its receptor in water.

Zusammenfassung:

Die genaue Analyse von chemischen Reaktionen ist eine der Schlüsselaufgaben in der theoretischen Chemie. Das Wissen, das dabei gewonnen wird, hilft bekannte Prozesse zu verbessern oder neue Prozesse zu entwickeln und somit die ökologischen und ökonomischen Kosten zu reduzieren. Darüber hinaus spielt der Verlauf von Reaktionspfaden auch eine entscheidende Rolle für die Wirkung von Medikamenten. Durch das genaue Verständnis der Bindungsvorgänge der Wirkstoffe mit Proteinen können Wirkungen optimiert, Nebenwirkungen reduziert oder sogar neue Wirkmechanismen gefunden werden. Leider laufen die meisten Reaktion mit hohen Geschwindigkeiten ab, so dass es oft nicht möglich ist, genaue Informationen über Zwischenzustände aus experimentellen Daten zu erhalten. Diese Lücke wird von chemischen Simulationen geschlossen.

In der theoretischen Chemie fasst man die Gesamtheit aller Kernkoordinaten im so genannten Konfigurationsraum zusammen. Die potentielle Energie bildet eine Hyperfläche in diesem Raum. Minima stellen stabile oder metastabilen Zustände dar, die über längere Zeit existieren können. Sattelpunkte repräsentieren Übergangszustände, die die energetisch ungünstigste Konfiguration auf einem Weg von einem Minimum zu einem anderen darstellen. Kennt man nun den Weg, den eine chemische Reaktion im Konfigurationsraum zurücklegt, können alle Zwischenzustände dargestellt werden. Allerdings sind die nötigen Berechnungen sehr aufwändig. Anders als im Experiment kann in einer Simulationen in der Regel nicht der ganze Konfigurationsraum erkundet werden. Dies würde in den meisten Fällen die vorhandene Computerkapazität überfordern. Es müssen also Techniken zum Einsatz kommen, die den Ablauf einer Reaktion ermitteln können ohne dafür den gesamten Raum aller Freiheitsgrade abtasten zu müssen.

In einem thermodynamischen Ensemble, zum Beispiel dem Inhalt eines Reagenzglases, müssen zusätzlich noch statistische Eigenschaften miteinbezogen werden. Das hierfür relevante Potential ist die Freie-Energie-Landschaft, bei der ein Teil der Freiheitsgrade im Konfigurationsraum statistisch gemittelt wurden. In diese Funktion gehen also statistische und energetische Eigenschaften ein. Die Freie Energie kann in Allgemeinen nur durch statistische Simulationen (molekulardynamische oder Monte-Carlo) berechnet werden. Leider kommen die Übergangszustände, an denen wir besonderes Interesse haben, bei statistischen Simulationen besonders selten vor. Daher müssen Techniken verwendet werden, die eine ausreichende Auflösung auch im Bereich dieser seltenen Ereignisse erlauben.

In dieser Arbeit wird ein nicht-physikalisches quadratisches Potential, ein sogenannter *bias*, zur Bewegungsgleichung der Teilchen hinzugefügt. Dadurch wird erreicht, dass auch ungünstige Bereiche im Konfigurationsraum ausreichend aufgelöst werden. Dieses Technik wird *Umbrella Sampling* genannt. Das Bias-Potential wirkt nur entlang einer oder mehrerer Koordinaten, die die Reaktion beschreiben. Sie werden deshalb

Reaktionskoordinaten genannt. Eine Umbrella-Sampling-Simulation wird eine Fluktuation der Reaktionskoordinate ergeben, deren Erwartungswert nahe am, aber im Allgemeinen nicht auf dem Minimum des Bias-Potentials liegen wird. Aus der Differenz zwischen Erwartungswert und Minimum des Bias-Potentials kann der Gradient, der zugrundeliegenden Freien Energieoberfläche berechnet werden. Ähnlich kann die Hessematrix der freien Energie aus der Kovarianz-Matrix der Verteilung der Reaktionskoordinate hergleitet werden. Diese Methode zur Interpretation der Daten, die man durch Umbrella Sampling erhält, nennen wir *Umbrella-integration*.

Zunächst verwenden wir diese Werte um damit die Sattelpunkte, die die Übergangszustände repräsentieren, iterativ zu bestimmen. Ausgehend von diesen Konfigurationen kann der Reaktionspfad durch Verfolgen des Gradienten ermittelt werden. Dieser Algorithmus wurde für das System Alanindipeptid erfolgreich getestet und veröffentlicht.

Diese einfache Methode hat die Nachteile, dass sie zum Einen intrinsisch seriel arbeitet und zum Anderen recht gute Startwert für die Sattelpunkte voraussetzt. In einem zweiten Teil der Arbeit wird deshalb die etablierte Methode der Nudged Elastic Band (NEB)-Optimierungen für die Anwendung in der Freien-Energie-Landschaft erweitert. Bei NEB-Optimierungen beginnt man mit einer ersten Abschätzung für den Reaktionspfad, dieser wird durch eine Anzahl von Konfiguration, sogenannten Bildern, mit gleichem Abstand diskretisiert. Damit die Bilder während der Optimierung gleichmäßig verteilt bleiben, führt man eine nicht physikalische Federkraft ein, die zwischen den Bildern wirkt. Zur eigentlichen Optimierung wird nun die Summe aus der Komponente der Kraft des zugrundeliegenden Potentials, die senkrecht zum Pfad wirkt, und die Komponente der Federkraft die parallel zum Pfad wirkt, minimiert.

In dieser Arbeit wird zuerst ein Optimierer entwickelt, der für bestimmte Testsysteme quadratische Konvergenz von NEB-Optimierungen innerhalb der potentiellen Energie erreicht. Dieser neue Optimierer benutzt für jeden Schritt nicht nur den Gradient sondern auch die Hessematrix des zugrundeliegenden Potentials. Für die Freie-Energie-Oberfläche können beide Werte durch Umbrella-integration ermittelt werden. Um also NEB-Optimierungen in der Freien-Energie Oberfläche durchführen zu können, wird in dieser Arbeit wie folgt vorgegangen. Zuerst wird ein Startpfad z. B. eine gerade Linie zwischen zwei Punkten, meist Minima, als Kleinster-Freier-Energie-Pfad angenommen. Dieser Pfad wird in mehrere Bilder diskretisiert, um dann an jeder dieser Konfigurationen molekulardynamische Simulationen mit Umbrella-integration durchzuführen. Die so erhaltenen Gradienten und Hessematrizen finden nun Eingang in den neu entwickelten NEB-Optimierer. Auf diese Weise benötigt man weniger gute Startwerte für die Sattelpunkt, als Startwerte reicht eine Interpolation zwischen viel leichter zugänglichen Minima. Darüber hinaus ist die Methode intrinsisch parallel, da zu jedem Bild unabhängige molekulardynamische Simulationen durchgeführt werden müssen. Diese Methode wurde für das System Alanindipeptid erfolgreich getestet und mit den Ergebnissen der seriellen Methode verglichen. Anschließend wird der Algorithmus auch für das deutlich aufwendigere System der Bindung von Ligand und Rezeptor in Wasser eingesetzt.

Part I

State of the Art

1

Background and Motivation

The first chapter explains the contextualisation of this work within its discipline.

Contents

1.1 Why We Do Theoretical Chemistry

Chemistry has a broad impact on our daily life. From drugs and food ingredients to material design and environment protection, chemical knowledge plays an important role in the protection of our health as well as in sustainable progress. Research activities that seek to improve this knowledge are usually based on experimental lab work. While experimental methods serve as a wide source of important findings, complementary theoretical studies can help to open ways which would not be accessible by pure experimental methods. An example of the benefits of using computational methods is virtual screening. To find a new medical active component it would be necessary to synthesize thousands of structures and test their impact on human cells in a Petri dish. Using computational methods, the interaction of a substance with proteins found in cells can be simulated. This way a preselection can be made, which helps reduce time and cost of investigation. Further computational simulation of enzymes can uncover their biological function. This may help to develop even newer strategies to fight diseases.

Theoretical chemistry can be divided into three areas. The oldest area addresses theoretical concepts, which use analogies, symmetries and heuristic considerations to predict structures and reactivities of chemical substances and their components. A second area is engaged with the calculation of the electronic structures of molecules and solid state body. Nowadays this work is done exclusively by computational methods. The third area, to which this work belongs, uses computational methods to predict chemical structures and reaction mechanisms.

1.2 Computational Simulations in Theoretical Chemistry

We have seen that we can divide the area of theoretical chemistry into three sub-areas: analytic methods, electronic structure investigations and computational chemistry. The fast-growing availability of computational performance leads to an increasing importance of the last two sub-areas. Since this work belongs to computational chemistry, this and following chapters only deal with this sub-area.

Chemical systems consist of nucleons and electrons. In principle, all properties should be explained by solving the physical equations governing the systems.

However, for the predominant number of multibody systems closed solutions do not exist. In computational chemistry we use numerical methods to find approximative solutions to the governing equations. This involves such a large number of calculations that such simulations can only reasonable be done by large computers. Thus, we use computational simulations to approximate the physical behavior of chemical systems. These results are further used to investigate the structure, reactivity and dynamics. Therefore, this area is called computational chemistry.

1.3 Free Energy

A main task of computational chemistry is to find mechanisms of chemical reactions. While reactants and products of such a reaction can be easily observed by experimental methods, because they exist in a reasonable time, most reactions take place at such small time scales, that they are difficult to investigate by experimental methods. This is where computational simulations join the game. All configurations reached during a simulation can be studied in detail. However, one needs to ensure that the simulated course of the reaction is consistent with that found in nature.

Nature has two different ways of driving processes. The most intuitive one is energy. A river flows from the mountain to the sea because sea level, lying comparatively deeper as it does, has a lower potential energy than the height of the mountain. More difficult to understand is entropy. In paradoxically, a piece of sugar at the bottom of a vessel filled with water dissolves in the whole liquid after some time, even though sugar has a higher density and should stay at the bottom for energetic reasons. This process is driven by entropic properties. While at least for these examples we can clearly distinguish the driving force, in many cases we have to consider an interaction of both drives. This is described by Helmholtz free energy. Thermodynamic systems have the tendency to move towards lower Helmholtz free energy. Its change is described by

$$\Delta A = \Delta E + P\Delta V - T\Delta S \tag{1.1}$$

where ΔE is the change in the energy, P the pressure, ΔV the change of the volume, T the temperature and ΔS the change of the entropy. This formulation leads to a lot of confusion. Since a thermodynamic description is only valid for equilibrium conditions the free energy should not change, $\Delta A = 0$. The only satisfying explanation known by the author uses the concept of internal constrains. Considering again the example of a river flowing down from the mountain: The water is obviously not in equilibrium conditions. However, we can imagine a dam keeping water back on the mountain. In this example the dam serves as an internal constraint, which enables the water to stay in equilibrium condition at a different position. Taking away internal constraints and opening the dam, the water is not in equilibrium condition any more, it flows down to the valley or to a deeper barrier lake, where it will reach another equilibrium with lower free energy after some time. The change of the macroscopic variables in equation (1.1) describes their change between different equilibrium conditions under different internal constraints. However, this concept does not help us to explain how fast the water will flow and which way it will take. It is different in the case of slow processes, like the dissolving of sugar in water. Here the internal dynamics happen much faster than the macroscopically observed process. Describing the solution as infinitely slow, we can treat the process like an infinitely slow change of the internal constraints. This approximation can be found under the catchword quasistatic processes in many textbooks.

In this work internal constraints are applied to a set of variables $\boldsymbol{\xi}$, which are a subset of all micro variables, and used as internal constraints. $\Delta A(\boldsymbol{\xi})$ forms a landscape in the space of the constraint micro variables. Properties gained from this landscape are only valid under the condition of the quasistatic approximation.

Reactant and product of a reaction are represented by minima in the underlying potential, here the free energy $\Delta A(\boldsymbol{\xi})$. These configurations are stable since they will return to their original state after small perturbations. It has been shown that the most probable reaction mechanism between two minima takes place along paths which are tangential to the gradient and lead over saddle points.[1,2]

1.4 Thesis Overview

The main part of this work consists of five chapters. The first chapter explains the background and motivation leading to this thesis. In the second chapter I give a brief overview of literature covering the groundwork necessary to build on this work. Here I start by explaining molecular dynamics using force fields, followed by the mathematical background from statistical physics. This chapter ends by explaining computational methods used to investigate potential and free energy landscapes. The third chapter contains improvements reached during the work. This includes a serial algorithm to find minimum free energy paths (MFEP) and nudged elastic band simulation, first in the potential energy landscape and then in the free energy landscape. The latter one requires a number of independent molecular dynamics simulations at each optimization step. It is therefore an intrinsically parallel process. All developed algorithms are demonstrated for simple test cases. The method of doing nudged elastic band simulations in the free energy surface, the final algorithm which represents the essence of the whole work, is applied to a realistic complex ligand binding problem.

2

LITERATURE OVERVIEW

This chapter introduces the theoretical and computational concepts used throughout the thesis

Contents

2.1 Molecular Dynamics

In computational chemistry one of the main tasks is to analyze reaction mechanisms. However, information about the reaction of a particular molecule yields little insight. The behaviour of chemical structures is subject to statistical properties like thermal stochastic motion and quantum mechanically Heisenberg's uncertainty principle. If we can not generalise the trajectory a single molecule follows during a reaction, we need to average this over many such processes in order to find statistical information about the underlying principles. The method used in this work is not to trace one but many trajectories.

Frankly, this work does not derive statistical properties from many trajectories, but from a single very long trajectory, which will be justified in the section about ergodicity later. Trajectories are calculated by molecular dynamics (MD) simulations. MD simulations approximate the nucleons as classical particles and use classical equations of motion for time propagation.

2.1.1 Integrators

For the time propagation of classical particles Newton's equation of motion has to be solved.

$$m_i \ddot{\boldsymbol{x}}_i = \boldsymbol{F}_{\text{atom},i} \tag{2.1}$$

where m_i is the mass, $\boldsymbol{x}_i$ the position and $\boldsymbol{F}_{\text{atom},i}$ the force acting on the i^{th} atom. However, since in molecular dynamics we always deal with many particle systems, this cannot be done in a closed form, but has to be calculated numerically. Computers only have a limited performance. Newton's equation of motion can not be integrated for every point in time during a period. For numerical integration, time has to be discretised and a function for stepwise calculation of the trajectory be applied. In this work equally spaced time steps Δt are used and spatial coordinates of all N particles are organized in the super vector $\boldsymbol{X} = (x_1, y_1, z_1, x_2, y_2, z_2, x_3, y_3, z_3, \dots, x_N, y_N, z_N)^{\text{T}}$, and analogously the velocities $\boldsymbol{V} = (v_{1,x}, v_{1,y}, v_{1,z}, v_{2,x}, v_{2,y}, v_{2,z}, v_{3,x}, v_{3,y}, v_{3,z}, \dots, v_{N,x}, v_{N,y}, v_{N,z})^{\text{T}}$ and the accelerations $\boldsymbol{A} = (\frac{F_{1,x}}{m_1}, \frac{F_{1,y}}{m_1}, \frac{F_{1,z}}{m_1}, \frac{F_{2,x}}{m_2}, \frac{F_{2,y}}{m_2}, \frac{F_{2,z}}{m_2}, \frac{F_{3,x}}{m_3}, \frac{F_{3,y}}{m_3}, \frac{F_{3,z}}{m_3}, \dots, \frac{F_{N,x}}{m_N}, \frac{F_{N,y}}{m_N}, \frac{F_{N,z}}{m_N})^{\text{T}}$.

Within this nomenclature the simplest time stepping algorithm, the explicit Euler algorithm, applied to equation (2.1) yields

$$\boldsymbol{V}_{n+1} = \boldsymbol{V}_n + \Delta t \boldsymbol{A}_n, \tag{2.2}$$

$$\boldsymbol{X}_{n+1} = \boldsymbol{X}_n + \Delta t \boldsymbol{V}_n \tag{2.3}$$

where the index n serves as a shortcut for the position in time e. g. $\boldsymbol{X}_n = \boldsymbol{X}(t = n \cdot \Delta t)$. This method corresponds to a truncation of the Taylor expansion of the real solution after the linear element. It has therefore an error of $\mathcal{O}(\Delta t^2)$. Unfortunately, this method has a comparatively large error, and it is also known to be unstable for most cases. A much better method is the so called leapfrog method

$$\boldsymbol{V}_{n+\frac{1}{2}} = \boldsymbol{V}_{n-\frac{1}{2}} + \Delta t \boldsymbol{A}_n \tag{2.4}$$

$$\boldsymbol{X}_{n+1} = \boldsymbol{X}_n + \Delta t \boldsymbol{V}_{n+\frac{1}{2}}. \tag{2.5}$$

By shifting the sampling points of time between velocity and position half a time step Δt, we get an error of $\mathcal{O}(\Delta t^3)$. This can be seen by plugging equation (2.5) into (2.4).

$$\boldsymbol{X}_{n+1} = \boldsymbol{X}_n + \Delta t \boldsymbol{V}_{n-\frac{1}{2}} + \Delta t^2 \boldsymbol{A}_n \tag{2.6}$$

The exact value for $\boldsymbol{V}_{n-\frac{1}{2}}$ can be expressed in a Taylor expansion around $t = n \cdot \Delta t$.

$$\boldsymbol{V}_{n-\frac{1}{2}} = \boldsymbol{V}_n - \frac{\Delta t}{2} \boldsymbol{A}_n - \frac{\Delta t^2}{4} \frac{\mathrm{d}^3 \boldsymbol{X}_n}{\mathrm{d}t^3} + \mathcal{O}(\Delta t^4) \tag{2.7}$$

Putting the written terms of equation (2.7) in (2.6)

$$\boldsymbol{X}_{n+1} = \boldsymbol{X}_n + \Delta t \left[\boldsymbol{V}_n - \frac{\Delta t}{2} \boldsymbol{A}_n - \frac{\Delta t^2}{4} \frac{\mathrm{d}^3 \boldsymbol{X}_n}{\mathrm{d}t^3} \right] + \Delta t^2 \boldsymbol{A}_n \tag{2.8}$$

$$= \boldsymbol{X}_n + \Delta t \boldsymbol{V}_n + \frac{\Delta t^2}{2} \boldsymbol{A}_n - \underbrace{\frac{\Delta t^3}{4} \frac{\mathrm{d}^3 \boldsymbol{X}_n}{\mathrm{d}t^3}} \tag{2.9}$$

while the under-braced term does not coincide with the Taylor expansion of $\boldsymbol{X}$ and is of the order $\mathcal{O}(\Delta t^3)$. In addition, the leapfrog algorithm does not only have a higher accuracy of one order in comparison to the Euler algorithm, but it has also been shown that the leapfrog formula is a symplectic integrator.[3] It is often claimed that symplectic integrators produce results which conserve energy in the system averaged over many steps, and that they preserve the phase space volume of a thermodynamic ensemble.[3–7] Note that using the leapfrog algorithm provides higher accuracy and preservation of thermodynamical conservation laws by the same amount of computational operation used for the Euler stepping and even less memory since the Euler algorithm needs to store $\boldsymbol{V}_n$ to calculate $\boldsymbol{X}_{n+1}$. For the leapfrog algorithm the storage of $\boldsymbol{V}_n$ can simply be overwritten by the value of $\boldsymbol{V}_{n+1}$. Compare equations (2.4) and (2.5) with (2.2) and (2.3).

Apart from its simple structure and benign numerical behavior, the leapfrog algorithm has the disadvantage that velocities and positions are calculated at different times. Within the time discretization of equation (2.4) we can calculate the velocity at integer time positions by either stepping half a time step forwards or backwards

$$\boldsymbol{V}_{n+\frac{1}{2}} = \boldsymbol{V}_{n-\frac{1}{2}} + \Delta t \boldsymbol{A}_n \ \Rightarrow \boldsymbol{V}_n = V_{n+\frac{1}{2}} - \frac{1}{2}\Delta t \boldsymbol{A}_n \tag{2.10}$$

$$\boldsymbol{V}_{n+\frac{3}{2}} = \boldsymbol{V}_{n+\frac{1}{2}} + \Delta t \boldsymbol{A}_{n+1} \ \Rightarrow \boldsymbol{V}_{n+1} = V_{n+\frac{1}{2}} + \frac{1}{2}\Delta t \boldsymbol{A}_{n+1}. \tag{2.11}$$

Subtracting equation (2.10) from (2.11) and rearrange the outcome we get the stepping formula

$$\boldsymbol{V}_{n+1} = V_n + \frac{1}{2}\Delta t \left[\boldsymbol{A}_n + \boldsymbol{A}_{n+1}\right]. \tag{2.12}$$

However, this time discretization is not compatible with the leapfrog stepping. Equation (2.12) calculates the velocity at full time positions but equation (2.5) needs it at half time positions. Therefore we reformate equation (2.10) to $\boldsymbol{V}_{n+\frac{1}{2}} = V_n + \frac{1}{2}\Delta t \boldsymbol{A}_n$ and plug it into equation (2.5).

$$\boldsymbol{X}_{n+1} = \boldsymbol{X}_n + \Delta t \boldsymbol{V}_n + \frac{1}{2}\Delta t^2 \boldsymbol{A}_n. \tag{2.13}$$

Equations (2.12) and (2.13) are together called the velocity Verlet integrator. Since it is the mathematical equivalent to the leapfrog algorithm, it shares the properties of symplecticity and order of error.

Both the velocity Verlet as and as the leapfrog integrator are usually available in molecular dynamics software and are widely used. One may wonder why integrators with higher accuracy should not be used. The reason is that we do not aim to numerically calculate a particular trajectory but rather average behaviour. Therefore it is important that the integrator creates a canonical trajectory, but small perturbations are not of any consequence if they statistically cancel out. A symplectic integrator meets these conditions.[3,5]

2.1.2 Force Fields

For a correct description of the force between atoms the quantum mechanic equations of motions have to be solved. This means that the common wave function for electrons and nucleons has to be found. However, for most cases the Born–Oppenheimer approximation can be applied. This approximation states that one can separate the motion of electrons and nucleons because of the different timescales on which the two kinds of particles are accelerated. In the case of molecular dynamic simulations this means that the Schrödinger equation is solved for the electrons. The Coulomb potential of the density probability of the surrounding electrons is used to calculate the force acting on the nucleons. This force enters the calculation for the movement of the nucleons. For many cases, and usually for heavy atoms, nucleons can be treated classically.

Unfortunately, for many atoms such as we usually face in biological systems, even within the Born–Oppenheimer approximations numerical quantum mechanical calculations are computationally prohibitive. Therefore we use a types of reduced models called force fields. A force field models the force acting on a particular atom by

$$\boldsymbol{F}_{i,j} = \boldsymbol{F}_{i,j\,\text{bound}} + \boldsymbol{F}_{i,j\,\text{nonbound}} \tag{2.14}$$

with

$$\boldsymbol{F}_{i,j\,\text{bound}} = \boldsymbol{F}_{i,j\,\text{distance}} + \boldsymbol{F}_{i,j\,\text{angle}} + \boldsymbol{F}_{i,j\,\text{dihedral}} \tag{2.15}$$

and

$$\boldsymbol{F}_{i,j\,\text{nonbound}} = \boldsymbol{F}_{i,j\,\text{van der Waals}} + \boldsymbol{F}_{i,j\,\text{electrostatic}}. \tag{2.16}$$

These interactions are illustrated in Fig. 2.1. The indices i and j are written to indicate that all these interactions take place between different atoms.

The whole force acting on the i^{th} atom is the sum

$$\boldsymbol{F}_i = \sum_{i \neq j}^{N} \boldsymbol{F}_{i,j}, \tag{2.17}$$

where we sum up over all N atoms but exclude the i^{th} one. The single terms for a certain kind of interaction between two atoms $\boldsymbol{F}_{i,j}$ are formed by analytical

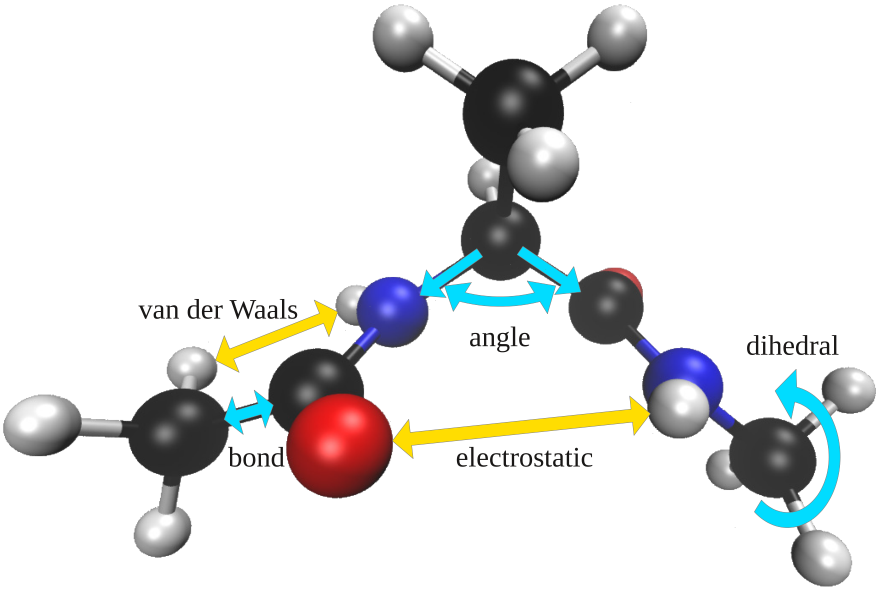

Figure 2.1: Illustration of interactions encountered in molecular dynamic simulations with force fields. Bonded interactions: bond length, angle and dihedral are marked with turquoise arrows. Non-bonded interactions: the electrostatic and van der Waals interactions are marked with yellow arrows. Each kind of interaction is visualized only once but acts on each atom.

functions, which approximate the real behavior. For example, in the bounded distance in most molecular dynamics simulations software force is represented by either the harmonic approximation

$$V_{ij\ \mathrm{distance}} = \frac{1}{2} k \left(\boldsymbol{r}_{ij} - \boldsymbol{r}_{ij,0} \right)^2 \tag{2.18}$$

or a Morse potential

$$V_{ij\ \mathrm{distance}} = D \left(1 - \mathrm{e}^{\alpha (\boldsymbol{r}_{ij} - \boldsymbol{r}_{ij,0})} \right)^2 , \tag{2.19}$$

where $\boldsymbol{r}_{ij}$ denotes the actual and $\boldsymbol{r}_{ij,0}$ the equilibrium distance. The term V_x denotes the potential of the corresponding force $\boldsymbol{F}_x = -\nabla V_x$. A Morse potential has the advantage that it better approximates the potential for larger distances. The functions are tuned by fitting the parameters k, D and α to experimentally archived and calculated properties for the particular bond. All these parameters depend on atom and bond types. Obtaining all the parameters for different atom types and different kind of interactions demands a huge amount of work. Databases so-called force fields like charmm[8] or amber[9] are usually used.

Chemical experiments very seldom take place in the vacuum or gas phase, where one only needs to model molecules with very little interaction with other molecules. Most chemical reactions are observed within a solvent e. g. water. One has to admit that water molecules do not only act as a thermal reservoir but also interfere in the molecular dynamic properties by electrostatic forces and spatial dimension. A ligand entering a binding pocket has to crow the water out, while without water in many cases an enzyme would not fold into the active geometry. Therefore realistic modelling of solvents is necessary. On the other hand, in usual systems many more atoms belong to the solvent, which are dynamics we are not interested in. The model for the parameter should therefore compromise between reducing computational effort and reproducing the influence of the solvent on the observed part of the system as closely as possible.

In this work the TIP3P water model[10] is used. This model uses three point charges, each for one atom to represent the electrostatic influence of one water molecule. The spatial crowding is modeled by Lennard–Jones potential around each atom. The bond distances and angles are kept fixed, since we are not interested in the dynamics of the water itself.

The TIP3P water model[10] is not the only simplified water model used in common force fields. It has been used in this work because of its width spread application. Since this work focuses on the techniques rather than a particular reaction mechanism, the main motivation for the choice of the water model was comparability with former work.

2.1.3 Thermostats

Time propagation in molecular dynamics simulations are designed to conserve energy over many steps. This is ensured by the use of symplectic integration algorithms and is an important property because the simulation aims to reproduce the behaviour of the real system. If it were possible to model a system perfectly, only configurations with the same energy would occur. We have seen that averaged over many time steps, symplectic integrators are a good approximation to reality with respect to energy conservation. The particles can exchange energy between each other, but the sum of the energy as a whole must be constant because of the empirical principle of energy conservation. If one also keeps volume and the number of particles constant, as we usually do in molecular dynamic simulations, such an ensemble is called a micro-canonical ensemble. Contrary, even with high quality isolation a real system always interacts with the world. The total amount of energy within the ensemble can change by energetic exchange with the environment. Configurations occur with the probability of the Boltzmann factor

$$P_i = \exp(-\beta \boldsymbol{E}_i) \tag{2.20}$$

where $\beta = \frac{1}{k_\mathrm{B}T}$ and E_i is the energy of the particular configuration and microstate respectively. Such a system is called a canonical system and has different statistic from a system with a constant energy.

The most intuitive way to simulate a canonical ensemble would be to simulate a part of the environment of the system, a thermal reservoir, and allow energy exchange. However, we would spend a lot of computational performance by calculating the dynamics of the thermal reservoir. Therefore, various algorithms, so-called thermostats were developed in order to allow the system to visit configurations with different energies with thermostatistical behaviour.

In this work I use the Nosé–Hoover chain[11–14] thermostat, a variant of a thermostat proposed by Nosé.[11] This thermostat is based on the idea of reducing the thermal reservoir to one degree of freedom s to which an effective mass Q and potential of

$$\mathcal{V}(s) = -\frac{g}{\beta} \ln s \tag{2.21}$$

is assigned. The parameter $g = 3N + 1$ and the form of the potential $\mathcal{V}(s)$ will be justified later. One degree of freedom can of course give and take energy but cannot have a stochastic behaviour like a realistic thermal reservoir.

The more sophisticated part of the algorithm is to couple this one dimensional thermal reservoir to the simulated system. In nature this is always done by the interaction of particles of the subsystems which each other. This corresponds to a temporal modification of the force respective to the potential in the equation of motion. However, this would require a high dimensional thermal reservoir with stochastic behaviour. Otherwise a modification of the potential of the form

$$V(\boldsymbol{q}) \ \rightarrow \tilde{V}(\boldsymbol{q}) = f(s, \boldsymbol{q}) V(\boldsymbol{q}) \tag{2.22}$$

would result in strong correlated energetic interaction between the thermal reservoir and the different degrees of freedom of the system. Nosé therefore modified the kinetic energy term in order to introduce an interplay between the system and the thermal reservoir. The resulting kinetic Energy term reads

$$T(\boldsymbol{p}) = \sum_{i=1}^{N} \frac{p_i^2}{2m_i} \to \tilde{T}(\boldsymbol{p}) = \sum_{i=1}^{N} \frac{p_i^2}{2m_i s^2}. \tag{2.23}$$

For $s < 1$ the potential of equation (2.21) will be positive, consequently the kinetic energy of the simulated system will be amplified, equation (2.23). For $s > 1$ the opposite is true. Joseph Louis Lagrange introduced a formalism to describe classical mechanical systems by just one scalar function $L = T - V$. We get the modified Lagrange function for the whole system (simulated system of interest plus thermal reservoir) by means of

$$\tilde{\mathcal{L}} = \tilde{T}(\boldsymbol{p}) + \mathcal{T}(s) - \tilde{V}(\boldsymbol{q}) - \mathcal{V}(s) = \sum_{i=1}^{N} \frac{m_i \dot{q}_i^2}{2s^2} - V(\boldsymbol{q}) + \frac{Q}{2}\dot{s}^2 + \frac{g}{\beta} \ln s \tag{2.24}$$

The Hamilton function is formed by a Legendre transformation and yields with $p_i = m_i \dot{q}_i$ and $p_s = Q\dot{s}$

$$\mathcal{H}(\boldsymbol{q}, \boldsymbol{p}, s, p_s) = \sum_{i=1}^{N} \frac{p_i^2}{2m_i s^2} + V(\boldsymbol{q}) + \frac{p_s^2}{2Q} - \frac{g}{\beta} \ln s. \tag{2.25}$$

The effective mass Q of the thermal reservoir determines how strongly the systems are coupled. The larger Q is, the slower the simulated system returns to the desired temperature after fluctuations or perturbations. Molecular dynamics tools usually use the dubiously justified term response time for the shortcut $\tau = \sqrt{\frac{Q\beta}{g}}$.

If a Hamilton function does not explicitly depend on time, energy must be conserved. Consequently the whole system described by the Hamilton function of equation (2.25) must be a microcanonical ensemble if we keep volume and the number of particles fixed. The central property to describe a thermostatistical system is the partition function. It is the overall sum of occupied microstates. The partition function of the microcanonical system treated here reads

$$Q = \int_{s} \int_{ps} \int_{\mathbb{R}^{3N}} \int_{\mathbb{R}^{3N}} s^{3N} \delta \left[\mathrm{H}(\boldsymbol{q}, \boldsymbol{p}') + \frac{p_s^2}{2Q} - \frac{g}{\beta} \ln s - E \right] \mathrm{d}s \mathrm{d}p_s \mathrm{d}\boldsymbol{q} \mathrm{d}\boldsymbol{p}', \tag{2.26}$$

where $\mathrm{H}(\boldsymbol{q}, \boldsymbol{p}')$ denotes the part of the Hamilton containing the actual system of interest and the substitution $\boldsymbol{p}' = \boldsymbol{p}/s$ was used. E is the energy of the whole system. The number of possible states of a system is proportional to the phase space volume $\int_{s} \int_{ps} \int_{\mathbb{R}^{3N}} \int_{\mathbb{R}^{3N}} s^{3N} \mathrm{d}s \mathrm{d}p_s \mathrm{d}\boldsymbol{q} \mathrm{d}\boldsymbol{p}'$. In a microcanonical system we only allow states with a certain energy to be occupied. This is the reason why the δ distribution appears in the support of the integral. Actually in equation (2.26) the factor $\left((N+1)!h^{3N+1}\right)^{-1}$ concerning that according to Heisenberg's uncertainty principle states are not infinitely dense is missing. However, it will not change the qualitative result of this analysis. A simple substitution leads to the rule

$$\int \delta\left[f(x)\right]\mathrm{d}x = \int \sum_i \frac{\delta\left[x - x_i\right]}{f'(x_i)}\mathrm{d}x \tag{2.27}$$

with x_i being the roots of the function $f(x)$. The only root of the function in the argument of the delta distribution in equation (2.26) is $s_0 = \exp\left(-\frac{\mathrm{H}(\boldsymbol{q},\boldsymbol{p}')+\frac{p_s^2}{2Q}-E}{g}\beta\right)$. Hence the microcanonical partition function can be reformulated as

$$\begin{aligned}
Q =& \frac{\beta}{g}\int\limits_{s}\int\limits_{ps}\int\limits_{\mathbb{R}^{3N}}\int\limits_{\mathbb{R}^{3N}} s^{3N} s_0 \cdot \delta\left[s - s_0\right]\mathrm{d}s\mathrm{d}p_s\mathrm{d}\boldsymbol{q}\mathrm{d}\boldsymbol{p}' \\
=& \frac{\beta}{g}\int\limits_{ps}\int\limits_{\mathbb{R}^{3N}}\int\limits_{\mathbb{R}^{3N}} \exp\left(-\left(3N+1\right)\frac{\mathrm{H}(\boldsymbol{q},\boldsymbol{p}')+\frac{p_s^2}{2Q}-E}{g}\beta\right)\mathrm{d}p_s\mathrm{d}\boldsymbol{q}\mathrm{d}\boldsymbol{p}' \\
=& \frac{\beta}{(3N+1)}\int\limits_{ps}\exp\left(-\left(\frac{p_s^2}{2Q}-E\right)\beta\right)\mathrm{d}p_s\int\limits_{\mathbb{R}^{6N}}\exp\left(-\left(\mathrm{H}(\boldsymbol{q},\boldsymbol{p}')\right)\beta\right)\mathrm{d}\boldsymbol{q}\mathrm{d}\boldsymbol{p}'
\end{aligned} \tag{2.28}$$

where the shortcut $g = 3N+1$ was used. We clearly see in equation (2.28) that the microcanonical partition function of the whole system containing the one dimensional thermal reservoir and the simulated system only differs from the partition function of a canonical system by the factor $\frac{1}{(3N+1)k_{\mathrm{B}}T}\int\limits_{ps}\exp\left(-\left(\frac{p_s^2}{2Q}-E\right)\beta\right)\mathrm{d}p_s$. Note that in this nomenclature E denotes the fixed energy of the microcanonical ensemble, while E_i in equation (2.20) denotes the energy of the particular microstate, which is equivalent to its Hamilton function.

In equation (2.26) we implicitly assumed that the system visits all points in phase space, with the particular energy E. This is a safe assumption for a large chaotic fluctuating thermal reservoir. However, the simple one-dimensional thermal reservoir of the Nosé–Hoover thermostat may not be able to activate some degrees of freedom. It was shown that even for such cases one gets a canonical distribution by using a chain of k one-dimensional thermal reservoirs $s_i = \{s_1, \ldots, s_k\}$.[14] While the simulated system itself is regulated by the thermal reservoir s_1, s_1 is driven by s_2 and so on. Since each thermal reservoir only consists of one degree of freedom, typical chain lengths from 4 to 10 are of no consequence in comparison with the few thousand degrees of freedom used to describe realistic systems.

2.2 Mathematical Concepts

2.2.1 Free Energy Surface

For investigation of reaction mechanisms in a thermodynamic ensemble, e. g. the contents of test tube statistical information have to be included. A potential which does so is the free energy landscape, for which some degrees of freedom of the configuration space are thermostatistically integrated out. This function therefore includes statistical and energetic properties. The free energy surface can be calculated by[15]

$$A(\xi) = -\frac{1}{\beta} \ln \left[\frac{Q(\xi)}{Q} \right] . \tag{2.29}$$

The coordinate ξ denotes an arbitrary degree of freedom, where $\beta = \frac{1}{k_\mathrm{B} T}$ with T being the temperature, k_B the Boltzmann's constant and the partition function

$$Q = \iint \exp(-\beta E(\boldsymbol{q}, \boldsymbol{p}))\ \mathrm{d}^{3N}q\ \mathrm{d}^{3N}p\ . \tag{2.30}$$

$E(\boldsymbol{q}, \boldsymbol{p})$ denotes the energy of a certain point in phase space described by the spatial coordinates $\boldsymbol{q}$ and the momenta $\boldsymbol{p}$.

$$Q(\xi) = \iint \delta(\xi'(\boldsymbol{q}) - \xi) \exp(-\beta E(\boldsymbol{q}, \boldsymbol{p}))\ \mathrm{d}^{3N}q\ \mathrm{d}^{3N}p \tag{2.31}$$

with δ being Dirac's delta function, is a constrained partition function in which all degrees of freedom but ξ_ref are integrated out. $\xi(\boldsymbol{q})$ may be a component of the position vector $\boldsymbol{q}$ or a non-linear function out of those e. g. a torsion angle. The only restriction implicitly made is in equation (2.31), that it is defined at every position in the configuration space. As will be discussed later, this condition yields problems if we want to use the arc length of a path as reaction coordinate. In these cases we have to generalize it for the environment.

In the absence of an external electromagnetic field the whole energy is a sum of potential energy and kinetic energy $E(\boldsymbol{p}, \boldsymbol{q}) = K(\boldsymbol{p}) + V(\boldsymbol{q})$. Consequently, the integrations over $\boldsymbol{p}$ in equations (2.30) and (2.31) cancel. Equation (2.29) can be generalized to higher dimensional subspaces of $\mathbb{R}^M$, which results in

$$A(\boldsymbol{\xi}) = -\frac{1}{\beta} \ln \frac{\int \delta(\boldsymbol{\xi}'(\boldsymbol{q}) - \boldsymbol{\xi}) \exp(-\beta V(\boldsymbol{q}))\ \mathrm{d}^{3N} q}{\int \exp(-\beta V(\boldsymbol{q}))\ \mathrm{d}^{3N} q}\ , \tag{2.32}$$

where $\boldsymbol{\xi}$ is a general coordinate, or a set of those e. g. two torsion angles.[16]

$A(\boldsymbol{\xi})$ is often referred to as free-energy surface. This may be confusing, because the free energy is actually a thermodynamical state function independent of microscopic variables such as e. g. the configuration space, compare equation (1.1). In fact, the potential of mean force is neither a potential energy nor a pure free energy but can be tuned step by step from a potential energy to the free energy by integrating out more and more degrees of freedom.

The careful reader may have noticed that the free energy surface $A(\boldsymbol{\xi})$, equation (2.32), derived here is not the same as the change of free energy under different internal constraints explained in section 1.3. Equation (2.32) only considers a slice of the non-constrained equilibrium distribution, while internal constraints would force all microstates to a certain value of the considered degree of freedom $\boldsymbol{\xi}$. However, this difference is only a constant factor in the partition function leading to a constant shift of the free energy potential. Obviously, only differences and deviations but not the absolute value of a potential are of physical relevance.

2.2.2 Intrinsic Reaction Coordinates

A chemical reaction can be described as a path in a reaction space, E. g. the $3N$ dimensional configuration space of all spatial coordinates of the N atoms forming the studied system. Describing the chemical reaction A $\longrightarrow$ B in a reaction space, reactant A and product B occupy different areas. An infinite amount of lines can be drawn to connect both areas. Each line represents a possible course of the reaction between A and B. However the possibility of occurrence differs a lot depending on the physical properties of the system. This is taken into account by the introduction of a reaction potential. In terms of the configuration space this would be the potential energy. In this work I mainly use the free energy landscape in respect to the potential of mean force as defined in equation (2.32), which will be explained in detail later. For the potential of mean force the reaction space is a subspace of the configuration space, only containing a subset of atoms important to describe the reaction. Work done shows that the most probable reaction path leads over saddle points and is always parallel to the gradient of the underlying potential.[1,2] Considering a potential energy surface this would be the minimum energy path (MEP). For the free energy surfaces this path is called the minimum free energy path (MFEP).[17–24]

The MFEP is a one dimensional curvilinear line embedded in the high dimensional reaction space. In this work I exclusively use the symbol s to denote the arc length s along the MFEP, the so-called intrinsic reaction coordinate. ξ denotes any one-dimensional reaction coordinate. At the MFEP, the value of the reaction coordinate s is merely the arc length of the path. Furthermore the path s is not defined. To generalise the concept of an intrinsic reaction coordinate for configuration in environment, to the best of the author's knowledge no satisfactory mathematical conception exists. However, in this work, equation (2.31) will only be evaluated for Cartesian coordinates or the MFEP. The latter describes the path with the highest probability of the reaction taking place. In most cases all significant contribution to the reaction occurs from paths in the vicinity of the MFEP, where one may approximately assign equal values of the reaction coordinate s to isosurfaces perpendicular to the path as illustrated in figure 2.2.

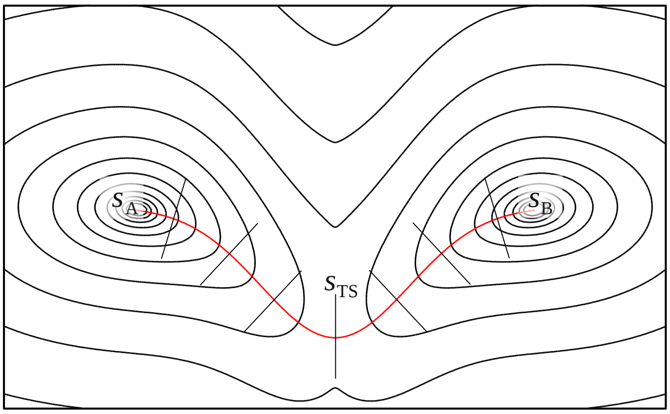

Figure 2.2: Sketch to illustrate the concept of intrinsic reaction coordinate. An arbitrary example free energy landscape is drafted by isolines. The red line shows minimum free energy path (MFEP). The reaction coordinate s denotes arc length along the MFEP. Thin straight lines crossing the MFEP illustrate the approximative generalisation of the reaction coordinate in the vicinity of the path by perpendicular surfaces.

The tangent vector of the intrinsic reaction coordinate reads

$$\boldsymbol{\tau}(s) = \frac{\mathrm{d}\boldsymbol{s}}{\mathrm{d}s} = -\frac{\boldsymbol{g}(\boldsymbol{q}^{\mathrm{RCS}}(s))}{|\boldsymbol{g}(\boldsymbol{q}^{\mathrm{RCS}}(s))|}. \tag{2.33}$$

The minus sign results from the arbitrary definition starting the measurement of the arc length at the saddle point. At a saddle point the gradient is zero and equation (2.33) is not defined. In the infinitesimal vicinity of the saddle point $\boldsymbol{q}^{\mathrm{RCS}}(0))$ we can use a first order Taylor expansion of the gradient.

$$\boldsymbol{g}(\boldsymbol{q}^{\mathrm{RCS}}(0) + \mathrm{d}\boldsymbol{q}^{\mathrm{RCS}}) = \mathbf{H}(s=0)\mathrm{d}\boldsymbol{q}^{\mathrm{RCS}}. \tag{2.34}$$

The constant part of the Taylor expansion at the saddle point is zero by definition. On the MFEP

$$\mathrm{d}\boldsymbol{s} = \frac{\partial \boldsymbol{q}^{\mathrm{RCS}}(s=0)}{\partial s}\mathrm{d}s = \boldsymbol{q}^{\mathrm{RCS}}(s=\mathrm{d}s) - \boldsymbol{q}^{\mathrm{RCS}}(s=0). \tag{2.35}$$

Putting all these ingredients together we get a condition for the MFEP in the vicinity of the saddle point

$$-|\mathbf{H}(s=0)\mathrm{d}\boldsymbol{s}|\frac{\mathrm{d}\boldsymbol{s}}{\mathrm{d}s} = \mathbf{H}(s=0)\mathrm{d}\boldsymbol{s}. \tag{2.36}$$

This is obviously an eigenvalue equation for negative eigenvalues only. Therefore we can state that the MFEP at the saddle point is tangential to an eigenvector with a negative eigenvalue.

One may argue that the minus sign in equation (2.33) comes from an arbitrary choice of the start of the arc length. Consider a definition of the arc length, where s increases when the MFEP approaches the saddle point. In this case one side of equation (2.35) has to be multiplied by -1 and we end up with a similar eigenvalue equation, with the only difference being that $s \neq 0$.

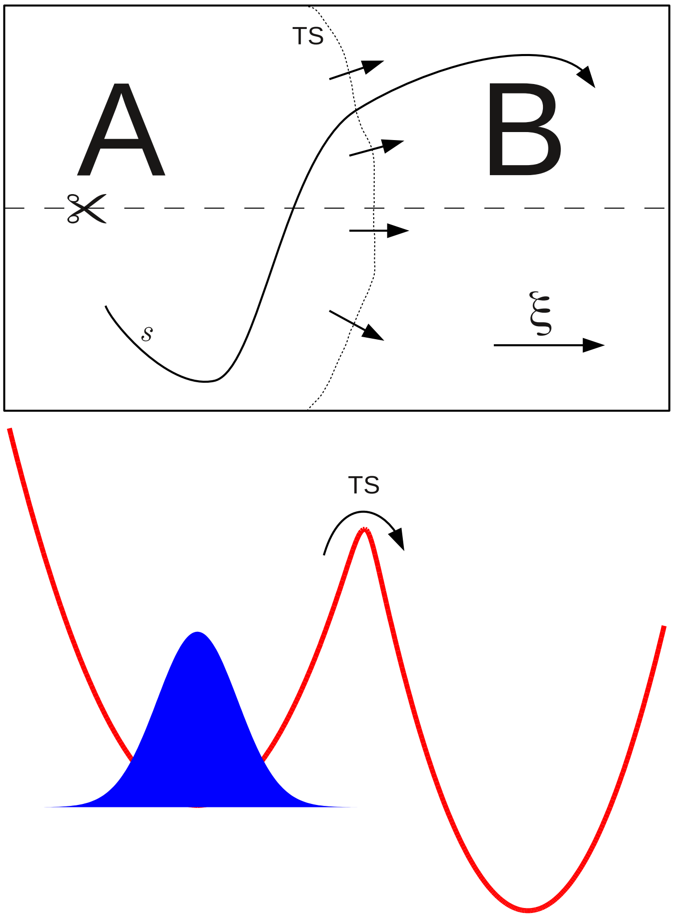

Figure 2.3: Sketch to illustrate concepts used in transition state theory. Individual configurations residing in area A are said to be in the reactant state. Everything in B is said to be in the product state. The surface TS denoting the border between reactant and product state is drawn with a fine dashed line. Arrows symbolise the chemical reaction A $\longrightarrow$ B. The solid serpentine line illustrates the intrinsic reaction coordinate. Illustration below shows an example potential energy profile resulting from cutting along one particular spatial degree of freedom symbolized by a dashed straight line. Since the reaction from A to B happens on time scales much larger than equilibration within reactant and product we can assume thermal equilibrium within A but not between A and B.

2.2.3 Transition State Theory

In transition state theory one searches for an expression to calculate the rate of a chemical reaction from the potential along the reaction coordinate. Here I follow the idea of reference [25] but will end up with a formulation known from [26]. The rate of a chemical reaction is usually expressed with the help of a rate constant k which obeys the formula

$$\frac{\mathrm{d}}{\mathrm{d}t}\,[\mathrm{A}] = -k\,[\mathrm{A}]\,, \tag{2.37}$$

while [A] denotes the concentration of the reactant A. In the following we regard the chemical reaction A $\longrightarrow$ B as taking place between two minima separated by a barrier as illustrated in figure 2.3. The peak of the barrier is called the transition state, and denoted by ξ_{TS}. Every microstate at the left side of ξ_{TS} is taken to be in A. Furthermore the assumption is made that the residence time in A is much longer than the time needed for equilibration between species in A. The probability in terms of concentration of finding an individual structure at a certain volume element of the phase space is consequently

$$\mathrm{d}\,[\mathrm{A}] = \frac{\exp(-\beta E(\boldsymbol{q},\boldsymbol{p}))\mathrm{d}\boldsymbol{q}\mathrm{d}\boldsymbol{p}}{\int^{\mathbb{R}^{6N}} \Theta(\xi_{\mathrm{TS}}-\xi)\exp(-\beta E(\boldsymbol{q},\boldsymbol{p}))\mathrm{d}\boldsymbol{q}\mathrm{d}\boldsymbol{p}}\,[\mathrm{A}]\,. \tag{2.38}$$

The nominator serves for normalization. $\Theta(\xi)$ denotes the Heavy side function, indicating that integration merely runs over the subspace of the phase space belonging to the reactant A. To know the change of the concentration of A over time one needs to divide equation (2.38) by dt and integrate over the subspace belonging to A.

$$\frac{\mathrm{d}}{\mathrm{d}t}\,[\mathrm{A}] = \frac{1}{\mu}\frac{\int p_1\exp(-\beta\frac{p_1^2}{2\mu})\mathrm{d}p_1}{\int\exp(-\beta\frac{p_1^2}{2\mu})\mathrm{d}p_1}\frac{\int^{\mathrm{TS}}\exp(-\beta E(\boldsymbol{q},\boldsymbol{p}))\mathrm{d}\boldsymbol{q}\mathrm{d}\boldsymbol{p}_2\ldots\mathrm{d}\boldsymbol{p}_{3N}}{\int^{\mathbb{R}^{6N-1}}\Theta(\xi_{\mathrm{TS}}-\xi)\exp(-\beta E(\boldsymbol{q},\boldsymbol{p}))\mathrm{d}\boldsymbol{q}\mathrm{d}\boldsymbol{p}}\,[\mathrm{A}]\,. \tag{2.39}$$

where I used $\frac{\mathrm{d}q_1}{\mathrm{d}t} = v_1 = \frac{p_1}{\mu}$ and implicitly presumed that the Energy can be split into independent summands. The mass is called μ to indicate that it is the reduced mass of the atoms involved in the reaction. The hypersurface TS is a $3N-1$ dimensional subspace orthogonal to q_1. Obviously the support of the integration over p_1 is antisymmetric and the result of the integral is $\int p_1\exp(-\beta\frac{p_1^2}{\mu})\mathrm{d}p_1 = 0$ – and how should it be otherwise since we are considering equilibrium condition?

This induces the need for a further assumption. All individuals crossing TS in the direction of B and accordingly $p_1 > 0$ are seen as taking part in the reaction and belong immediately to state B. This is not wrong in itself. The problem arises from adding the back reaction to equation (2.37)

$$\frac{\mathrm{d}}{\mathrm{d}t}\,[\mathrm{A}] = -k\,[\mathrm{A}] + k_{\leftarrow}\,[\mathrm{B}]\,. \tag{2.40}$$

Calculating the rate $k_{\leftarrow}$ for the back reaction one needs to address the fact that individuals are not in thermal equilibrium with state B by merely crossing an arbitrary boundary. Even if at the beginning of the reaction the concentration [B] is very small, the few individuals which had already crossed the boundary from A to B are close to the dividing surface TS, so that they can easily recross.

In transition state theory the approximation of no early recrossing is made. An individual with a momentum $p_1 > 0$ is treated as thermally equilibrated in B first. Obviously this assumption mad is most valid by choosing the surface S so as to reside at the "watershed" of the free energy landscape between A and B, the previously mentioned generalized transition state. Equation (2.39) is transformed to

$$\frac{\mathrm{d}}{\mathrm{d}t}\,[\mathrm{A}] = \sqrt{\frac{Tk_{\mathrm{B}}}{2\mu\pi}}\,\frac{\int^{\mathrm{TS}} \exp(-\beta E(\boldsymbol{q}))\mathrm{d}\boldsymbol{q}}{\int^{\mathbb{R}^{3N}} \Theta(\xi_{\mathrm{TS}} - \xi)\exp(-\beta E(\boldsymbol{q}))\mathrm{d}\boldsymbol{q}}\,[\mathrm{A}]\,, \tag{2.41}$$

where integration over p_1 in the enumerator was done between the borders $0 \to \infty$ and equal to equation (2.32) the integral over all other momenta was canceled.

A constant value of the generalized coordinate $\xi = \xi_{\mathrm{TS}}$ was already assigned to the surface TS. Doing so, in general hypersurfaces with $\xi = const$ cannot be flat. Indeed in a curvilinear coordinate system energy cannot be expressed as a sum of functions of the single components of $\boldsymbol{q}$ and $\boldsymbol{p}$. This seems to be in contradiction to some assumptions made in the derivation before. However, for every infinitesimal element of phase space appearing in the integral expression a local flat linearisation of the coordinate system can be used. Writing

$$\int^{\mathrm{TS}} \exp(-\beta E(\boldsymbol{q}))\mathrm{d}\boldsymbol{q} = \int^{\mathbb{R}^{3N}} \delta(\xi - \xi_{\mathrm{TS}})\exp(-\beta E(\boldsymbol{q}))\mathrm{d}\boldsymbol{q} = Q(\xi_{\mathrm{TS}}) \tag{2.42}$$

one gets

$$\frac{\mathrm{d}}{\mathrm{d}t}\,[\mathrm{A}] = \sqrt{\frac{Tk_{\mathrm{B}}}{2\mu\pi}}\,\frac{Q(\xi_{\mathrm{TS}})}{\int_0^{\xi_{\mathrm{TS}}} Q(\xi)\mathrm{d}\xi}\,[\mathrm{A}] \tag{2.43}$$

which is consistent with the result in reference [26].

2.2.4 On Ergodicity and Finite Sampling Time

The term ergodicity denotes a statistical property of dynamic systems. A system is said to be ergodic if the thermal average over time is equal to the average over all possible configurations, namely that the expectation value of an observable o is

$$\langle o \rangle = \lim_{\mathfrak{T} \to \infty} \frac{1}{\mathfrak{T}} \int_0^{\mathfrak{T}} o(t)\mathrm{d}t \overset{!}{=} \frac{1}{Q} \int o(\boldsymbol{q}, \boldsymbol{p}) \exp\left(-\beta E(\boldsymbol{q}, \boldsymbol{p})\right) \mathrm{d}\boldsymbol{q}\mathrm{d}\boldsymbol{p}. \tag{2.44}$$

This assumption states that the system visits the whole phase space in infinite time. Ergodicity can not be proved for most systems. Therefore we state it as an assumption here. Obviously tracking infinite time is not possible. In computational applications the following approximation is deduced from equation (2.44)

$$\bar{o} = \frac{1}{\mathfrak{T}} \int_0^{\mathfrak{T}} o(t)\mathrm{d}t \approx \frac{1}{Q} \int o(\boldsymbol{q}, \boldsymbol{p}) \exp\left(-\beta E(\boldsymbol{q}, \boldsymbol{p})\right) \mathrm{d}\boldsymbol{q}\mathrm{d}\boldsymbol{p}. \tag{2.45}$$

The assumption that the approximation of equation (2.45) is valid states that the system visits all local minima which are deep enough to have a countable contribution to the right hand side of equation (2.45) within the time $\mathfrak{T}$. If several deep minima are separated by large barriers, $\mathfrak{T}$ has to be chosen very large in order to get a good approximation for the expectation value $\langle o \rangle$. Otherwise the system may stay in one minimum the whole time, and calculations by equation (2.45) will not take into account the contribution of other minima. In many realistic systems barriers between minima are too high for reasonable sampling of the whole system within computational time. For these cases computational methods which allow the system to leave the local pond more easily have to be applied. A method developed to deal with this problem is replica exchange simulation[27] or the application of constraints in the essential subspace.[28] However, supposed knowledge about the locations of ponds and barriers exists, rare event methods, like umbrella sampling,[29] methadynamics,[30] transition path sampling[31,32] and many others, can be used.

For both assumptions, ergodicity itself and that the approximation of equation (2.45) is valid, no conditions exist.

2.2.4.1 Discrete Sampling

In molecular dynamics simulations we cannot calculate the value of the observable $o(t)$ at each time, because equations of motions are integrated by time steps. The integral in equation (2.45) has to approximated by a discrete sum. In this work I use the very simple end point rule.

$$\bar{o} = \frac{1}{\mathrm{T}} \int_0^{\mathrm{T}} o(t) \mathrm{d}t = \frac{1}{N \Delta t} \sum_{i=1}^{N} o(i \cdot \Delta t) \cdot \Delta t + \frac{1}{N \Delta t} \mathcal{O}(\Delta t) \approx \frac{1}{N} \sum_{i=1}^{N} o_i \tag{2.46}$$

Δt cancels out in the sum and $o_i = o(i \cdot \Delta t)$ is just an abbreviation. Of course, more accurate quadrature rules exist. However, since the sampling error decreases with $1/\sqrt{N}$, as we will see in the next chapter, the error is dominated by sampling.

2.2.4.2 Central Limit Theorem

Besides systematical errors, one also needs to take care with stochastic fluctuations. Their influence on the error of the expectation value can be estimated by the variance

$$\sigma_N^2 = \lim_{M \to \infty} \frac{1}{M} \sum_{j=1}^{M} \left(\bar{o}_N - \langle o \rangle \right)^2 , \tag{2.47}$$

where σ_N is the variance of the mean values $\bar{o}_N$ gained by sampling over N samples. In other words, if one were to calculate $\bar{o}_N$ infinite times, the values would be distributed with a variance of σ_N. The central limit theorem states that

$$\sigma_N = \frac{\sigma}{\sqrt{N}} \tag{2.48}$$

where σ is the variance of the distribution of o_i. Equation (2.48) is only true for statistical, not correlated samples.

As a practical consequence of the central limit theorem, we have to quadratically increase the number of samples if we want to reduce the error of the approximation $\bar{o} \approx \langle o \rangle$, e. g. we have to use 100 times more samples if we want to increase the precision of the sampling result by one digit.

2.3 Computational Methods

2.3.1 Umbrella Integration

In the rest of the work, the configuration space is always described in Cartesian coordinates. The free energy landscape will always be expressed as a function of coordinates of a set of R atoms. The subspace of these $M = 3 \times R$ Cartesian coordinates is not integrated out in equation (2.32) and will be called reaction coordinate space (RCS). A point in the RCS is denoted by the vector $\boldsymbol{q}^{\mathrm{RCS}}$.

The high dimensional integral equation (2.32) is predestined to be calculated by the use of Monte–Carlo or molecular dynamics simulations. Unfortunately the most interesting states, the transition states which are represented by saddle points in the potential energy landscape, are also the configurations which are most unlikely to appear along the path. Sufficient sampling of these rare events by naïve Monte-Carlo integration would be computationally prohibitive.

In this work we use umbrella integration,[16, 33, 34] to get information about the free energy surface around unfavorable configurations. Therefore a quadratic bias of the form

$$w_{\mathrm{b}}(\boldsymbol{q}^{\mathrm{RCS}}) = \frac{K}{2}\left(\boldsymbol{q}^{\mathrm{RCS}} - \boldsymbol{q}^{\mathrm{RCS}}_{\mathrm{ref}}\right)^2 \tag{2.49}$$

is applied, where K is the force constant, and $\boldsymbol{q}^{\mathrm{RCS}}_{\mathrm{ref}}$ the reference value of the reaction coordinate. It has been shown that after sufficient sampling we obtain the free-energy gradient by[16, 33]

$$\boldsymbol{g}(\boldsymbol{q}^{\mathrm{RCS}}) = \nabla_{\mathrm{RCS}} A(\boldsymbol{q}^{\mathrm{RCS}}) = \mathbf{C}^{-1}\frac{1}{\beta}\left(\boldsymbol{q}^{\mathrm{RCS}} - \left\langle \boldsymbol{q}^{\mathrm{RCS}} \right\rangle\right) - K(\boldsymbol{q}^{\mathrm{RCS}} - \boldsymbol{q}^{\mathrm{RCS}}_{\mathrm{ref}}) \ , \tag{2.50}$$

where $\mathbf{C}$ is the covariance matrix of $\boldsymbol{q}^{\mathrm{RCS}}$ and $\left\langle \boldsymbol{q}^{\mathrm{RCS}} \right\rangle$ is the mean value of $\boldsymbol{q}^{\mathrm{RCS}}$ in the biased ensemble. Consequently, the gradient at the mean value is[16]

$$\boldsymbol{g}(\left\langle \boldsymbol{q}^{\mathrm{RCS}} \right\rangle) = -K\left(\left\langle \boldsymbol{q}^{\mathrm{RCS}} \right\rangle - \boldsymbol{q}^{\mathrm{RCS}}_{\mathrm{ref}}\right). \tag{2.51}$$

The Hessian is[16]

$$\mathbf{H} = \nabla\nabla A(\boldsymbol{q}^{\mathrm{RCS}}) = \frac{1}{\beta}\mathbf{C}^{-1} - K\mathbb{1} \tag{2.52}$$

with the unit matrix $\mathbb{1}$. With the RCS atoms restrained, we obtain the gradient as a M-dimensional vector $\boldsymbol{g}(\boldsymbol{q}^{\mathrm{RCS}})$ and the corresponding $M \times M$ Hessian matrix $\mathbf{H}$, where $M = 3 \times R$ the number coordinates in the RCS.

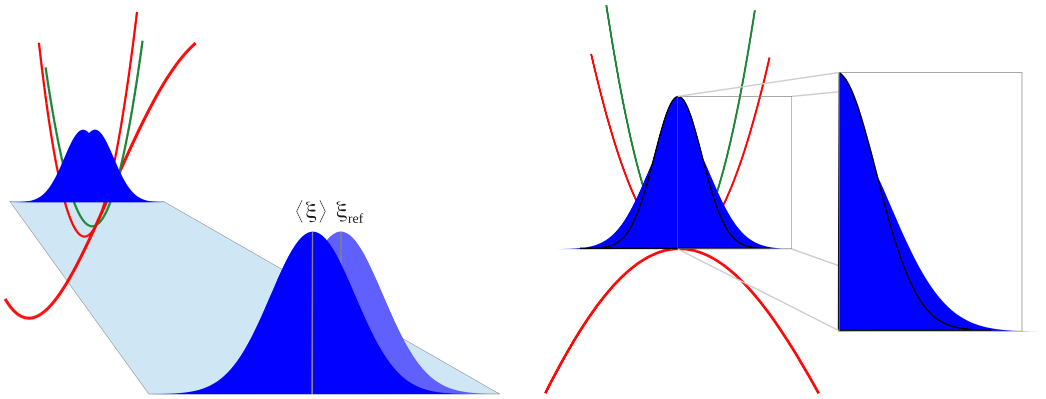

(a) The shift of the expectation value of the distribution can be used to calculate the gradient.

(b) The variance of the umbrella distribution can be used to calculate the curvature and accordingly the Hessian of the free energy surface.

Figure 2.4: Sketch to illustrate umbrella integration. The thick red line symbolises the underlying free energy potential. The green line is the non-physical bias used for umbrella sampling and the thin red line shows the resulting potential which is the sum of bias and underlying potential. The light blue distribution is what we expect without underlying potential. Its expectation value is equal to the minima of the quadratic bias. The dark blue distribution is what we actually get by umbrella sampling.

Principles for calculating gradients and Hessians of a free energy landscape are illustrated in the sketches of figure 2.4. Higher order deviations can in principle be calculated from higher order moments of the umbrella sampling distribution. However, since these moments are more strongly effected by noise, it is usually cheaper to get desired information from several umbrella sampling runs at different positions.[35]

2.3.2 Nudged Elastic Band Simulations*

Different classes of methods exist for finding an intrinsic reaction coordinate. Chain of states methods approximate it as a series of replicas of the system, so-called images. They include the nudged elastic band[37–40] (NEB) method and variants thereof,[41] string methods,[42–44] and conjugate peak refinement.[45] This work builds on NEB. A good introduction to the NEB method can be found in reference 46.

The potential energy is $V(\boldsymbol{R}_i)$, where $\boldsymbol{R}_i$ is the position of the i^{th} image along the path. The force $\boldsymbol{F}_i = -\nabla V(\boldsymbol{R}_i)$ acting on each image is calculated. The aim is to minimize the component of the force perpendicular to the path. The simplest way to do so would be to solve the equation

$$0 \overset{!}{=} (1 - \hat{\boldsymbol{\tau}}_i \hat{\boldsymbol{\tau}}_i^{\mathrm{T}})\boldsymbol{F}_i, \tag{2.53}$$

for each image where $\hat{\boldsymbol{\tau}}_i$ is the unit vector tangential to the path. The projection operator is $\hat{\boldsymbol{\tau}}\hat{\boldsymbol{\tau}}^{\mathrm{T}}$. Several schemes to approximate the tangent vector for discretized paths have been developed.[38,46] Here we stick to the upwind scheme, used in the improved tangent NEB method[38]

$$\boldsymbol{\tau}_i = \begin{cases} \boldsymbol{\tau}_i^+ = \boldsymbol{R}_{i+1} - \boldsymbol{R}_i & \text{if} \quad V_{i+1} > V_i > V_{i-1} \\ \boldsymbol{\tau}_i^- = \boldsymbol{R}_i - \boldsymbol{R}_{i-1} & \text{if} \quad V_{i+1} < V_i < V_{i-1} \end{cases}, \tag{2.54}$$

where $V_i = V(\boldsymbol{R}_i)$ is the corresponding potential energy of image i. If an image has a lower ($V_{i+1} > V_i < V_{i-1}$) or higher ($V_{i+1} < V_i > V_{i-1}$) energy than both its neighbors, a linear combination of both differences is used

$$\boldsymbol{\tau}_i = \begin{cases} \Delta V_i^{\max} \boldsymbol{\tau}_i^+ + \Delta V_i^{\min} \boldsymbol{\tau}_i^- & \text{if} \quad V_{i+1} > V_{i-1} \\ \Delta V_i^{\min} \boldsymbol{\tau}_i^+ + \Delta V_i^{\max} \boldsymbol{\tau}_i^- & \text{if} \quad V_{i+1} < V_{i-1} \end{cases} \tag{2.55}$$

with

$$\begin{aligned} \Delta V_i^{\max} &= \max\left(|V_{i+1} - V_i|, |V_{i-1} - V_i|\right) \\ \Delta V_i^{\min} &= \min\left(|V_{i+1} - V_i|, |V_{i-1} - V_i|\right). \end{aligned} \tag{2.56}$$

---

*Parts of this chapter were published in reference 36: M. U. Bohner, J. Meisner and J. Kästner: "A Quadratically-Converging Nudged Elastic Band Optimizer", *J. Chem. Theory Comput.* **9**, 3498 (2013).

In the following we use the general expression $\boldsymbol{\tau}_i = a\boldsymbol{\tau}_i^+ + b\boldsymbol{\tau}_i^-$ and choose a and b according to the case.

An optimizer based on equation (2.53) would cause many images to gather near the minima. This problem can be addressed by introducing a penalty, which leads to an equal distribution of the images. In NEB, non-physical spring forces between the images are used. However, this force, unlike a real spring, should only act tangentially to the path. Altogether in improved-tangent NEB, the force on image i to be minimized reads[38]

$$\boldsymbol{F}_i^{\text{NEB}} = k\left(\left|\tau_i^+\right| - \left|\tau_i^-\right|\right)\hat{\boldsymbol{\tau}}_i + (1 - \hat{\boldsymbol{\tau}}_i\hat{\boldsymbol{\tau}}_i^{\text{T}})\boldsymbol{F}_i^{\text{t}}, \tag{2.57}$$

where k denotes the spring constant. We introduced the superscripts NEB and t to discriminate between the NEB force and the true force $\boldsymbol{F}^{\text{t}} = -\nabla V$. The spring, or penalty, term $k\left(\left|\tau_i^+\right| - \left|\tau_i^-\right|\right)\hat{\boldsymbol{\tau}}_i$ reduces the difference between the distances to both neighbor images but not the distances themselves. A humble attempt to illustrate the NEB force can be found in figure 2.5. This is necessary to avoid artificially shortening the NEB path (corner cutting). The penalty term should act on physically meaningful differences between the images. Translation or rotations e. g. of the whole system do not have chemical meaning. Thus molecular geometries have to be superimposed to remove any translation or rotation between the images.[46]

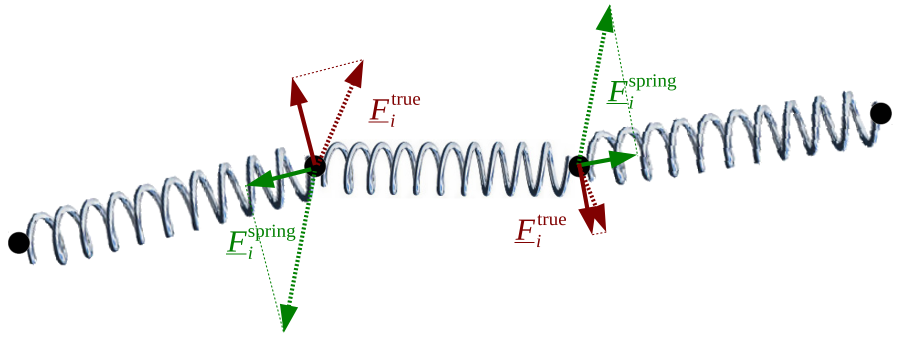

Figure 2.5: Sketch to illustrate NEB force of equation (2.57). Images are connected with non-physical spring forces. Spring force does not punish path length, like real world springs, but the unequal distribution of images along the path. Only the component of the true force acting perpendicular to the path is included in NEB force.

Part II

RESULTS

3

METHODS

This chapter explains improvements archived

Contents

3.1 Serial Algorithm to Find Minimum Free Energy Paths*

The minimum free energy path (MFEP) leads over saddle points of the free energy landscape and follows the gradient down to the minima.[1,2] This imposes, starting with the search for saddle points. The algorithm explained in this chapter uses a Newton–Raphson iteration to converge to the next saddle point in the free energy landscape. Once a saddle point is found up to a certain precision, the corresponding MFEP can be reconstructed by following the gradient down to the minima.

We have seen how biased molecular dynamics, namely umbrella sampling, can be used to calculate gradients and Hessians of the free energy landscape via umbrella integration. Both values enter the iterative search for the closest stationary point using the Newton–Raphson method:

$$\boldsymbol{q}_{n+1}^{\mathrm{RCS}} = \boldsymbol{q}_{n}^{\mathrm{RCS}} - \mathbf{H}^{-1}(\boldsymbol{q}_{n}^{\mathrm{RCS}}) \cdot \boldsymbol{g}(\boldsymbol{q}_{n}^{\mathrm{RCS}}). \tag{3.1}$$

Due to statistical noise the components of the gradient as well as the Hessian corresponding to overall rotational and translational movements are generally non-zero. Therefore the gradient is orthogonalized to translations and rotations by

$$\tilde{\boldsymbol{g}}(\boldsymbol{q}^{\mathrm{RCS}}) = \boldsymbol{g}(\boldsymbol{q}^{\mathrm{RCS}}) - \sum_{k=1}^{6} \hat{\boldsymbol{t}}_k(\hat{\boldsymbol{t}}_k \cdot \boldsymbol{g}(\boldsymbol{q}^{\mathrm{RCS}})), \tag{3.2}$$

where $\hat{\boldsymbol{t}}_k$ are the unit vectors of translations and rotations, which can be obtained algebraically from $\boldsymbol{q}^{\mathrm{RCS}}$. Furthermore the overlap of $\hat{\boldsymbol{t}}_k$ with the eigenvectors of the Hessian $\hat{\boldsymbol{v}}_i$ is calculated, $\varepsilon_i = \sum_{k=1}^{6} (\hat{\boldsymbol{v}}_i \cdot \boldsymbol{t}_k)^2$. The Newton–Raphson step in equation (3.1) is replaced by

$$\boldsymbol{q}_{n+1}^{\mathrm{RCS}} = \boldsymbol{q}_{n}^{\mathrm{RCS}} - \sum_{i \notin \{i_1 \ldots i_6\}} \hat{\boldsymbol{v}}_i \frac{1}{\lambda_i} \left(\hat{\boldsymbol{v}}_i \cdot \tilde{\boldsymbol{g}}(\boldsymbol{q}^{\mathrm{RCS}})\right), \tag{3.3}$$

so that the summation runs from one to $3S$ but omits the indices of the six largest ε_i. $\hat{\boldsymbol{v}}_i$ denote the eigenvectors and λ_i the corresponding eigenvalues of the Hessian at the point $\boldsymbol{q}_n^{\mathrm{RCS}}$. In all cases tested this was sufficient to remove rotational and translational noise from the step.

---

*Parts of this chapter were published in reference 36: M. U. Bohner and J. Kästner: "An algorithm to find minimum free-energy paths using umbrella integration", *J. Chem. Phys.* **137**, 034105 (2012).

The reference point of an umbrella sampling simulation is $\boldsymbol{q}_n^{\mathrm{RCS}}$. Essentially, equation (3.3) contains a pseudo-inverse of the Hessian rather than its full inverse. The approximations for the gradient and the Hessian are most accurate at the average coordinates of the biased sampling, $\left\langle \boldsymbol{q}_n^{\mathrm{RCS}} \right\rangle$. Thus, the Newton–Raphson step is performed relative to the average coordinates of the current step to provide the reference coordinates for the next step $\boldsymbol{q}_{n+1}^{\mathrm{RCS}}$. The adjusted formula for the Newton–Raphson iteration reads

$$\boldsymbol{q}_{n+1}^{\mathrm{RCS}} = \left\langle \boldsymbol{q}_n^{\mathrm{RCS}} \right\rangle - \sum_{i \notin \{i_1 \ldots i_6\}} \hat{\boldsymbol{v}}_i \frac{1}{\lambda_i} \left(\hat{\boldsymbol{v}}_i \cdot \tilde{\boldsymbol{g}}(\boldsymbol{q}_n^{\mathrm{RCS}}) \right). \tag{3.4}$$

The algorithm is converged to a stationary point if $\boldsymbol{q}_{n+1}^{\mathrm{RCS}}$ equals $\left\langle \boldsymbol{q}_n^{\mathrm{RCS}} \right\rangle$. A proper choice of the initial values is required for convergence to a saddle point on the free-energy landscape.

The whole algorithm is explained in figure 3.1. One starts at an initial point in the RCS, where umbrella integration using a quadratic bias is performed. A subroutine subtracts the rotational and translational components from the gradient as described in equation (3.2). Another one excludes the eigenvalues of the Hessian matrix which are dominated by rotational and translational character, equation (3.3). If the resulting gradient is smaller than a pre-defined criterion the algorithm is assumed to be converged. If not, a Newton–Raphson step is performed and the result is used as reference coordinates of the next iteration.

Once a saddle point is found the corresponding MFEP is reconstructed by following the gradient down to the associated minima. However, at the saddle point the gradient is zero, the MFEP follows the transition mode. Integration of the path starts by

$$\boldsymbol{q}^{\mathrm{RCS}}(\pm\Delta s_0) = \boldsymbol{q}^{\mathrm{RCS}}(0) \pm \hat{\boldsymbol{v}}_1 \Delta s_0, \tag{3.5}$$

where Δs_0 is a pre-defined step length of the first step along the path, $\boldsymbol{q}^{\mathrm{RCS}}(0)$ the coordinates of the saddle point and $\hat{\boldsymbol{v}}_1$ is the normalized eigenvector associated with the negative eigenvalue of $\mathbf{H}$. The MFEP can be followed by integration of

$$\mathrm{d}\boldsymbol{s} = \mathrm{d}\boldsymbol{q}^{\mathrm{RCS}}(s) = -\frac{\boldsymbol{g}(\boldsymbol{q}^{\mathrm{RCS}}(s))}{|\boldsymbol{g}(\boldsymbol{q}^{\mathrm{RCS}}(s))|}\, \mathrm{d}s, \tag{3.6}$$

where s represents a scalar parameter describing the progress along the path. Therefore the gradient is approximated by a Taylor expansion to second order, equation (2.50). Obviously this approximation is only valid in a small area around $\left\langle \boldsymbol{q}^{\mathrm{RCS}} \right\rangle$ of the corresponding umbrella sampling simulation. Therefore subsequent

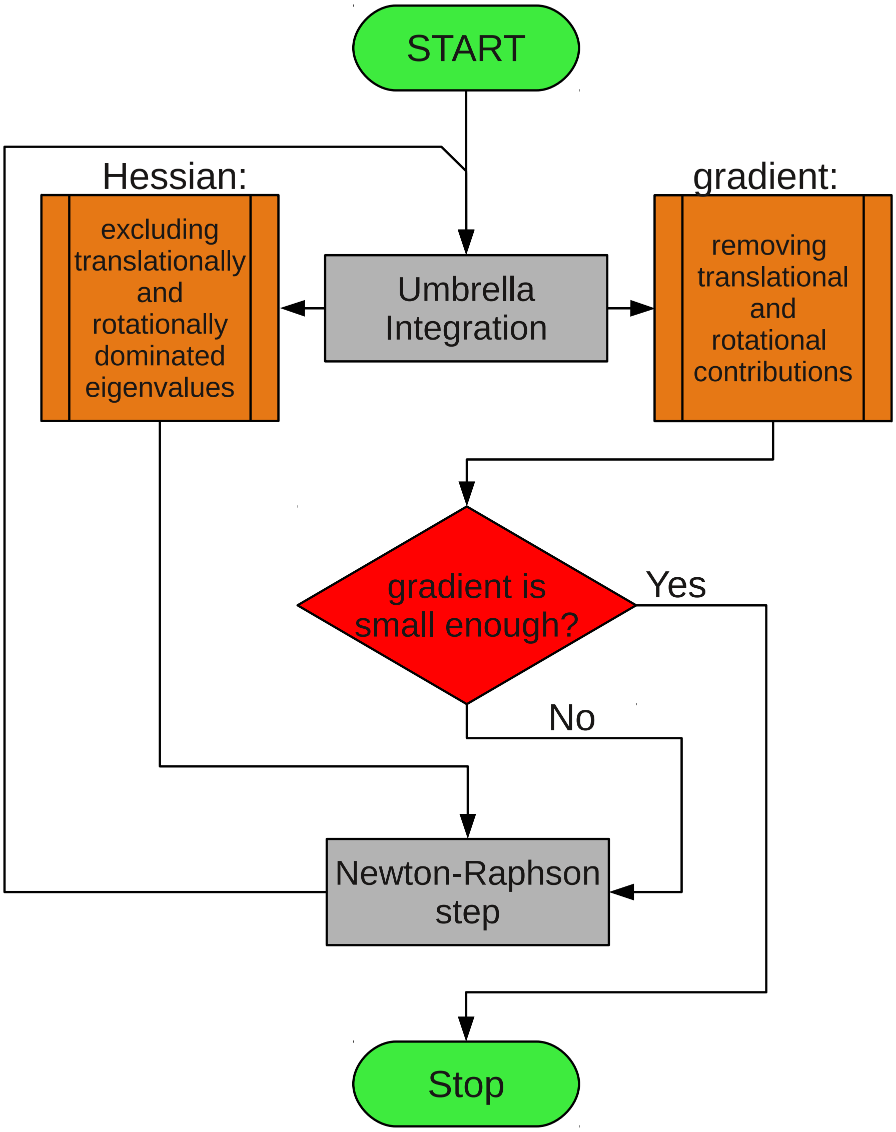

Figure 3.1: Flow chart to illustrate the algorithm to find the free-energy saddle points

runs of umbrella sampling have to be done. This reduces the whole problem from a multidimensional surface scan to one dimension.

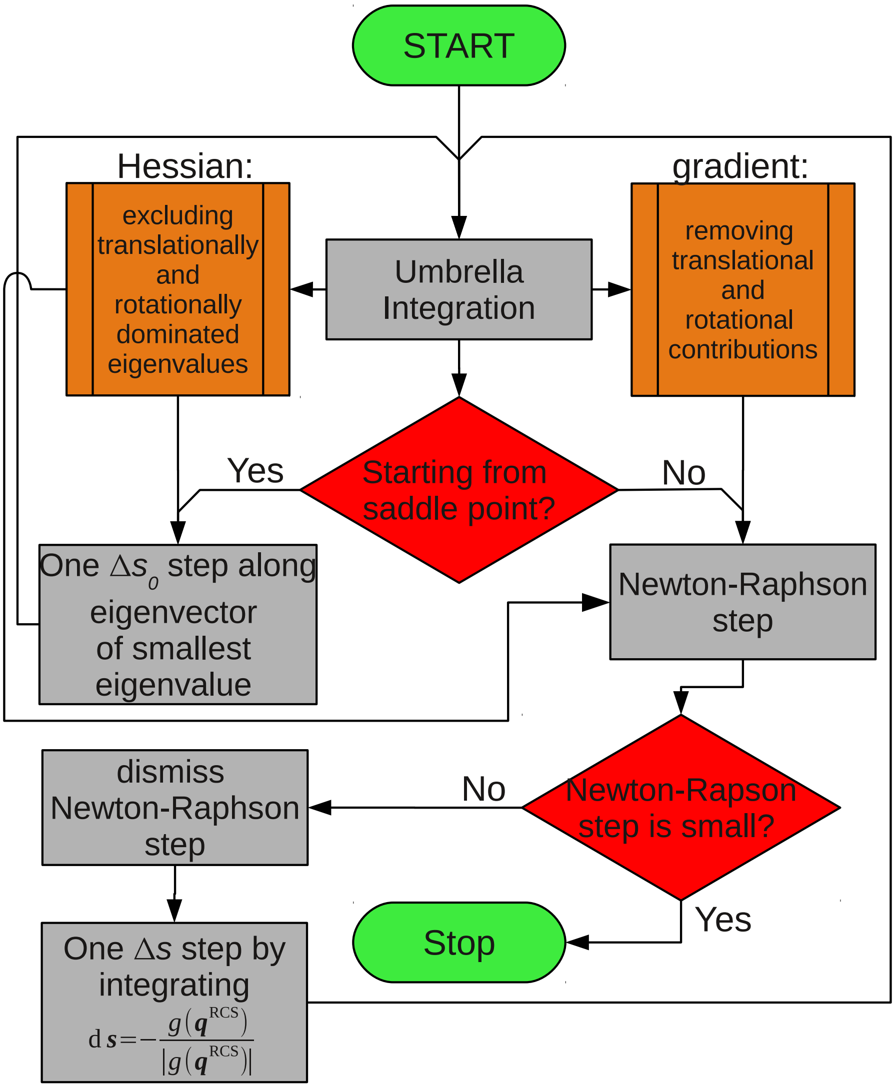

Figure 3.2: Flow chart of the algorithm to reconstruct the MFEP

The algorithm to follow the MFEP is explained in figure 3.2. The same process is used for umbrella integration and for the removal of rotational and translational contributions from the gradient and the Hessian as described in equations (3.2) and (3.3). On the saddle point the algorithm simply follows the direction of the eigenvector of negative eigenvalue of the Hessian for one step of the length Δs_0. Δs_0 is an input parameter. The result is used as reference coordinates $\boldsymbol{q}_{\mathrm{ref}}^{\mathrm{RCS}}$ for the next umbrella sampling run. In the following proceeder $\boldsymbol{g}(\boldsymbol{q}_{\mathrm{ref}}^{\mathrm{RCS}})$ is calculated by equation (2.50) and used by equation (3.6). Equation (3.6) itself is solved stepwise using an explicit Euler algorithm. The path is followed for the length Δs until another umbrella sampling run is performed. Δs is an input parameter as well. For flat saddle points it turned out to be useful to use large $\Delta s_0 > \Delta s$. If a Newton–Raphson step to the minimum is shorter than $\varepsilon\Delta s$, the Newton–Raphson step is performed and the path search is finished. ε is a scalar input parameter, $\varepsilon < 1$.

Finally, the height of the reaction barrier is to be determined. The free-energy difference for each step is given by

$$\Delta_n A^{\mathrm{RCS}} = A(\boldsymbol{q}_{n+1}^{\mathrm{RCS}}) - A(\boldsymbol{q}_n^{\mathrm{RCS}}). \tag{3.7}$$

Umbrella integration with reference $\boldsymbol{q}_n^{\mathrm{RCS}}$ obtains the free energy landscape most accurately around $\left\langle \boldsymbol{q}_n^{\mathrm{RCS}} \right\rangle$, which is located between $\boldsymbol{q}_n^{\mathrm{RCS}}$ and $\boldsymbol{q}_{n+1}^{\mathrm{RCS}}$. Therefore to calculate the difference between $A(\boldsymbol{q}_n^{\mathrm{RCS}})$ and $A(\boldsymbol{q}_{n+1}^{\mathrm{RCS}})$ in equation (3.7) run n was used. The difference along the whole path $\Delta A^{\mathrm{RCS}} = A^{\mathrm{RCS}}(s = 0) - A^{\mathrm{RCS}}(s = s^{\mathrm{RS}})$ is the sum of all $\Delta_n A^{\mathrm{RCS}}$. s is set to zero at the saddle point and s^{RS} at the minimum (reactant state).

Since constraints are applied to the coordinates of S atoms, the differences of the potential of mean force in the RCS are obtained. This excludes the entopic contributions of the coordinates within the RCS. Instead of $A^{\mathrm{RCS}}(\boldsymbol{q}^{\mathrm{RCS}})$, which is a function of $3S$ coordinates, one aims at $A^s(s)$ which is a function of the one-dimensional arc length s of the path:

$$A^s(s) = -\frac{1}{\beta} \ln \int \exp[-\beta A^{\mathrm{RCS}}(\boldsymbol{q}^{\mathrm{RCS}})] d^{3S-7} q_\perp. \tag{3.8}$$

The integration is performed over the $3S - 7$ degrees of freedom $\boldsymbol{q}_\perp$ orthogonal to the translations and rotations and orthogonal to the tangent of the path. A basis of $\boldsymbol{q}_\perp$ can be found algebraically by e.g., Gram–Schmidt orthogonalization. The basis vectors provide the column vectors of a $(3S - 7) \times (3S)$ transformation matrix $\mathbf{U}$:

$$\boldsymbol{q}_\perp = \mathbf{U}^T \boldsymbol{q}^{\mathrm{RCS}}, \quad \boldsymbol{q}^{\mathrm{RCS}} = \mathbf{U}\boldsymbol{q}_\perp. \tag{3.9}$$

The free energy $A^{\mathrm{RCS}}(\boldsymbol{q}^{\mathrm{RCS}})$ in (3.8) is expanded to second order perpendicular to the path:

$$A^{\mathrm{RCS}}(\boldsymbol{q}^{\mathrm{RCS}}) = A^{\mathrm{RCS}}(\boldsymbol{q}^{\mathrm{RCS}}(s)) + \frac{1}{2}\boldsymbol{q}_\perp^T \mathbf{H}_\perp \boldsymbol{q}_\perp \tag{3.10}$$

with $\mathbf{H}_\perp = \mathbf{U}^T \mathbf{H}^{\mathrm{RCS}} \mathbf{U}$. The $(3S-7) \times (3S-7)$ matrix $\mathbf{H}_\perp$ is positive definite by construction. Using (3.10) turns the integral in (3.8) into a Gaussian integral, which results in

$$A^s(s) = A^{\mathrm{RCS}}(\boldsymbol{q}^{\mathrm{RCS}}(s)) - \frac{1}{\beta} \ln \left(\sqrt{\frac{\pi^{3S-7} 2^{3S-7}}{\beta^{3S-7} \det \mathbf{H}_\perp(s)}} \right). \tag{3.11}$$

Free-energy differences are obtained as

$$\begin{aligned} \Delta A^s = A^s(s=0) - A^s(s=s^{\mathrm{RS}}) = \\ A^{\mathrm{RCS}}(s=0) - A^{\mathrm{RCS}}(s=s^{\mathrm{RS}}) + \frac{1}{2\beta} \ln \frac{\det \mathbf{H}_\perp(s=0)}{\det \mathbf{H}_\perp(s=s^{\mathrm{RS}})}. \end{aligned} \tag{3.12}$$

For the case that more than one saddle point is found between two minima, the path over each barrier has to be calculated. If the barrier heights differ a lot, it can be assumed that the path over the lower barrier dominates the reaction.

3.1.1 Application: Alanine Dipeptide

A simple example for free-energy simulations is N-acetyl-alanine-N'methylamide, commonly named alanine dipeptide. In the gas phase this molecule has three stable configurations, C_5, $\mathrm{C}_7^{\mathrm{eq}}$, and $\mathrm{C}_7^{\mathrm{ax}}$. The last one is shown in figure 3.3. The method described above is applied using MD simulations with the peptide placed in vacuum. The CHARMM22[8] forcefield is used. A Nosé–Hoover chain[11–14] thermostat generates a canonical ensemble at $T = 300$ K. The thermostat has a chain length of 4 and a response time of 20 fs. The actual integration of Newton's equation of motion is performed with a reversible non-iterative leapfrog-type integrator with time steps of 1 fs. The calculations use DL_POLY[47] within the ChemShell[48] program.

The Cartesian coordinates of the 5 backbone atoms, highlighted as spheres in figure 3.3, are assigned to the RCS. The starting points of the saddle-point searches are taken from a nudged-elastic band[37–39] path obtained on the potential-energy surface. The force constant K is chosen between 0.1 and 0.3 atomic units (≈ 93758 to 281275 kJ mol^{-1} nm^{-2}). The number of time steps sampled is adjusted to the magnitude of the gradient: $10^9/|\boldsymbol{g}(\boldsymbol{q}^{\mathrm{RCS}})|^2$(with a minimum of $5 \cdot 10^5$). Here the gradient $\boldsymbol{g}(\boldsymbol{q}^{\mathrm{RCS}})$ in kJ mol^{-1} nm^{-1} is taken from the previous umbrella integration run. The background of this choice is that the gradient has to be significantly larger than the noise and the error is expected to decrease with the square root of the number of time steps as mentioned in section 2.2.4.2. The saddle point search is accepted as converged if the root mean square of the gradient is below 10 kJ mol^{-1} nm^{-1}.

An example of a transition state search, the one between C_7^{eq} and C_7^{ax}, is shown in figure 3.4. Since a 15-dimensional space can not be illustrated, a projection into the two-dimensional space of the backbone torsion angles Ψ and Φ, defined in figure 3.3, is used.

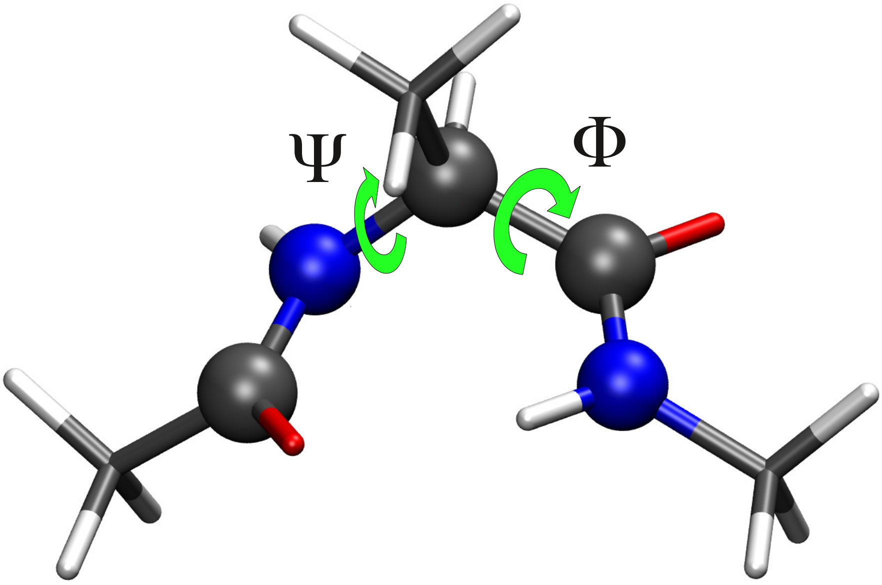

Figure 3.3: The minimum structure of C_7^{ax} of the alanine dipeptide. The backbone torsion angles Ψ and Φ are indicated. The backbone atoms belonging to the RCS are highlighted as spheres. Graphic generated using the visualization tool VMD.[49]

To integrate the MFEP the fixed values of $K = 0.2$ atomic units ($\approx$187517 kJ mol^{-1} nm^{-2}) and 10^6 time steps were used. The first step length is set to $\Delta s_0 = 0.008$ nm except for the saddle point between C_5 and C_7^{eq}, where $\Delta s_0 = 0.016$ nm had to be chosen. For following steps the lengths are always $\Delta s = 0.008$ nm. The resulting 15-dimensional paths are again projected into the two-dimensional space of the two backbone torsion angles. This is plotted over the level curve of the potential-energy surface in figure 3.5.

The transition states and minima obtained by this method are in good agreement with those from Ψ and Φ as active space,[16] see table 3.1. The detailed path

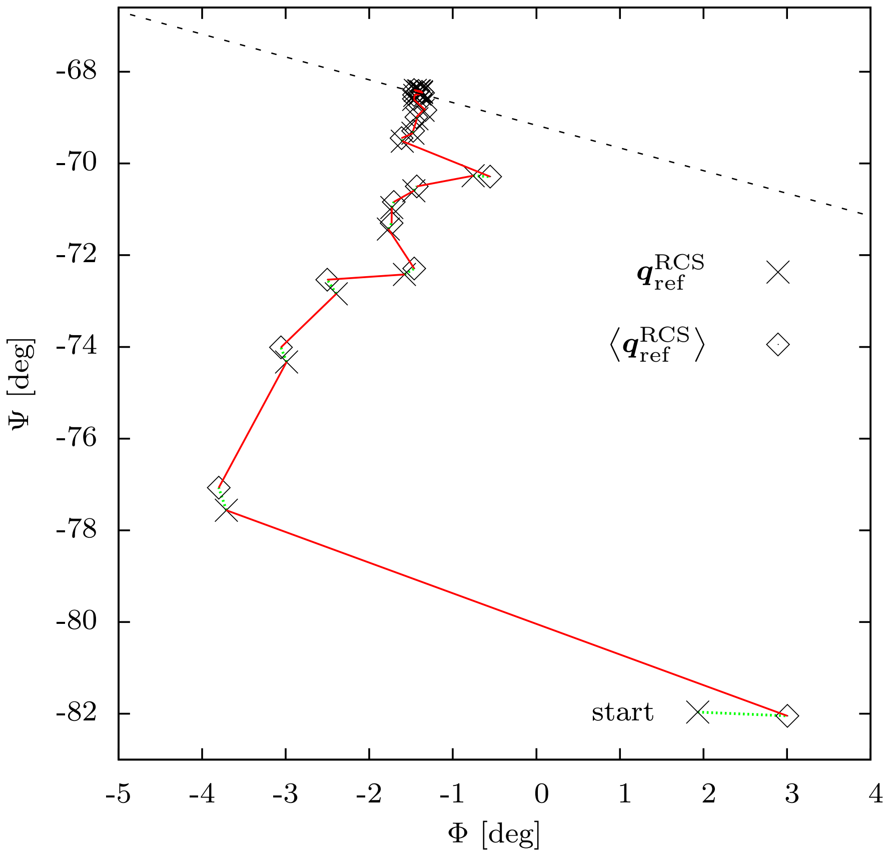

Figure 3.4: Search path of the saddle point between C_7^{eq} and C_7^{ax} of the alanine dipeptide. The reference coordinates for each umbrella sample run $\boldsymbol{q}_{\text{ref}}^{\text{RCS}}$ are marked with × signs. The mean value of each umbrella sampling run $\left\langle \boldsymbol{q}^{\text{RCS}} \right\rangle$ is marked with ⋄ symbols. The umbrella sampling displacements are shown by green dotted lines, while the Newton–Raphson steps from $\left\langle \boldsymbol{q}^{\text{RCS}} \right\rangle$ to the next reference coordinates $\boldsymbol{q}_{\text{ref}}^{\text{RCS}}$ is drawn by red solid lines. The dashed black line represents the MFEP.

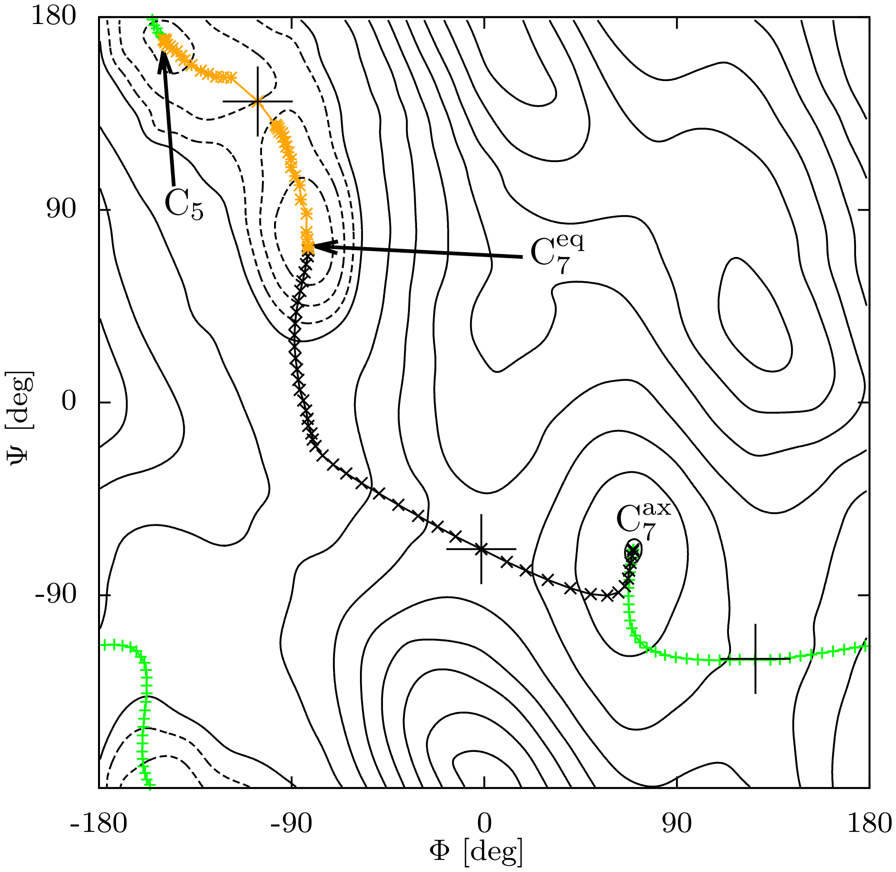

Figure 3.5: Two-dimensional projection to the backbone torsion angles of the paths calculated with the serial algorithm. The level curves represent the potential-energy surface as a function of Φ and Ψ. The big crosses represent the saddle points found by Newton–Raphson search. The symbols along the path mark the reference coordinates for each umbrella sampling in the path search. The minima C_7^{ax}, C_7^{eq}, and C_5 are labeled.

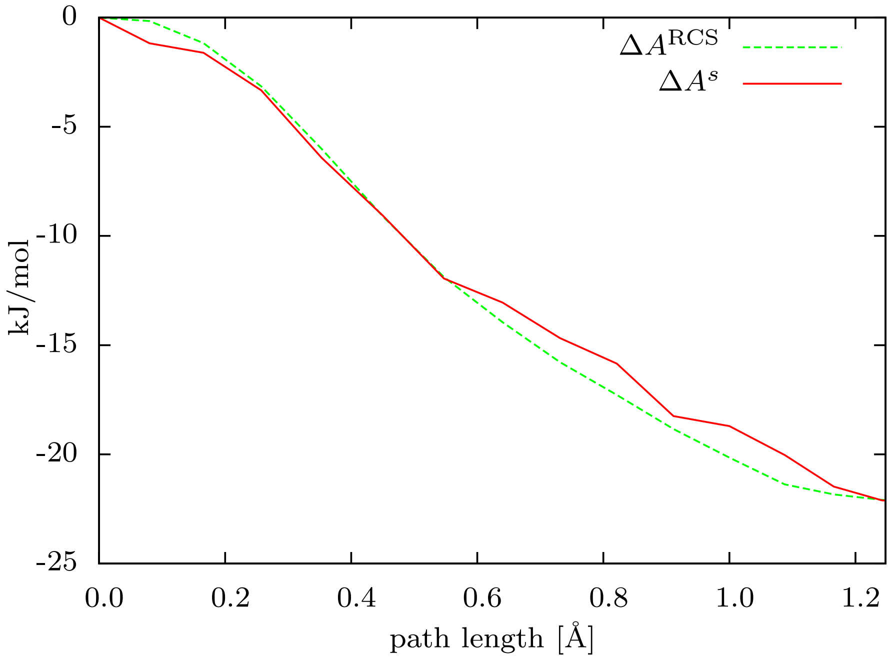

Figure 3.6: Free energy along the MFEP. The graph starts at the saddle point between $\mathrm{C}_7^{\mathrm{ax}}$ and C_5 and ends at $\mathrm{C}_7^{\mathrm{ax}}$. The path length is approximated by the sum of the beelines between the reference coordinates. The green dashed line shows the result neglecting the entropic contribution of the RCS, the red solid line shows the corrected values.

characteristics between saddle point and minimum are hard to compare because different RCSs were used.

The free energy along the path from the saddle point between $\mathrm{C}_7^{\mathrm{ax}}$ and C_5 to the minimum $\mathrm{C}_7^{\mathrm{ax}}$ is shown in figure 3.6. The green dashed line shows the result neglecting the entropic contribution of the RCS, the red solid line shows the corrected values. The diagram shows that this correction does not change the qualitative result. The whole difference from this saddle point to $\mathrm{C}_7^{\mathrm{ax}}$ corresponds to the barrier height for a reaction from $\mathrm{C}_7^{\mathrm{ax}}$ to C_5.

Barrier			ΔA^{Φ}, Ref[16]	ΔA^{s}	ΔA^{RCS}
$\mathrm{C}_7^{\mathrm{ax}}$	→	$\mathrm{C}_7^{\mathrm{eq}}$	25.31 ± 0.32	26.06	23.92
$\mathrm{C}_7^{\mathrm{eq}}$	→	$\mathrm{C}_7^{\mathrm{ax}}$	36.92 ± 0.37	33.40	32.61
$\mathrm{C}_7^{\mathrm{ax}}$	→	C_5	22.27 ± 0.31	22.11	22.09
C_5	→	$\mathrm{C}_7^{\mathrm{ax}}$	31.98 ± 0.35	28.98	27.57

Table 3.1: Free-energy barrier in kJ mol^{-1} along the MFEP compared to literature data along Φ.[16]

3.2 Nudged Elastic Band Optimisations

3.2.1 Quadratically Converging Nudged Elastic Band Algorithm[†]

The root of a multidimensional function $\boldsymbol{F}(\boldsymbol{R})$ can be iteratively approached using the Newton–Raphson method

$$\boldsymbol{R}_{n+1} = \boldsymbol{R}_n - \mathbf{J}^{-1}\boldsymbol{F}(\boldsymbol{R}), \tag{3.13}$$

where n is the number of the iteration and $\mathbf{J}$ is the Jacobian matrix of the function. Here we are looking for the root of the NEB force, equation (2.57). In many optimisation problems a scalar potential function can be found, the minimum of which is sought in the optimisation. Then the Hessian, the symmetric matrix of second derivatives of the potential function, can be used in Newton–Raphson optimisations, e. g. equation (3.1). However, such a potential is not available for the NEB force, which is why we have to use the Jacobian matrix, which in general is not symmetric.

Let us define an $(N{\cdot}M)$-dimensional super vector, where N is the number of images and M the number of coordinates for each image. For a molecule with 5 atoms M

[†] Parts of this chapter were published in reference 36: M. U. Bohner, J. Meisner and J. Kästner: "A Quadratically-Converging Nudged Elastic Band Optimizer", *J. Chem. Theory Comput.* **9**, 3498 (2013).

will in general be $M = 15$. This super vector reads $\mathbf{F} = ((\boldsymbol{F}_1^{\mathrm{NEB}})^{\mathrm{T}}, (\boldsymbol{F}_2^{\mathrm{NEB}})^{\mathrm{T}}, (\boldsymbol{F}_3^{\mathrm{NEB}})^{\mathrm{T}}, \ldots, (\boldsymbol{F}_N^{\mathrm{NEB}})^{\mathrm{T}})^{\mathrm{T}}$. The Jacobian is divided into sub-matrices

$$\mathbf{J}^{\mathrm{NEB}} = \begin{pmatrix} \mathbf{J}_{1,1}^{\mathrm{NEB}} & \mathbf{J}_{1,2}^{\mathrm{NEB}} & \ldots & \mathbf{J}_{1,N}^{\mathrm{NEB}} \\ \mathbf{J}_{2,1}^{\mathrm{NEB}} & \mathbf{J}_{2,2}^{\mathrm{NEB}} & \ldots & \mathbf{J}_{2,N}^{\mathrm{NEB}} \\ \vdots & \vdots & \ddots & \vdots \\ \mathbf{J}_{N,1}^{\mathrm{NEB}} & \mathbf{J}_{N,2}^{\mathrm{NEB}} & \ldots & \mathbf{J}_{N,N}^{\mathrm{NEB}} \end{pmatrix} \tag{3.14}$$

with the vector gradient

$$\mathbf{J}_{i,j}^{\mathrm{NEB}} = \mathbf{grad}_j\, \boldsymbol{F}_i^{\mathrm{NEB}} = \left(\nabla_{\boldsymbol{R}_j} \otimes \boldsymbol{F}_i^{\mathrm{NEB}}\right)^{\mathrm{T}}, \tag{3.15}$$

where the derivative of the NEB force of image i with respect to the coordinates of image j is calculated and $\boldsymbol{x} \otimes \boldsymbol{y} = \boldsymbol{x}\boldsymbol{y}^{\mathrm{T}}$ denotes the dyadic product. $\mathbf{J}_{i,j}^{\mathrm{NEB}}$ is an $M \times M$ matrix.

To derive the Jacobian of the NEB force in equation (2.57) the following general expressions will be used.

$$\mathbf{grad}\boldsymbol{A} = (\nabla \otimes \boldsymbol{A})^{\mathrm{T}}, \tag{3.16}$$

$$\mathbf{grad}(f\boldsymbol{A}) = \boldsymbol{A} \otimes (\nabla f) + \left[f(\nabla \otimes \boldsymbol{A})\right]^{\mathrm{T}}, \tag{3.17}$$

$$\mathbf{grad}(\boldsymbol{A} \cdot \boldsymbol{B}) = (\mathbf{grad}(\boldsymbol{A}))^{\mathrm{T}} \boldsymbol{B} + (\mathbf{grad}(\boldsymbol{B}))^{\mathrm{T}} \boldsymbol{A}. \tag{3.18}$$

Here $\boldsymbol{A}$ and $\boldsymbol{B}$ are vector-valued and f is a scalar-valued function.

A further ingredient is the gradient of the length of the tangent vector:

$$\mathbf{grad}_j\, |\boldsymbol{\tau}_i^{+/-}| = \frac{1}{2} \frac{1}{|\boldsymbol{\tau}_i^{+/-}|}\, \mathbf{grad}_j \left(\boldsymbol{\tau}_i^{+/-}\right)^2 \tag{3.19}$$

which leads with equation (3.18) to

$$\mathbf{grad}_j\, |\boldsymbol{\tau}_i^{+}| = \frac{1}{|\boldsymbol{\tau}_i^{+}|} \left(\delta_{i+1}^{j} - \delta_i^{j}\right) \mathbb{1} \boldsymbol{\tau}_i^{+} = \hat{\boldsymbol{\tau}}_i^{+} \left(\delta_{i+1}^{j} - \delta_i^{j}\right) \tag{3.20}$$

and, equivalently,

$$\mathbf{grad}_j\, |\boldsymbol{\tau}_i^{-}| = \hat{\boldsymbol{\tau}}_i^{-} \left(\delta_i^{j} - \delta_{i-1}^{j}\right) \tag{3.21}$$

with δ being the Kronecker delta. Further indispensable relations are

$$
\begin{aligned}
-\,\mathbf{grad}_j\, \boldsymbol{F}_i^{\mathrm{t}} =& \mathbf{H}_i^{\mathrm{t}}\delta_i^j = {\mathbf{H}_i^{\mathrm{t}}}^{\mathrm{T}}\delta_i^j, && (3.22)\\
\hat{\boldsymbol{\tau}}_i \otimes \left(\left(\mathbf{grad}_j\, \hat{\boldsymbol{\tau}}_i\right)^{\mathrm{T}} \boldsymbol{F}_i^{\mathrm{t}}\right) =& \left(\hat{\boldsymbol{\tau}}_i \otimes \boldsymbol{F}_i^{\mathrm{t}}\right) \mathbf{grad}_j\, \hat{\boldsymbol{\tau}}_i && (3.23)
\end{aligned}
$$

where $\mathbf{H}_i^{\mathrm{t}}$ denotes the Hessian of the potential $V(\boldsymbol{R}_i)$. A straightforward calculation leads then to

$$
\begin{aligned}
\mathbf{J}_{i,j}^{\mathrm{NEB}} =& -k\hat{\boldsymbol{\tau}}_i \otimes \left\{\hat{\boldsymbol{\tau}}_+(\delta_{i+1}^j - \delta_i^j) - \hat{\boldsymbol{\tau}}_-(\delta_i^j - \delta_{i-1}^j)\right\}\\
&+ \mathbf{H}_i\delta_i^j - \hat{\boldsymbol{\tau}}_i\mathbf{H}_i\hat{\boldsymbol{\tau}}_i\delta_i^j + \left\{(\boldsymbol{F}_i^{\mathrm{t}} \cdot \hat{\boldsymbol{\tau}}_i)\mathbb{1} + \left(\hat{\boldsymbol{\tau}}_i \otimes \boldsymbol{F}_i^{\mathrm{t}}\right)\right.\\
&\left. -k\left(|\boldsymbol{\tau}_+| - |\boldsymbol{\tau}_-|\right)\mathbb{1}\right\} \mathbf{grad}_j\, \hat{\boldsymbol{\tau}}_i. \qquad (3.24)
\end{aligned}
$$

The vector gradient of the unit tangent vector reads

$$
\mathbf{grad}_j\, \hat{\boldsymbol{\tau}}_i = |\boldsymbol{\tau}_i|^{-1}\left(\mathbb{1} - \hat{\boldsymbol{\tau}}_i \otimes \hat{\boldsymbol{\tau}}_i\right) \mathbf{grad}_j\, \boldsymbol{\tau}_i. \qquad (3.25)
$$

Plugging it into equation (3.24) gives

$$
\begin{aligned}
\mathbf{J}_{i,j}^{\mathrm{NEB}} =& -k\hat{\boldsymbol{\tau}}_i \otimes \left\{\hat{\boldsymbol{\tau}}_+(\delta_{i+1}^j - \delta_i^j) - \hat{\boldsymbol{\tau}}_-(\delta_i^j - \delta_{i-1}^j)\right\}\\
&+ \mathbf{H}_i\delta_i^j - \hat{\boldsymbol{\tau}}_i\mathbf{H}_i\hat{\boldsymbol{\tau}}_i\delta_i^j + \mathbf{A} \cdot \mathbf{grad}_j\, \boldsymbol{\tau}_i \qquad (3.26)
\end{aligned}
$$

with

$$
\begin{aligned}
\mathbf{A} =& \left\{\left[\boldsymbol{F}_i^{\mathrm{t}} \cdot \hat{\boldsymbol{\tau}}_i - k\left(|\boldsymbol{\tau}_+| - |\boldsymbol{\tau}^-|\right)\right]\mathbb{1} + \left(\hat{\boldsymbol{\tau}}_i \otimes \boldsymbol{F}_i^{\mathrm{t}}\right)\right\}\\
&\cdot \frac{\mathbb{1} - \hat{\boldsymbol{\tau}}_i \otimes \hat{\boldsymbol{\tau}}_i}{|\boldsymbol{\tau}_i|}. \qquad (3.27)
\end{aligned}
$$

Now we can see that the Jacobian of the NEB force of equation (2.57) is a band matrix since every term contains one of the Kronecker deltas $\{\delta_{i-1}^j, \delta_i^j, \delta_{i+1}^j\}$. However, it must be kept in mind that the indices i and j do not determine a single element but an $M \times M$ submatrix.

While $\hat{\boldsymbol{\tau}}_i$ depends on the following case distinctions, equation (3.27) provides $\mathbf{A}$ for all cases.

Case: $V_{i+1} > V_i > V_{i-1}$

$\boldsymbol{\tau}_i = \boldsymbol{\tau}_i^+ = \boldsymbol{R}_{i+1} - \boldsymbol{R}_i$. The vector gradient $\mathbf{grad}_j\,\boldsymbol{\tau}_i^+$ reads

$$\mathbf{grad}_j\,\boldsymbol{\tau}_i = \mathbf{grad}_j\,\boldsymbol{\tau}_i^+ = \left(\delta_{i+1}^j - \delta_i^j\right)\mathbb{1}. \tag{3.28}$$

We get the diagonal and sub-diagonal elements of the NEB-Jacobian

$$\begin{aligned}
\mathbf{J}_{i,i-1}^{\mathrm{NEB}} &= -\,k\hat{\boldsymbol{\tau}}_i \otimes \hat{\boldsymbol{\tau}}_i^-, & (3.29)\\
\mathbf{J}_{i,i}^{\mathrm{NEB}} &= k\hat{\boldsymbol{\tau}}_i \otimes \left\{\hat{\boldsymbol{\tau}}_i^+ + \hat{\boldsymbol{\tau}}_i^-\right\} + \mathbf{H}_i - \hat{\boldsymbol{\tau}}_i\mathbf{H}_i\hat{\boldsymbol{\tau}}_i - \mathbf{A}, & (3.30)\\
\mathbf{J}_{i,i+1}^{\mathrm{NEB}} &= -\,k\hat{\boldsymbol{\tau}}_i \otimes \hat{\boldsymbol{\tau}}_i^+ + \mathbf{A}. & (3.31)
\end{aligned}$$

All other elements in the i^{th} row vanish.

Case: $V_{i+1} < V_i < V_{i-1}$

$\boldsymbol{\tau}_i = \boldsymbol{\tau}^- = \boldsymbol{R}_i - \boldsymbol{R}_{i-1}$. The vector gradient $\mathbf{grad}_j\,\boldsymbol{\tau}_i^-$ reads

$$\mathbf{grad}_j\,\boldsymbol{\tau}_i = \mathbf{grad}_j\,\boldsymbol{\tau}_i^- = \left(\delta_i^j - \delta_{i-1}^j\right)\mathbb{1}. \tag{3.32}$$

We get the diagonal and sub-diagonal elements of the NEB-Jacobian

$$\begin{aligned}
\mathbf{J}_{i,i-1}^{\mathrm{NEB}} &= -\,k\hat{\boldsymbol{\tau}}_i \otimes \hat{\boldsymbol{\tau}}_i^- - \mathbf{A}, & (3.33)\\
\mathbf{J}_{i,i}^{\mathrm{NEB}} &= k\hat{\boldsymbol{\tau}}_i \otimes \left\{\hat{\boldsymbol{\tau}}_i^+ + \hat{\boldsymbol{\tau}}_i^-\right\} + \mathbf{H}_i - \hat{\boldsymbol{\tau}}_i\mathbf{H}_i\hat{\boldsymbol{\tau}}_i + \mathbf{A}, & (3.34)\\
\mathbf{J}_{i,i+1}^{\mathrm{NEB}} &= -\,k\hat{\boldsymbol{\tau}}_i \otimes \hat{\boldsymbol{\tau}}_i^+. & (3.35)
\end{aligned}$$

All other elements in the i^{th} row vanish.

Other cases

These cover the situation of image i being a maximum or a minimum along the path. In this case $\boldsymbol{\tau}_i$ is a linear combination

$$\boldsymbol{\tau}_i = a\boldsymbol{\tau}^+ + b\boldsymbol{\tau}^- = a\boldsymbol{R}_{i+1} + (b-a)\boldsymbol{R}_i - b\boldsymbol{R}_{i-1} \tag{3.36}$$

The vector gradient $\mathbf{grad}_j\, \boldsymbol{\tau}_i$ reads

$$\begin{aligned}\mathbf{grad}_j\, \boldsymbol{\tau}_i = &\left(a\delta^j_{i+1} + (b-a)\delta^j_i - b\delta^j_{i-1}\right)\mathbb{1}\\ &+ \boldsymbol{\tau}_i^+ \otimes \mathbf{grad}(a) + \boldsymbol{\tau}_i^- \otimes \mathbf{grad}(b).\end{aligned} \tag{3.37}$$

Case: $a = |V_{i+1} - V_i|$, $b = |V_{i-1} - V_i|$

$$\begin{aligned}\mathbf{grad}(a) =&\frac{1}{2}\frac{1}{|V_{i+1} - V_i|}2(V_{i+1} - V_i)\cdot\left(\delta^j_{i+1}\nabla V_{i+1} - \delta^j_i\nabla V_i\right)\\ =&\mathrm{sign}(V_{i+1} - V_i)\left(\delta^j_{i+1}\nabla V_{i+1} - \delta^j_i\nabla V_i\right) && (3.38)\\ \mathbf{grad}(b) =&\mathrm{sign}(V_{i-1} - V_i)\left(\delta^j_{i-1}\nabla V_{i-1} - \delta^j_i\nabla V_i\right) && (3.39)\end{aligned}$$

Since the images i considered here are always minima or maxima $\mathrm{sign}_i = \mathrm{sign}(V_{i+1} - V_i) = \mathrm{sign}(V_{i-1} - V_i)$

$$\begin{aligned}\mathbf{grad}_j\, \boldsymbol{\tau}_i =&(a\delta^j_{i+1} + (b-a)\delta^j_i - b\delta^j_{i-1})\mathbb{1}\\ &+ \mathrm{sign}_i\cdot\left(\delta^j_{i+1}\boldsymbol{\tau}^+ \otimes \nabla V_{i+1}\right.\\ &\left.- \delta^j_i(\boldsymbol{\tau}^+ + \boldsymbol{\tau}^-)\otimes\nabla V_i + \delta^j_{i-1}\boldsymbol{\tau}^-\otimes\nabla V_{i-1}\right).\end{aligned} \tag{3.40}$$

The resulting elements of the Jacobian are:

$$\begin{aligned}\mathbf{J}^{\mathrm{NEB}}_{i,i-1} =& - k\hat{\boldsymbol{\tau}}_i \otimes \hat{\boldsymbol{\tau}}^- - \mathbf{A}\left\{b\mathbb{1} - \mathrm{sign}_i\cdot\boldsymbol{\tau}^-\otimes\nabla V_{i-1}\right\} && (3.41)\\ \mathbf{J}^{\mathrm{NEB}}_{i,i} =&k\hat{\boldsymbol{\tau}}_i \otimes \left\{\hat{\boldsymbol{\tau}}^+ + \hat{\boldsymbol{\tau}}^-\right\} + \mathbf{H}_i - \hat{\boldsymbol{\tau}}_i\mathbf{H}_i\hat{\boldsymbol{\tau}}_i + \mathbf{A}\left\{(b-a)\mathbb{1}\right.\\ &\left.-\mathrm{sign}_i\cdot(\boldsymbol{\tau}^+ + \boldsymbol{\tau}^-)\otimes\nabla V_i\right\} && (3.42)\\ \mathbf{J}^{\mathrm{NEB}}_{i,i+1} =& - k\hat{\boldsymbol{\tau}}_i \otimes \hat{\boldsymbol{\tau}}^+ + \mathbf{A}\left\{a\mathbb{1} + \mathrm{sign}_i\cdot\boldsymbol{\tau}^+\otimes\nabla V_{i+1}\right\}. && (3.43)\end{aligned}$$

Case: $a = |V_{i-1} - V_i|$, $b = |V_{i+1} - V_i|$

A similar calculations leads to:

$$\begin{aligned}\mathbf{J}^{\mathrm{NEB}}_{i,i-1} =& - k\hat{\boldsymbol{\tau}}_i \otimes \hat{\boldsymbol{\tau}}^- - \mathbf{A}\left\{b\mathbb{1} - \mathrm{sign}_i\cdot\boldsymbol{\tau}^+\otimes\nabla V_{i-1}\right\} && (3.44)\\ \mathbf{J}^{\mathrm{NEB}}_{i,i} =&k\hat{\boldsymbol{\tau}}_i \otimes \left\{\hat{\boldsymbol{\tau}}^+ + \hat{\boldsymbol{\tau}}^-\right\} + \mathbf{H}_i - \hat{\boldsymbol{\tau}}_i\mathbf{H}_i\hat{\boldsymbol{\tau}}_i + \mathbf{A}\left\{(b-a)\mathbb{1}\right.\\ &\left.-\mathrm{sign}_i\cdot(\boldsymbol{\tau}^+ + \boldsymbol{\tau}^-)\otimes\nabla V_i\right\} && (3.45)\\ \mathbf{J}^{\mathrm{NEB}}_{i,i+1} =& - k\hat{\boldsymbol{\tau}}_i \otimes \hat{\boldsymbol{\tau}}^+ + \mathbf{A}\left\{a\mathbb{1} + \mathrm{sign}_i\cdot\boldsymbol{\tau}^-\otimes\nabla V_{i+1}\right\} && (3.46)\end{aligned}$$

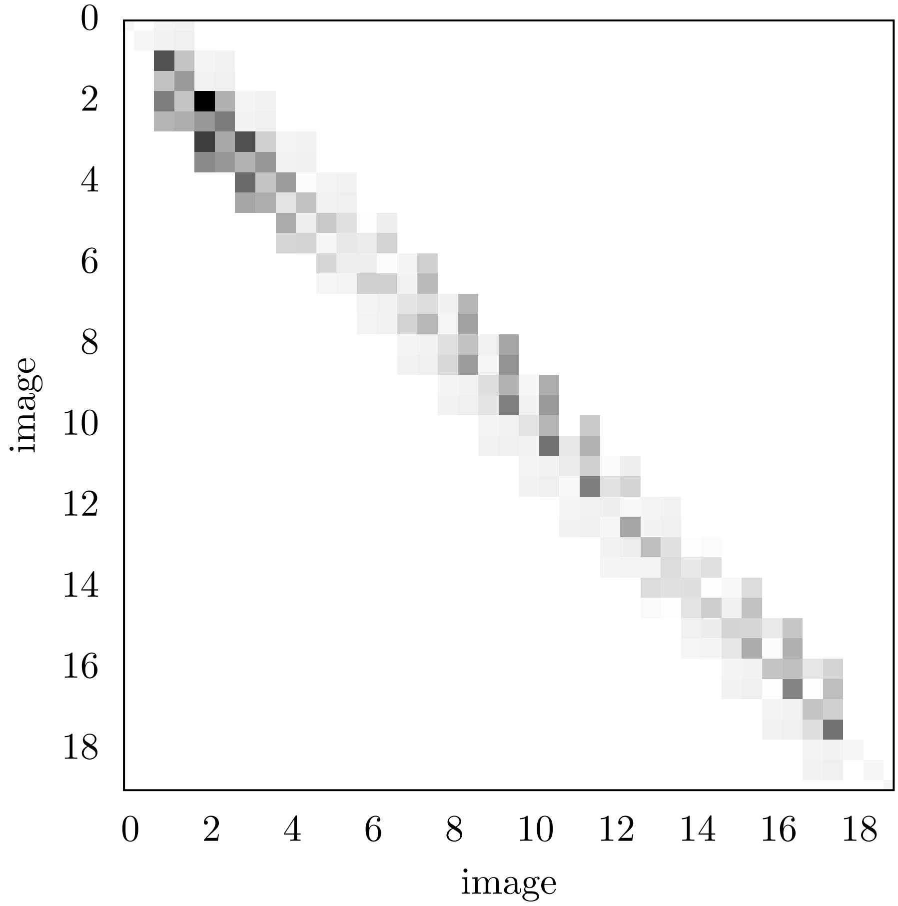

Figure 3.7: Visualization of the NEB Jacobian for the linear starting path in the MB potential. The darker a field is, the higher is the amount of the corresponding entry. White areas are zero. The Jacobian clearly shows asymmetry.

These expressions cover all cases so that the Jacobian, equation (3.14), can be set up and the Newton–Raphson method using equation (3.13) can be implemented.

In order to demonstrate the asymmetry as well as the band matrix character, the Jacobian of the starting path within the Müller–Brown potential is visualized in figure 3.7. The Müller–Brown potential and its use for the application of the NEB method described here will be covered in one of the next sections.

The first challenge to be faced is that the radius of convergence of the Newton–Raphson algorithm is, from experience, often rather small. By contrast, Newton–Raphson steps become large for a flat energy surface. Therefore the truncated Newton–Raphson approach was adopted. The Newton–Raphson step $d_{\text{Newton}} = |\mathbf{J}^{-1}\boldsymbol{F}|$ is scaled back if it extends the predefined maximal step length $d_{\max}$. This results in the iteration formula

$$\boldsymbol{R}_{n+1} = \begin{cases} \boldsymbol{R}_n - \mathbf{J}^{-1}\boldsymbol{F} & \text{if} \quad d_{\text{Newton}} \leq d_{\max} \\ \boldsymbol{R}_n - \mathbf{J}^{-1}\boldsymbol{F}\frac{d_{\max}}{d_{\text{Newton}}} & \text{if} \quad d_{\text{Newton}} > d_{\max} \end{cases} \tag{3.47}$$

The modified Newton–Raphson scheme for NEB optimisations presented here was implemented in a local branch of DL-FIND,[50] which is one of the optimiser options in ChemShell.[48] In the examples in the following section the method presented here is compared to the existing optimiser in DL-FIND, which was used in several applications.[51–56] There a quasi-Newton scheme is applied with the inverse Jacobian obtained from an L-BFGS update[57,58] of a scaled unitary matrix using the NEB force of the whole path. Details of this implementation are given elsewhere,[52] it is similar to an approach previously termed GL-BFGS.[59]

3.2.1.1 Global translation and rotation

For free (i.e., non-frozen) endpoints the NEB force is invariant with respect to translation and rotation of the whole path if the potential energy is invariant under these transformations (which is the case for molecules). Thus the Jacobian in Cartesian coordinates becomes singular. A step like in in equation (3.13) cannot be formed since $\mathbf{J}$ cannot be inverted. A singular value decomposition (SVD) of the form $\mathbf{U}^{\mathrm{T}}\mathbf{J}\mathbf{V} = \operatorname{diag}(\sigma_1,\ \sigma_2,\ \ldots,\ \sigma_{NM})$ of $\mathbf{J}$ will result in one or more singular values σ_i being zero.

Even if the endpoints are frozen, the first derivative of the NEB force is zero along the direction of a global translation of the non-frozen path as long as the frozen endpoints have a lower energy than their neighboring points. In this case, the upwind scheme, equation (2.54), causes the tangent vectors at the image next to the frozen endpoints to point towards the movable neighbor images. Specifically, if image 1 is frozen and the energy increases for the images 1, 2, and 3 in that order, then $\boldsymbol{\tau}_2 = \boldsymbol{\tau}_2^+ = \boldsymbol{R}_3 - \boldsymbol{R}_2$. The only term in the expression of the NEB force of image 2 which changes under a global translation of the path is $|\boldsymbol{\tau}_2^-|$, see equation (2.57). However, $\mathbf{grad}_2 |\boldsymbol{\tau}_2^-| = \hat{\boldsymbol{\tau}}_2^-$, see equation (3.21). Since the molecules of the start and end images (and thus all intermediate images) are superimposed to remove a translation between them, $\hat{\boldsymbol{\tau}}_2^-$ is orthogonal to a translation of $\boldsymbol{R}_2$ and the global NEB force vanishes. The same arguments hold for the other end of the NEB path. It should be noted that the NEB force is only invariant to a global translation of first order. The second derivative is non-zero and in fact the NEB force changes for non-zero displacements of the path. For a three-dimensional system three singular values are zero (two for a two-dimensional system). They correspond to translations. Those corresponding to rotations only approach zero for a converged NEB path with all forces approaching zero. For a system with one intermediate local minimum, the same arguments can be used to prove that translations of the two individual parts of the paths against each other also result in a first derivative of the NEB force of zero. Thus, in two dimensions, four singular values are zero for any general path, 6 for the converged path. In the system studied later three barriers with two minima between them in two dimensions, six singular values are zero for a general path, 13 for the converged one. Overall, a scheme is needed to deal with singular Jacobian matrices.

The inversion of the Jacobian matrix is replaced by a pseudo-inversion of the form

$$\mathbf{J}^{-1} \to \mathbf{J}^{+} = \mathbf{V}\,\mathrm{diag}\left(\frac{1}{\sigma_1}, \frac{1}{\sigma_2}, \frac{1}{\sigma_3}, \ldots, \frac{1}{\sigma_K}\right)\mathbf{U}^{\mathrm{T}}, \tag{3.48}$$

where $\mathbf{V}$ and $\mathbf{U}$ are the matrices of the right-singular and left-singular vectors and $\sigma_1 \ldots \sigma_K$ with $K \leq NM$ are all non-zero singular values. Since numerical noise affects the singular values, we ignore those with an absolute value smaller than a threshold.

The aim is to *minimize* the NEB force. The Newton–Raphson algorithm, however, converges to any stationary point, not necessarily to a minimum. Therefore the step direction for each pair of singular vectors is checked individually. In order for the step to point to a smaller NEB force, the scalar product of the right-side singular vector and the left-side singular vector to the same singular value should be positive. If it is negative, the step in the corresponding direction is reversed, i.e., the corresponding singular values are multiplied by -1. Practical application shows that this procedure ensures the convergence of the algorithm to the correct MEP.

3.2.1.2 Order of Convergence

A series $\{u_k\}$, $k = 1,\ 2,\ \ldots$ converges with the order p to its limit u_∞ if

$$\lim_{k\to\infty} = \frac{|u_{k+1} - u_\infty|}{|u_k - u_\infty|^p} = c \text{ with } c > 0, \tag{3.49}$$

While this is a formal definition, it is less useful for numerical purposes. It is therefore more common to define a series $\varepsilon_k > 0$ which converges to zero and fulfills condition 3.49. Thereupon a numerical series can be said to converge with the order p if[60]

$$|u_k - u_\infty| \leq \varepsilon_k \tag{3.50}$$

An example of a quadratically ($p = 2$) convergent series is

$$\varepsilon_k = 10^{-2^k} \tag{3.51}$$

Colloquially it is often said that a series converges quadratically if the number of correct decimal figures doubles with each iteration. However, this is a sufficient, but not a necessary condition.

3.2.1.3 Application: Müller–Brown Potential

The method is applied to the two-dimensional Müller–Brown (MB) potential.[61] A straight line between the two main minima is used as initial guess, see figure 3.8. 19 images approximate the path. The first and last image are fixed to the minima. This system is not invariant with respect to translation and rotation, since the potential energy changes in each of the two dimensions. Therefore a direct inversion of the Jacobian is used here rather than the pseudo inversion via the SVD.

The convergence properties of the method are given in 3.2 and compared to the L-BFGS optimizer in 3.9. Beginning from iteration 7 quadratic convergence is archived. To demonstrate the convergence rate numerically the remaining $|\boldsymbol{F}^{\mathrm{NEB}}|$

is compared to a series which is known to converge quadratically. Sets of parameters other than those used here ($k = 2.93$, $d_{\max} = 0.15$) also lead to quadratic convergence, which may, however, set in only after more cycles.

Table 3.2 also attempts to quantify how asymmetric the Jacobian actually is. For that purpose, the Euclidean norm of the Jacobian $||\boldsymbol{J}^{\mathrm{NEB}}||$ is compared to $||\boldsymbol{J}^{\mathrm{NEB}} - (\boldsymbol{J}^{\mathrm{NEB}})^{\mathrm{T}}||$. For a symmetric Jacobian, the latter should be zero. It is clear that the Jacobian significantly deviates from a symmetric matrix. This is one reason why the L-BFGS approach, which results in a symmetric approximative Jacobian matrix, converges slowly compared to the approach shown in this work.

In cases where the step is scaled back according to equation (3.47), the scaling factor $d_{\max}/d$ is given in table 3.2. Scaling is only necessary before the region of quadratic convergence is entered.

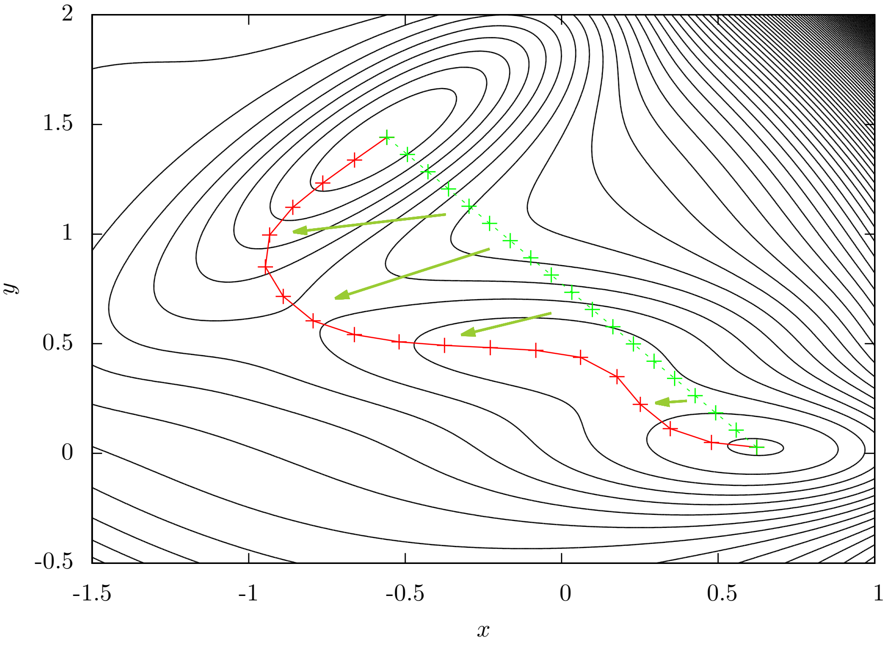

Figure 3.8: Contour plot of the MB potential. The green dashed line shows the initial guess of the NEB path. The red solid line shows the converged MEP. Images used to approximate the path are marked by crosses.

The results clearly show that the optimisation algorithm presented in this work efficiently finds the region of convergence of the Newton–Raphson method where it adopts quadratic convergence. This two-dimensional example does not include translational or rotational invariance, however. The resulting Jacobian can be inverted. A more stringent test for molecular systems is presented in the following example.

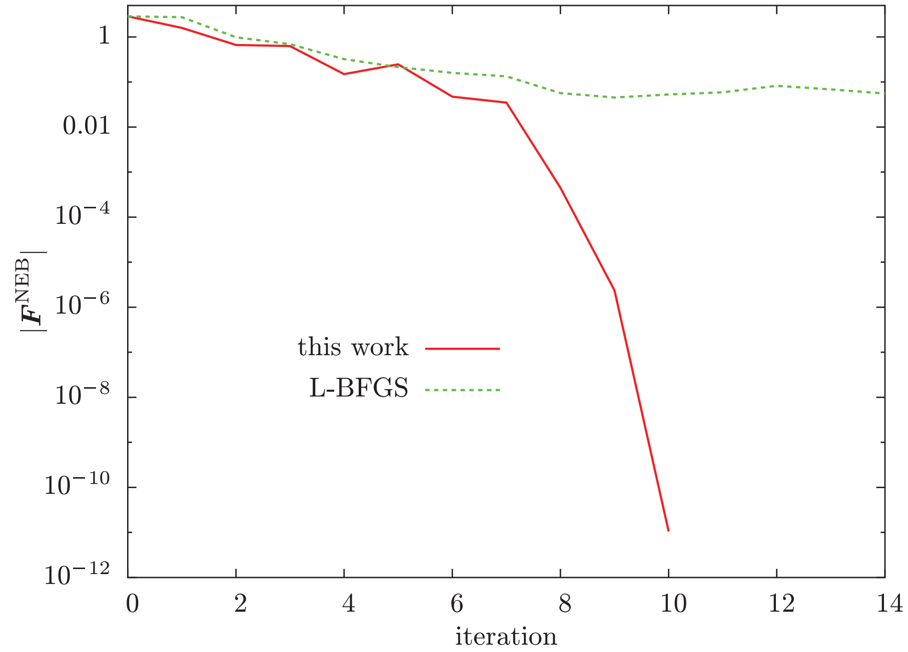

Figure 3.9: Convergence of an NEB optimisation in the MB potential with 19 images using the algorithm presented in this work (red solid line) compared with the L-BFGS optimiser (green dashed line).

iteration	$\|\boldsymbol{F}^{\mathrm{NEB}}\|$	$\frac{\varepsilon_0}{10^{2^k}}$	d_{max}/d	$\|\|\boldsymbol{J}^{\mathrm{NEB}}\|\|$	$\|\|\boldsymbol{J}^{\mathrm{NEB}} - (\boldsymbol{J}^{\mathrm{NEB}})^{\mathrm{T}}\|\|$
0	2.85952		0.39	55.7	48.1
1	1.59505		0.81	53.2	30.8
2	0.66294		0.22	49.9	23.6
3	0.630337		0.93	49.9	21.9
4	0.149348		0.85	51.7	23.2
5	0.247031			53.7	24.4
6	0.047369			54.5	23.6
7	0.0349786	10^{-1}		55.3	23.9
8	0.0**00**450947	10^{-2}		55.3	23.7
9	0.0**0000**235723	10^{-4}		55.3	23.7
10	0.0**000000000**105215	10^{-8}			

Table 3.2: Convergence of an NEB optimisation in the MB potential. The third column shows a suitable series to demonstrate quadratic convergence. Doubling correct digits in bold. The Euclidean norm of the Jacobian and its asymmetric components in the fifes and sixth columns aim to demonstrate the magnitude of the asymmetry.

3.2.1.4 Application: Rearrangement of a Two-Dimensional Lenard–Jones Cluster

As a second example the method is applied to the rearrangement of a planar Lennard–Jones cluster of seven particles. The pair interaction is defined by

$$V(r) = 4\varepsilon \left[\left(\frac{\sigma}{r}\right)^{12} - \left(\frac{\sigma}{r}\right)^{6} \right], \tag{3.52}$$

where r is the distance between two particles. The parameters ε and σ denote the depth and position of the minimum respectively.

The example was taken from reference 31. The minima along the path are illustrated in figure 3.10. A linear interpolation between these minima is used as the initial path. Movement of all atoms is restricted to a two-dimensional plane. This results in 14 degrees of freedom per image including one for rotation and two for translation. Again 19 images are used to resolve the path unless noted otherwise and the first and last images are frozen. The spring constant is set to $k = 15$ and the step limitation to $d_{\max} = 0.04$. All quantities for this example are given in Lennard–Jones units (ε and σ). The images of the initial path are superimposed to minimize rotational and translational displacement. This had been shown previously to be important in NEB optimisations.[46]

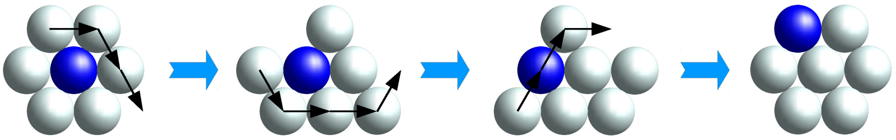

Figure 3.10: Rearrangement of a planar Lennard–Jones cluster with seven atoms. The configurations show the minima which are passed along the path.

In figure 3.11 the convergence properties for this system of the optimisation method presented here is compared to the L-BFGS algorithm. The resulting numbers are given in table 3.3. From iteration 7 onwards we obtain quadratic convergence as shown by comparison to a quadratically converging series.

The method converges for a wide range of parameters (k, $d_{\max}$), although the number of steps needed to arrive in the basin for quadratic convergance differs. Using more images to discretize the path shows a difference from the previous example. Here, translations and rotations leave the potential energy unchanged. These additional degrees of freedom transform the intrinsic minima from points to three-dimensional hyperplanes in configurational space. The system can minimize

iteration	$\lvert \boldsymbol{F}^{\mathrm{NEB}} \rvert$	$\frac{\varepsilon_0}{10^{2^k}}$	$d_{\max}/d$	$\lvert\lvert \boldsymbol{J}^{\mathrm{NEB}} \rvert\rvert$	$\lvert\lvert \boldsymbol{J}^{\mathrm{NEB}} - (\boldsymbol{J}^{\mathrm{NEB}})^{\mathrm{T}} \rvert\rvert$
0	3.21598		0.49	318.5	57.3
1	1.8302			273.3	41.3
2	0.352492		0.45	226.8	28.5
3	0.202129			221.5	27.0
4	0.0202993			218.6	26.8
5	0.0318344			217.6	26.5
6	0.00687046			218.4	26.7
7	0.000448025			218.5	26.7
8	0.000**0**244796	10^{-4}		218.5	26.7
9	0.000**00**335986	10^{-5}		218.5	26.7
10	0.000**00000**250889	10^{-7}		218.5	26.7
11	0.000**00000000000**923465	10^{-11}			

Table 3.3: Convergence of an NEB optimisation for the Lennard–Jones cluster rearrangement with 19 images.

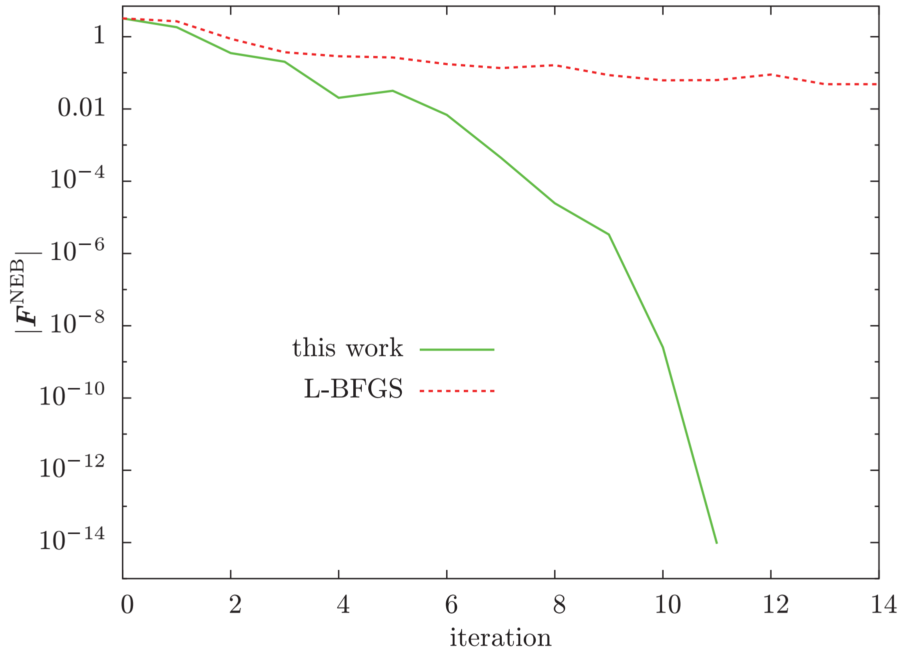

Figure 3.11: Convergence of an NEB optimisation for the Lennard–Jones cluster with 19 images using the algorithm presented in this work (green solid line) compared with the L-BFGS optimizer (red dashed line).

the NEB force by gathering images at a minimum, displaced by translation and/or rotation. While there should not be any force which displaces images along the translational and rotational modes, numerical errors in the force or in the initial coordinates can build up due to incomplete projection. To improve the stability remaining translational components are also removed from each Newton–Raphson step before performing it. In figure 3.12 the energy profile along the NEB path after an NEB optimisation with 49 images is shown. Obviously, fewer images are gathered at the minima when the translational component is projected out. In figure 3.13 the norm of the total NEB force of all images with altered and unaltered steps is compared. Quadratic convergence is reached in both cases, but much earlier if translations are removed. Further improvements could be possible by removing rotational components from the steps as well.

This work presents calculations for a two-dimensional cluster because it is easier to visualize and to interpret than a real three-dimensional system. However, no further challenges are expected for three-dimensional chemical applications.

It should be noted that the invariance of the potential with translation and rotation does not cause problems in the L-BFGS approach. BFGS results in a positive definite Hessian even if the exact one would be positive semidefinite. Translations and rotations are simply ignored in the L-BFGS approach without altering the convergence properties.

3.3 NEB Optimisations in the Free Energy Landscape [‡]

In the previous sections we have seen that NEB can be used to find an MEP by minimising the NEB force. Here the free-energy gradients of equation (3.2) are used and the free-energy Hessian is reassembled as

$$\tilde{\mathbf{H}} = \sum_{i \notin \{i_1 \ldots i_6\}} \hat{\boldsymbol{v}}_i \hat{\boldsymbol{v}}_i^{\mathrm{T}} \lambda_i \tag{3.53}$$

where $\hat{\boldsymbol{v}}_i$ are the eigenvectors and λ_i are the eigenvalues of the Hessian gained by umbrella integration according to equation (2.52). The omitted indices are those with the largest overlap with rotational and translational modes equal to

---

[‡] Parts of this chapter were published in reference 62: M. U. Bohner, J. Zeman, J. Smiatek, A. Arnold, and J. Kästner: "Nudged-elastic band used to find reaction coordinates based on the free energy", *J. Chem. Phys.* **140**, 074109 (2014).

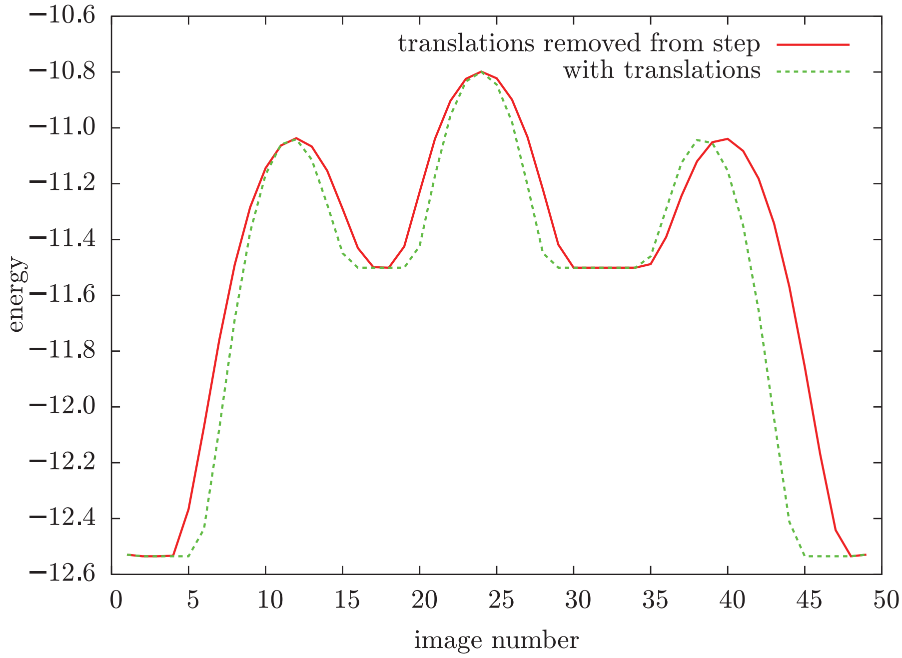

Figure 3.12: Energy profiles of the NEB paths of the planar Lennard–Jones system with translations removed from each optimisation step (red solid line) and unaltered steps (green dashed).

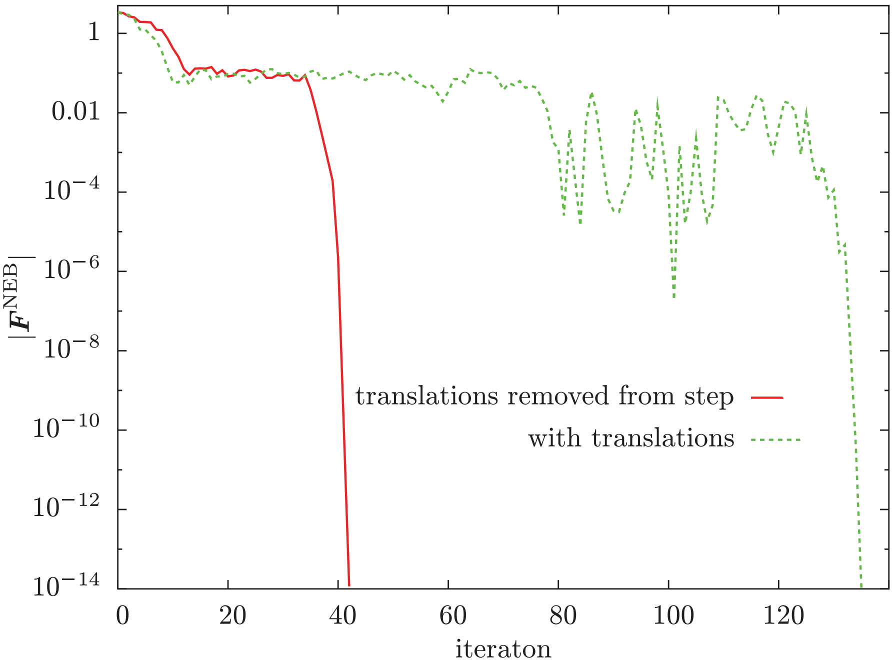

Figure 3.13: Comparison of the convergence with translations removed from each step (red solid line) and unaltered steps (green dashed) for the NEB optimisation for the Lennard–Jones cluster with 49 images.

the proceeder leading to equation (3.3). While gradient and Hessian are easily available by umbrella integration, the actual underlying potential is not accessible like the directly free-energy differences between adjacent points on the NEB path. Such an energy difference is required in the original version of NEB for defining the tangent vector. In the upwind scheme, the tangent vector of each image i points to the neighbouring image with the higher energy. This work relies on a quadratic approximation of the free-energy surface around the coordinates $\boldsymbol{R}_i$ of each image:

$$\Delta A_i = \tilde{\boldsymbol{g}}_i \boldsymbol{\tau}_i^+ + \frac{1}{2}\left(\boldsymbol{\tau}_i^+\right)^{\mathrm{T}} \tilde{\mathbf{H}} \boldsymbol{\tau}_i^+ \tag{3.54}$$

$$\tag{3.55}$$

This results in the definition of the tangent vector $\boldsymbol{\tau}_i$:

$$\boldsymbol{\tau}_i = \begin{cases} \boldsymbol{\tau}_i^+ = \boldsymbol{R}_{i+1} - \boldsymbol{R}_i & \text{if} \quad \Delta A_i > 0 > -\Delta A_{i-1} \\ \boldsymbol{\tau}_i^- = \boldsymbol{R}_i - \boldsymbol{R}_{i-1} & \text{if} \quad \Delta A_i < 0 < -\Delta A_{i-1} \end{cases}, \tag{3.56}$$

if the free-energy change is monotonous and

$$\boldsymbol{\tau}_i = \begin{cases} \Delta A_i^{\max} \boldsymbol{\tau}_i^+ + \Delta A_i^{\min} \boldsymbol{\tau}_i^- & \text{if} \quad \Delta A_i > -\Delta A_{i-1} \\ \Delta A_i^{\min} \boldsymbol{\tau}_i^+ + \Delta A_i^{\max} \boldsymbol{\tau}_i^- & \text{if} \quad \Delta A_i^+ < -\Delta A_{i-1} \end{cases} \tag{3.57}$$

with

$$\begin{aligned} \Delta A_i^{\max} &= \max\left(|\Delta A_i|, |\Delta A_{i-1}|\right) \\ \Delta A_i^{\min} &= \min\left(|\Delta A_i|, |\Delta A_{i-1}|\right). \end{aligned} \tag{3.58}$$

if image i is a minimum or a maximum along the path.

The reduced gradient, equation (3.2) and Hessian, equation (3.53), enter the formula for the improved tangent NEB force, equation (2.57), and its Jacobian, equation (3.26), previously derived.

For M images along the NEB path the Jacobian $\mathbf{J}$ for the whole NEB force is a non-symmetric $3SM \times 3SM$-matrix. It again contains 6 components corresponding to translation and rotation. Thus it is singular and cannot be directly inverted to form a Newton–Raphson step of the form $\boldsymbol{R}_{n+1} = \boldsymbol{R}_n - \mathbf{J}_n^{-1} \boldsymbol{F}^{\mathrm{NEB}}(\boldsymbol{R}_n)$. The inverse is replaced by a pseudo-inverse $\mathbf{J}^+$ and some components of steps direction inverted equal to the proceeder explained in section 3.2.1.1.

3.3.1 Levenberg–Marquardt minimization of the NEB force

The NEB force is minimized using the Levenberg–Marquardt[63] algorithm. It is related to a truncated Newton–Raphson approach. While in the latter the step is simply scaled back as soon it exceeds a trust-radius $d_{\max}$, Levenberg–Marquardt adopts a more flexible approach. The Newton–Raphson step

$$\boldsymbol{R}_{n+1} = \boldsymbol{R}_n - \mathbf{J}_n^{+} \boldsymbol{F}^{\mathrm{NEB}}(\boldsymbol{R}_n), \tag{3.59}$$

is replaced by

$$\boldsymbol{R}_{n+1} = \boldsymbol{R}_n - \left(\mathbf{J}_n + \lambda \mathbb{1}\right)^{-1} \boldsymbol{F}^{\mathrm{NEB}}(\boldsymbol{R}_n), \tag{3.60}$$

if the Newton–Raphson step is larger than $d_{\max}$. The scalar parameter λ is chosen such that the step length equals $d_{\max}$. $\mathbb{1}$ denotes the identity matrix.

This algorithm can be seen both as a damped Newton–Raphson method or a mixture of steepest descent and Newton–Raphson. The larger λ is, the more steepest descent character the step includes. If the Jacobian $\mathbf{J}$ has eigenvalues with a negative real part, more than one value for λ can be found to result in a step size of $d_{\max}$. In these cases we always chose the largest λ to ensure the step to point into the direction of the NEB force. Note that the choice of λ to damp the Newton–Raphson step to the desired length also ensures that $(\mathbf{J}_n + \lambda \mathbb{1})$ is non-singular and can be directly inverted.

In summary, the NEB optimisation algorithm works as follows:

1. Calculate free-energy gradients and Hessians of each NEB image by umbrella integration.
2. Calculate the NEB-Jacobian $\mathbf{J}$ from image data using the equations given in reference 64.
3. Calculate the Newton–Raphson step $\boldsymbol{\delta}_{\mathrm{NR}}$ by use of the pseudo-inverse, $\mathbf{J}^{+}$.
4. Calculate the Newton–Raphson step length $d_{\mathrm{NR}} = |\boldsymbol{\delta}_{\mathrm{NR}}|$.
5. If $d_{\mathrm{NR}} \leq d_{\max}$ use Newton–Raphson step $\boldsymbol{\delta} = \boldsymbol{\delta}_{\mathrm{NR}}$
   Else:
   a) Optimise λ so that
      $d_{\max} = \left|\left(\mathbf{J} + \lambda \mathbb{1}\right)^{-1} \boldsymbol{F}^{\mathrm{NEB}}(\boldsymbol{R})\right|$.

b) Calculate the step
   $\boldsymbol{\delta} = -\left(\mathbf{J} + \lambda \mathbb{1}\right)^{-1} \boldsymbol{F}^{\mathrm{NEB}}(\boldsymbol{R})$.

6. Apply the step $\boldsymbol{\delta}$ and go to next iteration

Optimisation of λ

Usually the Levenberg–Marquardt algorithm is used to find minima of a potential function. For these classes of problems the algorithm uses the Hessian like the Newton–Raphson scheme in equation (3.1). The λ optimisation problem then reads

$$|\underbrace{(\mathbf{H} + \lambda \mathbb{1})}_{\mathcal{H}_{\mathrm{LM}}}{}^{-1}\boldsymbol{g}| = d_{\max}. \tag{3.61}$$

In the following I call the underbraced term $\mathcal{H}_{\mathrm{LM}}$. Its eigenvalues $\mu_{\mathrm{LM},i}$ can be calculated as follows

$$\begin{aligned} 0 \overset{!}{=} &\det|\mathcal{H}_{\mathrm{LM}} - \mu_{\mathrm{LM}}\mathbb{1}| = \det|\mathbf{H} - \underbrace{\{\mu_{\mathrm{LM}} - \lambda\}}_{=\mu}\mathbb{1}| \\ \Rightarrow &\mu_{\mathrm{LM},i} = \mu_i + \lambda, \end{aligned} \tag{3.62}$$

where μ_i are the eigenvalues of the Hessian $\mathbf{H}$. The right eigenvectors are the same for $\mathcal{H}_{\mathrm{LM}}$ and $\mathbf{H}$.

$$\begin{aligned} \mathcal{H}_{\mathrm{LM}}\hat{\nu}_i = &(\mathbf{H} + \lambda \mathbb{1})\hat{\nu}_i = \mu_i\hat{\nu}_i + \lambda\hat{\nu}_i = \mu_{\mathrm{LM},i}\hat{\nu}_i \\ \Rightarrow \; &\hat{\nu}_{\mathrm{LM},i} = \hat{\nu}_i. \end{aligned} \tag{3.63}$$

The force term $\boldsymbol{g}$ can be decomposed into the basis of the eigenvectors by solving the linear system of equations

$$\boldsymbol{g} = (\hat{\nu}_{\mathrm{LM}})\boldsymbol{x} \;\Rightarrow\; \boldsymbol{g} = \sum_j \hat{\nu}_{\mathrm{LM},j} x_j \tag{3.64}$$

where $(\hat{\nu}_{\mathrm{LM}})$ denotes the matrix of eigenvectors. Since a Hessian of a potential function is symmetric, the eigenvectors form an orthogonal system. The coefficients $\boldsymbol{x}$ can be calculated more efficiently by

$$\boldsymbol{x} = (\hat{\nu}_{\mathrm{LM}})^{\mathrm{A}}\boldsymbol{g} \tag{3.65}$$

because a matrix of orthogonal columns is unitary. The suffix A denotes the conjugated transposed matrix. Obviously:

$$\begin{aligned}\mathcal{H}_{\mathrm{LM}}^{-1}\boldsymbol{g} =& \sum_i \frac{1}{\mu_{\mathrm{LM},i}}\hat{\nu}_{\mathrm{LM},i}\hat{\nu}_{\mathrm{LM},i}^{\mathrm{T}}\sum_j \hat{\nu}_{\mathrm{LM},j}x_j \\ =& \sum_i \frac{x_i}{\mu_{\mathrm{LM},i}}\hat{\nu}_{\mathrm{LM},i}\end{aligned} \tag{3.66}$$

and

$$\left|\mathcal{H}_{\mathrm{LM}}^{-1}\boldsymbol{g}\right|^2 = \sum_i \frac{|x_i|^2}{|\mu_{\mathrm{LM},i}|^2}. \tag{3.67}$$

The derivative of (3.67) with respect to λ can be calculated analytically, and the problem of optimising λ can be efficiently solved by a Hebden method.[65] To the best of the authors knowledge this is the proceeder which is used in most implementations of the Levenberg–Marquardt algorithm.

Unfortunately, the problem of NEB optimisations does not deal with a symmetric Hessian but with a non-symmetric Jacobian. Steps leading to equations (3.66) and (3.67) are only valid if the eigenvectors form an orthonormal basis. In this work the author does not know how else to proceed and applies a brute force approach, calculating the step length for each optimisation step by a matrix inversion.

From equation (3.67) one can easily see that for $\mu_{\mathrm{LM},i} \approx 0$ and $\lambda \approx -\mu_i$ respectively the step length becomes very large, like its deviation. This is in principle also true for a non-symmetric Jacobian even if the eigenvalues can be complex. Several tries with different methods showed that a simple bisectional algorithm has a good speed of convergency for this application. A Bisectional algorithm shows much better convergency than e. g. a pseudo Newton–Raphson algorithm. A pseudo Hebden-method was not tested.

3.3.2 Application: Alanine Dipeptide

As a test case the well studied alanine dipeptide system in vacuum was chosen. The five backbone atoms were assigned to the RCS as illustrated in figure 3.3. For backbone torsion angles the three minima named C_5, $\mathrm{C}_7^{\mathrm{eq}}$ and $\mathrm{C}_7^{\mathrm{ax}}$ are known. As an initial guess for the transition path a linear interpolation in terms of torsion angles between two minima is used. The paths between C_5 and $\mathrm{C}_7^{\mathrm{eq}}$ and $\mathrm{C}_7^{\mathrm{ax}}$ are approximated by 16 images each. The NEB spring constant is set to at

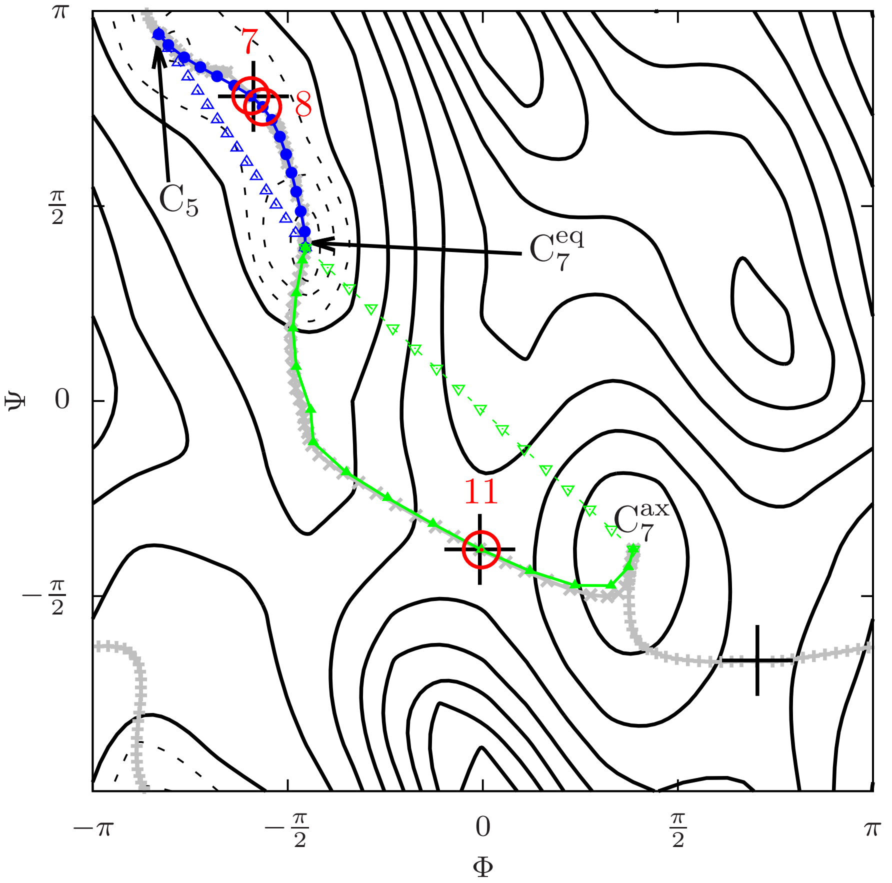

Figure 3.14: Starting paths (dashed lines) and converged free-energy NEB paths (solid lines) projected into the space of torsion angles Ψ and Φ of the alanine dipeptide. The contour lines show the potential energy with all degrees of freedom but Ψ and Φ relaxed. The minimum at C_7^{eq} is at 0 kJ mol^{-1}. Dotted lines are contours at 2.5, 5.0, and 7.5 kJ mol^{-1}. Solid lines are contours from 10 kJ mol^{-1} in steps of 10 kJ mol^{-1}. Gray lines show the MFEP and crosses the saddle points obtained with the serial algorithm. Red circles mark the images used as estimates for the saddle points. The indices of these images are printed as red numbers.

0.025 atomic units $\approx 2.3 \times 10^4$ kJ mol^{-1} nm^{-2} and the maximal step length at $d_{\mathrm{max}} = 0.025$ nm. While the precise number of steps to reach convergence obviously depends on the choice of these parameters, convergence was found for a wide range of values, sometimes with fewer steps than reported with the values given here. The author assumes that these values are also in a sensible range for other, bigger systems. A much smaller spring force leads to an uneven distribution of the images, larger spring forces reduce the radius of convergence. Similarly, a larger trust radius may in some cases speed up convergence, but increases the danger of complete divergence as well. Overall there is not much need to search for an optimal parameter set.

The actual molecular dynamic simulations were done using the software GROMACS[66] version 4.6.2. Unfortunately the author does not know how to use Cartesian coordinates as reaction coordinates in GROMACS. The position restraints algorithm in GROMACS should in principle serve for this issue. However, the author was not able to produce reasonable results this way. The GROMACS code was therefore patched with PLUMED[67] version 1.3, a code which adds a powerful capacity to freely define reaction coordinates to various MD packages. With PLUMED it is not only possible to restrain the reaction coordinate to the value of a reference structure, but also to an arbitrary value. This is an important feature of PLUMED for any method which searches an unknown point in the RCS.

As force field CHARMM22[8] a temperature of 300 K and a time step of 1 fs is used. The umbrella sampling uses the velocity Verlet integrator, a Nose–Hoover chain[11–14] thermostat with a chain length of 4 and a response time of 200 fs. The bias for umbrella sampling is $K = 0.2$ atomic units ($\approx 1.9 \times 10^5$ kJ mol^{-1} nm^{-2}). Independent MD runs have to be performed for each image in each step of the NEB optimisation. The accuracy obtained in the gradient and Hessian is obviously increased by longer sampling. While more noise can be tolerated at the beginning of an optimisation, more accurate values are required close to convergence. Therefore the number of steps to be sampled are increased by the heuristic criterion $N_{\mathrm{STEP}} = \max(10^6, 10^{10}/(\mathrm{RMS}(\boldsymbol{F}^{\mathrm{NEB}}))^2)$ with $\boldsymbol{F}^{\mathrm{NEB}}$ being the NEB force of the previous step in kJ mol^{-1} nm^{-1} and RMS denoting the root of the mean square. From the resulting trajectories the first 0.1 ps is omitted and every tenth step is used for the analysis. Each path is converged until $\mathrm{RMS}(\boldsymbol{F}^{\mathrm{NEB}})$ undercuts 10 kJ mol^{-1} nm^{-1}.

Describing the reaction with five backbone atoms in the RCS one obtains a path in 15 dimensions (six of those belonging to translation and rotation, however). Since this cannot be illustrated directly, we use a projection on to the two dimensional space of the backbone torsion angles shown in figure 3.3. In figure 3.14 the projection of the initial guess and the converged paths are shown in a contour map of the potential energy. The results gained by the serial method,[36] using the same RCS but with the saddle points found by Newton–Raphson search, are shown in gray.

The saddle points (transition states) are the points with highest free energy along the path. Using umbrella integration, there is no direct access to the free energy along the path. However, the gradient of the free energy at each image is known. A projection of the gradient on to the tangent of the path $\boldsymbol{g}_i \cdot \boldsymbol{\tau}_i$ allows an approximation of the free energy via integration. The points where $\boldsymbol{g}_i \cdot \boldsymbol{\tau}_i$ is zero are stationary points. Images close to these are used as approximations to the saddle point and can be used as an initial guess for a Newton–Raphson refinement.

In the following, convergence properties of specific paths are discussed.

Transition between C_5 and $\mathrm{C}_7^{\mathrm{eq}}$

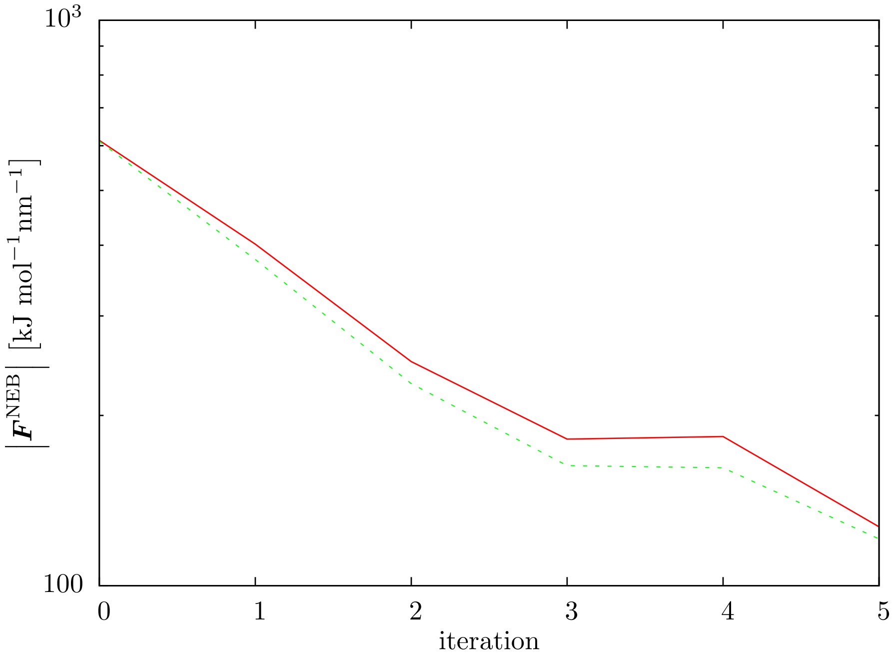

Figure 3.15: Convergence of the NEB force of a path between the minima C_5 and $\mathrm{C}_7^{\mathrm{eq}}$ using 16 images and a linear interpolation in terms of the backbone torsion angles as starting guess. The red solid, red line corresponds to the total NEB force, the green dashed line to the component of the force perpendicular to the path (ignoring uneven distribution of the images).

iteration	$\lvert\delta\rvert$	$\lvert\delta_{\mathrm{NR}}\rvert$	λ
0	0.0250	0.6921	18,132
1	0.0250	0.1608	5,203
2	0.0250	0.0811	2,668
3	0.0250	0.0272	2,406
4	0.0124	0.0124	0
5	0.0184	0.0184	0

Table 3.4: Levenberg–Marquardt parameters for the NEB optimisation of the path between C_5 and C_7^{eq}. The step lengths $|\delta|$ and $|\delta_{\mathrm{NR}}|$ are given in nm, the shift parameter λ in kJ mol^{-1} nm^{-2}.

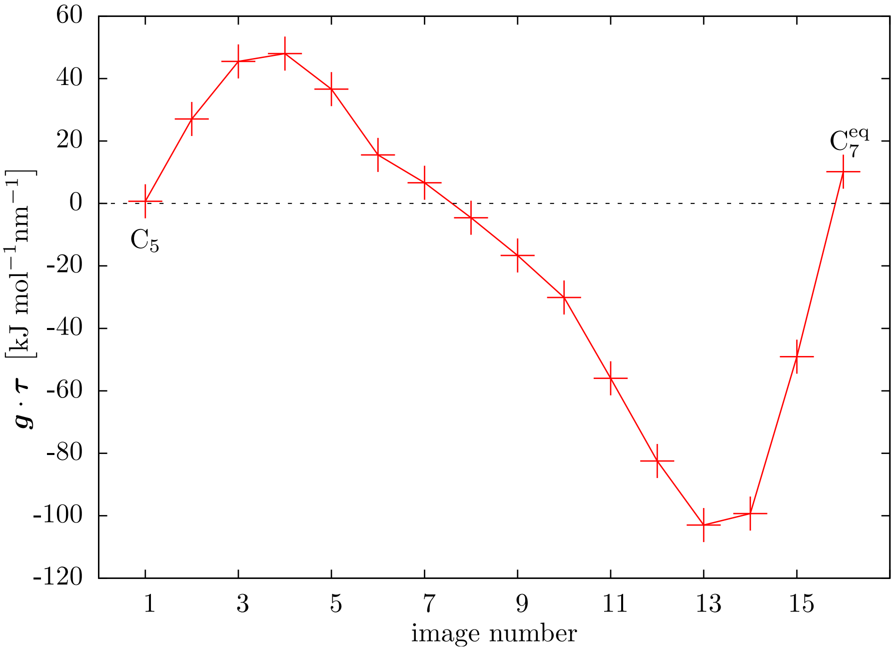

Figure 3.16: Gradient profile of the path between the minima C_5 and C_7^{eq} after convergence. The diagram shows free energy gradient projected on to the tangent vector $\hat{\boldsymbol{\tau}}_i$ of each image. Images number 7 and 8 are good estimates for saddle point.

The convergence of the NEB force for the path of the transition between C_5 and C_7^{eq} is shown in figure 3.15. The convergence criterion for the NEB optimisation ($\text{RMS}(\boldsymbol{F}^{\text{NEB}}) < 10$ kJ mol^{-1} nm^{-1}) is already reached after six NEB search steps. The first four of these are Levenberg–Marquardt steps with a non-zero λ, see table 3.4, the last two are pure Newton–Raphson steps. Figure 3.16 shows the projection of the gradient of each image on to the tangent vector for the converged path. Images 7 and 8 are the best approximations for the saddle point. This saddle point lies in a flat but rough area of the free-energy surface. Therefore the following Newton–Raphson search converges only with difficulty. A saddle where found point at $\Phi = -104.4°$, $\Psi = 139.2°$ which is in good agreement with the values from the literature[36] $\Phi = -105.8°$, $\Psi = 140.7°$. However, already before the Newton–Raphson search, image 7 of the converged NEB path has an RMS of the gradient of 5.5 kJ mol^{-1} nm^{-1}, which is already below the convergence criterion of 10 kJ mol^{-1} nm^{-1} previously used in the serial algorithm. Image 8 needs one Newton–Raphson step to reach an RMS of the gradient of 2.2 kJ mol^{-1} nm^{-1}, which is also below the convergence threshold.

Transition between C_7^{eq} and C_7^{ax}

The convergence of the NEB force for this transition is shown in figure 3.17. This optimisation is somewhat more challenging than the path discussed previously. In 14 steps the Newton–Raphson step size is longer than $d_{\text{max}} = 0.025$ nm so that the Levenberg–Marquardt algorithm reduces the step size, see table 3.5. It is only towards the convergence, from step 14 onwards, that a pure Newton–Raphson step is used. Convergence is smooth and the threshold is reached after 20 steps. Figure 3.18 displays the projection of the gradient of each image on to the tangent vector for the converged path. Image 11 is the best approximation for the saddle point. In figure 3.3 it appears that this would already perfectly coincide with the saddle point found previously.[36] However, the projection on to only two degrees of freedom hides details. 4 further Newton–Raphson steps with $d_{\text{max}} = 0.001$ nm were performed to refine this transition state to the one known from the literature[36] at $\Phi = -1.4°$ and $\Psi = -68.4°$, see figure 3.19.

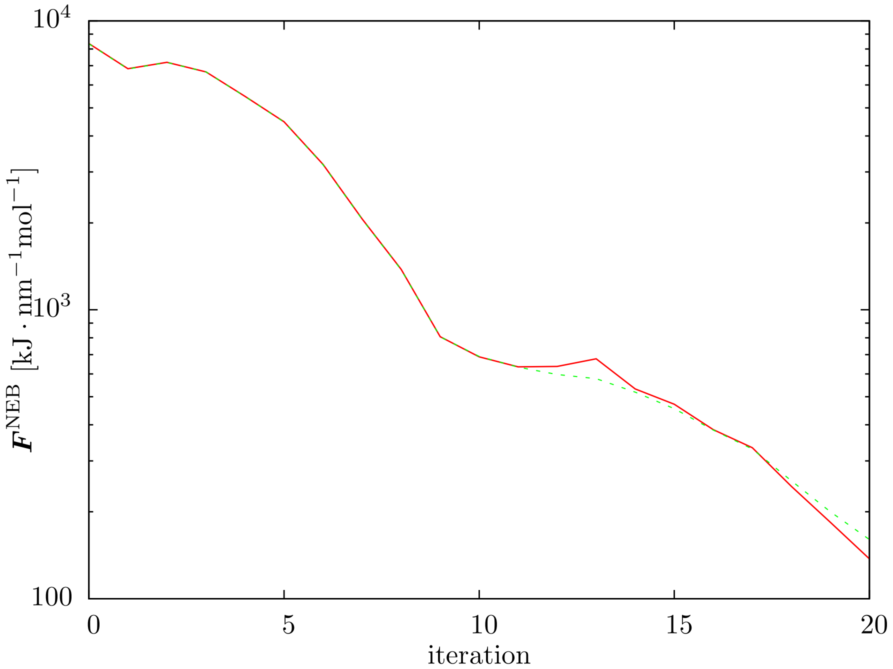

Figure 3.17: Convergence of an NEB path between the minima $\mathrm{C}_7^{\mathrm{eq}}$ and $\mathrm{C}_7^{\mathrm{ax}}$ using 16 images and a linear interpolation in terms of the backbone torsion angles as starting guess. The solid red line corresponds to the total NEB force, the dashed green line to the component of the force perpendicular to the path.

iteration	$\vert\delta\vert$	$\vert\delta_{\mathrm{NR}}\vert$	λ
0	0.0250	1.3012	211,692
1	0.0250	1.1858	216,716
2	0.0250	0.4166	156,690
3	0.0250	0.0928	109,847
4	0.0250	0.1203	71,291
5	0.0250	0.0694	39,171
6	0.0250	0.0394	17,596
7	0.0250	0.6282	14,741
8	0.0250	0.0547	12,917
9	0.0250	0.0683	14,041
10	0.0250	0.1693	13,805
11	0.0250	0.1387	10,668
12	0.0250	0.0470	7,359
13	0.0250	0.0397	3,414
14	0.0109	0.0109	0
15	0.0065	0.0065	0
16	0.0088	0.0088	0
17	0.0047	0.0047	0
18	0.0102	0.0102	0
19	0.0072	0.0072	0

Table 3.5: Levenberg–Marquardt parameters for the NEB optimisation of the path between $\mathrm{C}_7^{\mathrm{eq}}$ and $\mathrm{C}_7^{\mathrm{ax}}$. The step lengths $|\delta|$ and $|\delta_{\mathrm{NR}}|$ are given in nm, the shift parameter λ in kJ mol^{-1} nm^{-2}.

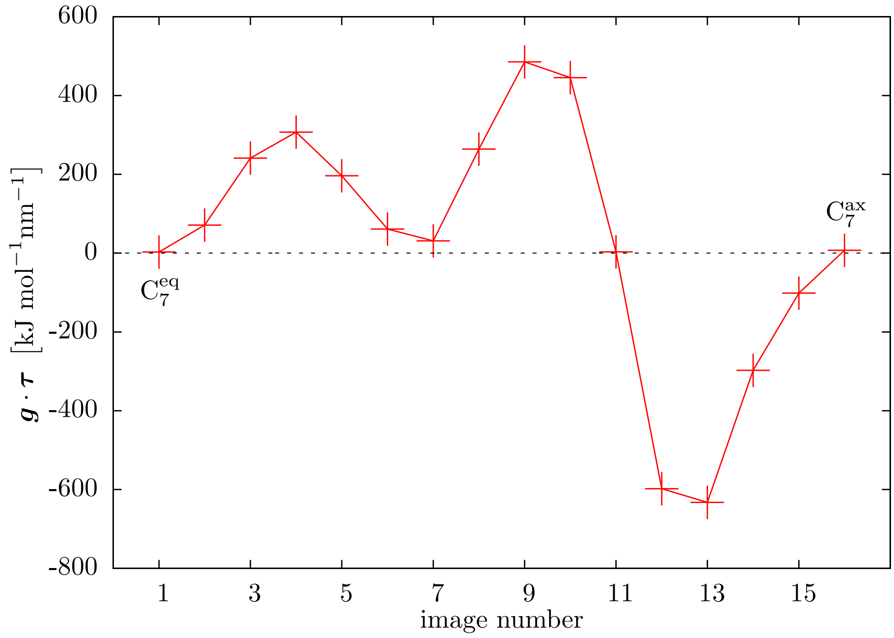

Figure 3.18: Gradient profile of the path between the minima C_7^{eq} and C_7^{ax} after convergence. The diagram shows the free energy gradient projected on to the tangent vector $\hat{\boldsymbol{\tau}}_i$ of each image. Image number 11 is a good estimates for the saddle point.

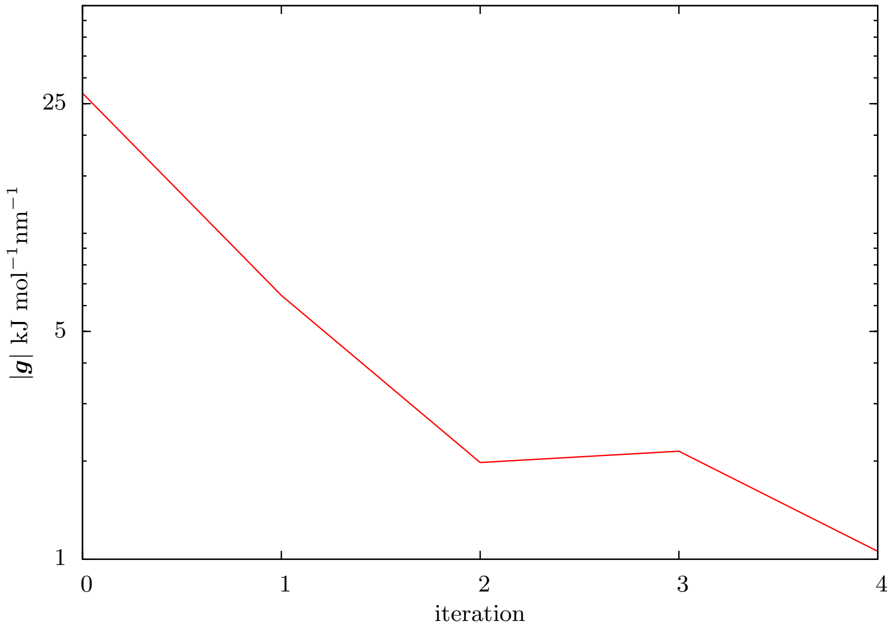

Figure 3.19: Newton–Raphson refinement to the saddle point at $\Phi = -1.43°$ and $\Psi = -68.36°$, starting from image 11 of the converged path between C_7^{eq} and C_7^{ax}. The fast convergence shows that image 11 is a good approximation for the saddle point.

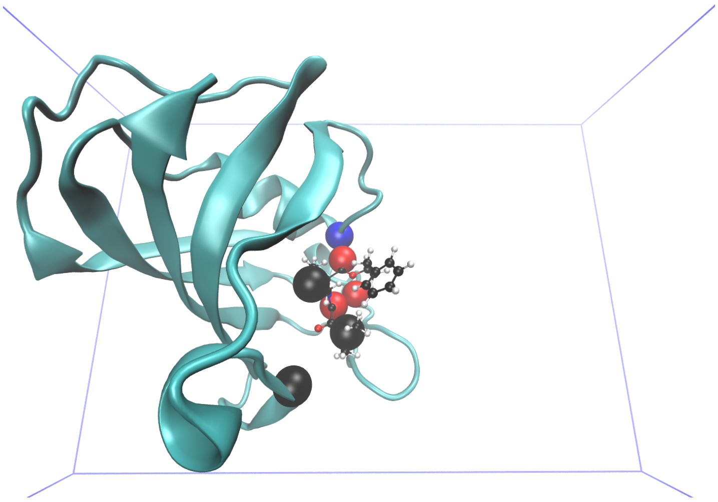

(a) Complex; ligand is bound to the protein

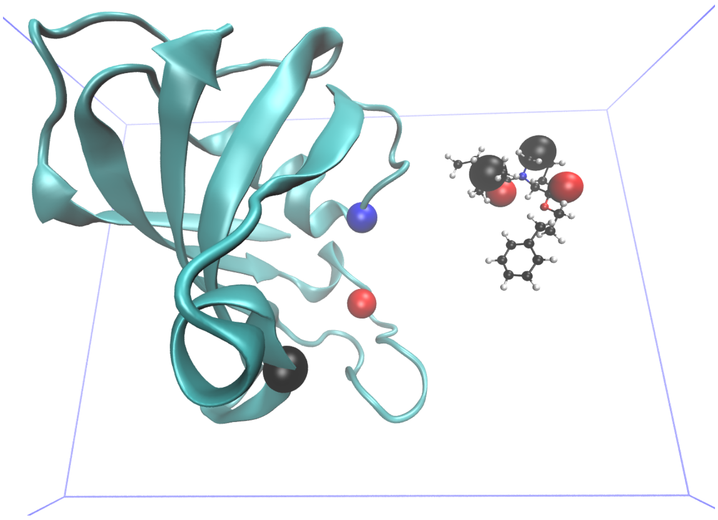

(b) Unbound state

Figure 3.20: Visualization of the investigated system. The receptor protein is illustrated in cartoon style, while the ligand is represented by a ball and stick model. The large balls indicate the seven atoms chosen to be in the reaction coordinate space (RCS). Blue lines indicate the edges of the water box. Graphic generated with the visualization tool VMD.[49]

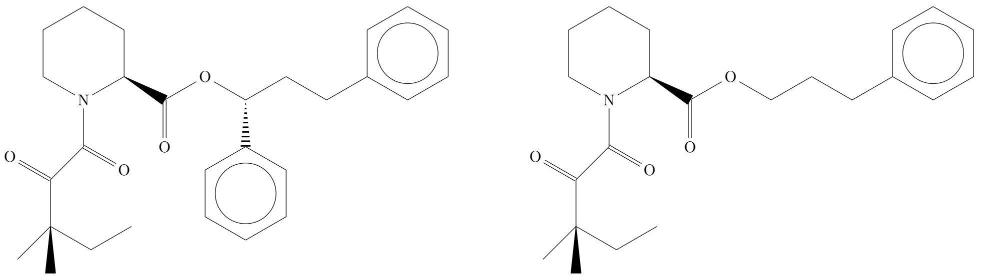

(a) *1,3 - diphenyl - 1 - propyl - 1 - (3,3 - dimethyl - 1,2 - dioxypentyl) - 2 - piperidine carboxylate.* Structure of ligand as found in the protein data base[68] in the structure file of the 1FKG complex[69, 70]

(b) *phenyl - 1 - propyl - 1 - (3,3 - dimethyl - 1,2 - dioxypentyl) - 2 - piperidine carboxylate* . Ligand used in this work

Figure 3.21: Structural formulas of ligands mentioned in this work. The structure (**b**) is generated by removing a phenyl group from the structure (**a**)

To test the concept for more relevant systems the binding of the ligand *phenyl - 1 - propyl - 1 - (3,3 - dimethyl - 1,2 - dioxypentyl) - 2 - piperidine carboxylate* with the human protein FKBP12 is investigated. The structure of this ligand is shown in figure 3.21b. This system was chosen because many studies on complexes including this protein were done before and can be used for comparison.[71–75] The initial configuration of the protein was taken from the complex found by X-ray studies of the crystal structure[69, 70] as it can be obtained from the protein database.[68] The structure for the ligand used in this work was generated by removing a phenyl group from the ligand *1,3 - diphenyl - 1 - propyl - 1 - (3,3 - dimethyl - 1,2 - dioxypentyl) - 2 - piperidine carboxylate* found in the 1FKG structure.[70] This ligands structure is illustrated in figure 3.21a

The system was placed in a 5.5 nm× 5.0 nm× 8.0 nm water box. The dimension in the Z-direction was set to a greater value in order to have space to pull the ligand out of the cavity. After minimization and equilibration the water box dimension relaxed to 5.62449 nm× 5.11318 nm× 8.18108 nm.

The AMBER99[76] force field is used for the protein and TIP3P[10] as water model, where the ligand was parameterized with the GAFF[77] force field using the software antechamber.[78] The Newton equations of motion are integrated using a velocity-Verlet integrator with a time step of 1 fs. The simulation is done with periodic boundary conditions in all dimensions. Electrostatic interactions are treated with a cut off of 1 nm for short range, and by way of particle mesh Ewald sum for long range interaction using a grid spacing of 0.135 nm. The Van-der-Waals force is cut off for interactions longer than 1.4 nm. The thermostat is a Nosé–Hoover chain[11–14] thermostat with a chain length of 4. Temperature is set to 300 K and pressure to 1.01325 bar. The pressure is controlled by a Martyna–Tuckerman–Tobias–Klein barostat.[79,80] The configuration of the unbound end image is visualized in figure 3.20.

In this work seven atoms are chosen to be in the RCS. Three belong to the receptor protein and four to the ligand. This choice is indicated by larger spheres in the visualisation of the whole system in figure 3.20.

The path to be observed is the route of the ligand into the binding pocket of the protein. As a preparation for the actual umbrella sampling simulations the complex of the ligand and the protein was formed and placed in the water box. The system was minimised and equilibrated. The resulting structure is used as the starting point for the construction of the initial guess of the path.

3.3.3.1 Construction of the initial path

The most crucial part of applying the method developed in this work to realistic systems is the definition of the initial path. Performing NEB optimisations using deterministic optimisation schemes the path will converge to the next local minima. Heuristic algorithms may be able to escape from the local pond to find global minima. The algorithm simulated annealing, for example, is applied to find the MEP of alanine dipeptide in literature.[81]

However, for optimisations within the free energy landscape, such global optimisations algorithms are computationally prohibitive. The initial path must therefore be placed within the area of convergence of the MFEP. If it is placed within the convergence area of a path leading over a less favorable saddle point, the iterations will not converge to the desired path. Worse, if parts of the images lie in the convergence radiuses of different paths, convergence can be unacceptably slow because many iterations will be needed until one path dominates over the other.

A naïve linear interpolation between the end points of an observed reaction often leads to energetically very unfavourable intermediate states. Recently a promising improvement for defining the initial path to carry out NEB optimisations within the potential energy landscape was made.[82] In this work more heuristic approaches defining the initial path are used.

Reminding the aim of the optimisations in this chapter is to describe the MFEP of ligand receptor binding. The end points of the path represent the complex on one side and a state with the ligand outside of the pocket on the other. To define the intermediate states of the initial guess two different approaches were carried out.

In a first attempt, a steered molecular dynamic simulation was used. Thereby a non physical force pulled the ligand away from the protein. A quadratic bias was applied, restraining the centre of mass of the ligand to a certain distance to the centre of mass of the protein. This was done in one run, while the distance was slowly increased. The parameters used for the steered MD simulation are the following: The spring force for the quadratic bias was 100 kJ mol^{-1}nm^{-1}, and pulling was done with a speed of 0.01 nm ps^{-1}. Every 1000$^{\text{th}}$ time step was written to disk. The resulting trajectory does not yield a linear path between bound complex and unbound state but rater configurations fluctuating around the aimed distances. To start with the most equally spaced path possible, the root mean square deviation (RMSD) of the seven atoms chosen to be in the RCS was plotted in figure 3.22. The range of RMSD was divided into 15 equally spaced intervals. The frames which match most to the intersection were used as images for the initial path. This procedure is illustrated in figure 3.22.

A second attempt to generate an initial path focuses on the RCS. For this a preliminary reaction coordinate Λ is chosen. Λ describes the progress along a linear interpolation of the RCS between two reference configurations A and B.

$$\boldsymbol{q}_{\Lambda}^{\mathrm{RCS}} = (\Lambda - 1)\boldsymbol{q}_{i,\mathrm{A}}^{\mathrm{RCS}} + \Lambda \boldsymbol{q}_{i,\mathrm{B}}^{\mathrm{RCS}}. \tag{3.68}$$

Here $\boldsymbol{q}_{\mathrm{A}}^{\mathrm{RCS}}$ refers to the coordinates of the RCS for the bound state configuration, and $\boldsymbol{q}_{\mathrm{B}}^{\mathrm{RCS}}$ are the coordinates of the RCS for the configuration with the ligand pulled out of the protein. The configurations A and B are the endpoints of the starting path gained by steered molecular dynamics as described above.

To construct the initial path 16 equally spaced values for $\Lambda = \{0, 0.0625, 0.125, \ldots, 1.0\}$ were chosen. For each value of Λ a molecular dynamics run with the additional bias

$$w_{\Lambda}(\boldsymbol{q}^{\mathrm{RCS}}) = \frac{k_{\Lambda}}{2}\left(\boldsymbol{q}^{\mathrm{RCS}}(t) - \boldsymbol{q}_{\Lambda}^{\mathrm{RCS}}\right)^2 \tag{3.69}$$

was executed. k_{Λ} was set to 1000 kJ mol^{-1}nm^{-2}. This bias can be applied using the position restraints algorithm of GROMACS[66] and does not require any further modification of the molecular dynamics code. For each Λ value the configuration

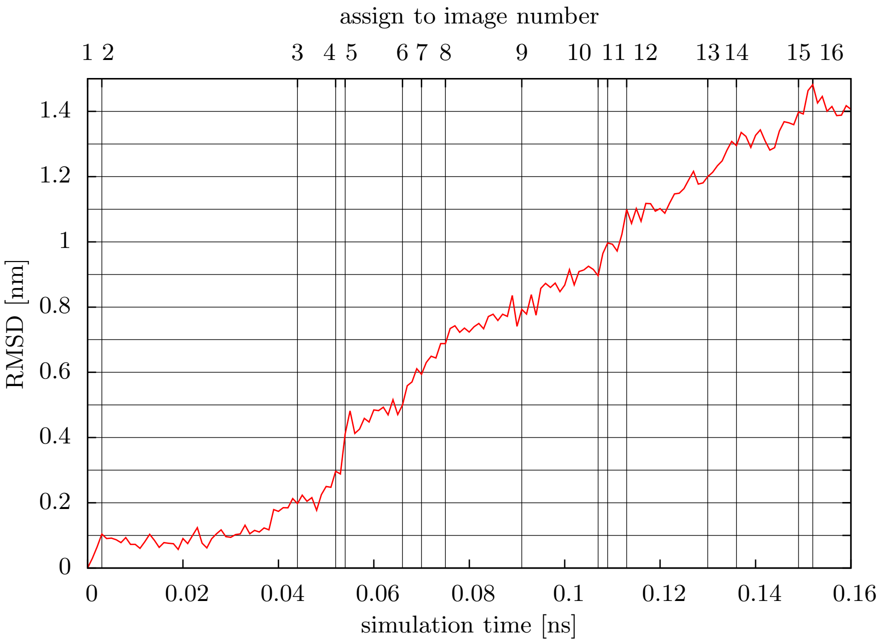

Figure 3.22: Illustration of the construction of the initial path from the steered dynamics run. The graph shows the root mean square deviation (RMSD) of the atoms belonging to the RCS of a steered molecular dynamics run. The range of RMSD was divided into 15 equally spaced intervals (horizontal lines). The frames matching best to the desired RMSD values are assigned to the corresponding images of the initial path (vertical lines).

after 100000 steps was used as an image of the initial path. In the following this work refers to the path gained this way as the initial path gained by position restrains.

3.3.3.2 Calculations

Comparative Umbrella Integration

To compare the results with an established method, comparative calculations of one-dimensional umbrella integration[16,33,34] are performed. The reaction coordinate χ was defined to be the distance of the centre of mass of the protein and the centre of mass of the ligand. This definition is included in the GROMACS package and can be used for umbrella sampling without modification of the code.

A quadratic bias of the form $w_\mathrm{b} = \frac{k}{2}(\chi - \chi_\mathrm{ref})^2$ with $k = 1000$ kJ mol^{-1}nm^{-2} is used for all windows, while the reference coordinates χ_ref are located at positions spaced by about 0.1 nm. At each window moleculardynamics simulations of 1 ns with a time step of 1 fs are performed. Every 10$^\mathrm{th}$ step is used for the umbrella integration analysis while the first 40 ps are omitted in order to avoid non-equilibrium artifacts. However, since the specifities of the GROMACS software require biased molecular dynamics simulations to be started at a configuration with the reaction coordinate $\chi = \chi_\mathrm{ref}$, these configurations have to be generated before the actual umbrella sampling run. Doing this carefully, the simulations start with already well equilibrated configurations. As a consequence, the number of omitted steps at the beginning of the simulations do not show a significant effect.

The close distance of the umbrella sampling windows assures a wide overlap of neighbouring windows. Reliable results could also be gained by using less sampling time. The addressed points yield some space for optimisation. Recalling, that umbrella integration is an established technique and not the objective of this work, the author chose to play safe in order to get a reliable profile to compare with his own work.

Comparing the profile gained by umbrella integration with those from NEB optimisations, raises the problem that reaction coordinates are measured in different ways. The comparative umbrella integration studies use the distance of the centre of mass of the protein and the ligand called χ in the following. For natural configurations this is never zero. It is different for the NEB optimisations. Here the reaction coordinate for image i is defined as

$$\xi_i = \sum_{k=2}^{i} \left| \boldsymbol{q}_{k-1}^\mathrm{RCS} - \boldsymbol{q}_k^\mathrm{RCS} \right| \tag{3.70}$$

In other words, ξ_i is simply the length within the RCS of the path from the first to the i^th image. Therefore ξ_0 is necessarily zero. To get some visual comparative graphs the centre of mass distances between protein and ligand, of the first (χ_0) and last (χ_{N-1}) image of NEB chain are calculated. Here the path of the last optimisation iteration was used. For plotting the χ values of the intermediate images are approximated by

$$\chi_i \approx \frac{\chi_{N-1} - \chi_o}{\xi_{N-1}} \xi_i + \chi_0. \tag{3.71}$$

Even if the actual χ_i^real values of the configurations are easily calculated, the author chose this linear relation in order not to disturb the character of the NEB profiles. Selected scaled NEB profiles are plotted together with the profile gained by the established umbrella integration techniques in figure 3.24 and 3.25. Details are discussed in the following.

Results

For no parameter set NEB optimisations in the free energy landscape converged to reasonable free energy profiles. I therefore discuss a representative case at this point. Many other parameters were tried, but no qualitatively different behavior was visible. Starting from the path gained by position restrains, the NEB force is significantly smaller in the first steps. However, in this case the path does not converge either.

The parameters of the illustrated examples are the following: 16 images are used to approximate the path, the NEB spring constant is 0.001 in atomic units (≈ 937.583 kJ mol^{-1} nm^{-2}) the maximal step length $d_{\text{max}} = 0.05$ nm and the umbrella sampling bias is set to 0.05 atomic units (≈ 46879.15 kJ mol^{-1} nm^{-2}). The convergence behavior is shown in figure 3.23. Even for much longer runs the convergence criterion is never met. At iteration 15 a peak of the NEB force is observed. In figure 3.24 free energy profiles from the iterations before this peak are compared with the profile calculated by one-dimensional umbrella integration technique. NEB profiles are calculated by summing up the projection of the gradient on to the local tangent vector, $A(\xi_i) = \sum_{k=2}^{i} \tilde{\boldsymbol{g}}_k \cdot \boldsymbol{\tau}_k$. To get comparable graphs the reaction coordinate of the NEB profiles are scaled according to equation (3.71). In order not to confuse the reader's eye, only profiles of each second NEB iteration are plotted.

In figure 3.25 the same comparison is done for the iterations up from iteration 15. We clearly observ that the peak corresponds to a qualitative change of the path. Before iteration 14 the path has a monotonic characteristic. After iteration 15 a minimum at the 8$^{\text{th}}$ image ($\chi \approx 1.5$) appears. This minimum is caused by hydrophobic binding of the ligand's phenyl group with residues of the protein. The minimum configuration is shown in figure 3.26. Even after many iterations the profile still changes a lot and does not reproduce the profile gained by the one-dimensional umbrella integration.

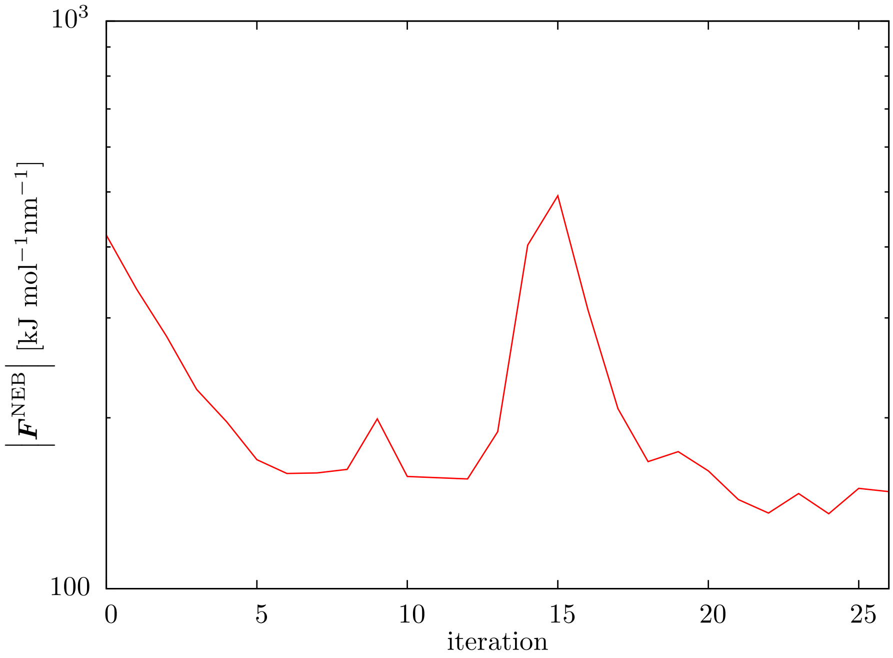

Figure 3.23: Convergence of nudged elastic band optimisations for the complex ligand system. While at the beginning the nudged elastic band force significantly decreases, convergence is not observed. The peak at iteration 15 represents an qualitative change of the path.

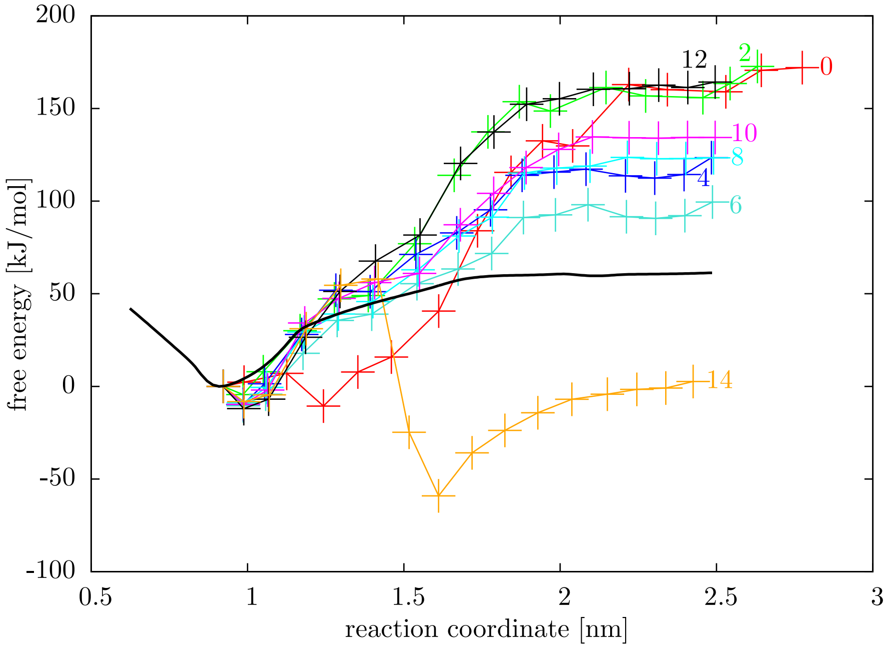

Figure 3.24: Free energy profile at different iterations. To avoid confusion, the plot only contains every second iteration before the iteration 15, which represents a reordering of the path. Crosses represent the actual positions of the images, while the thick black line shows the profile gained by one-dimensional umbrella integration. For the latter the reaction coordinate is the protein ligand center of mass distance. In order to compare profiles gained from NEB optimisations and umbrella integration, the reaction coordinate of the NEB profiles is scaled according to equation (3.71).

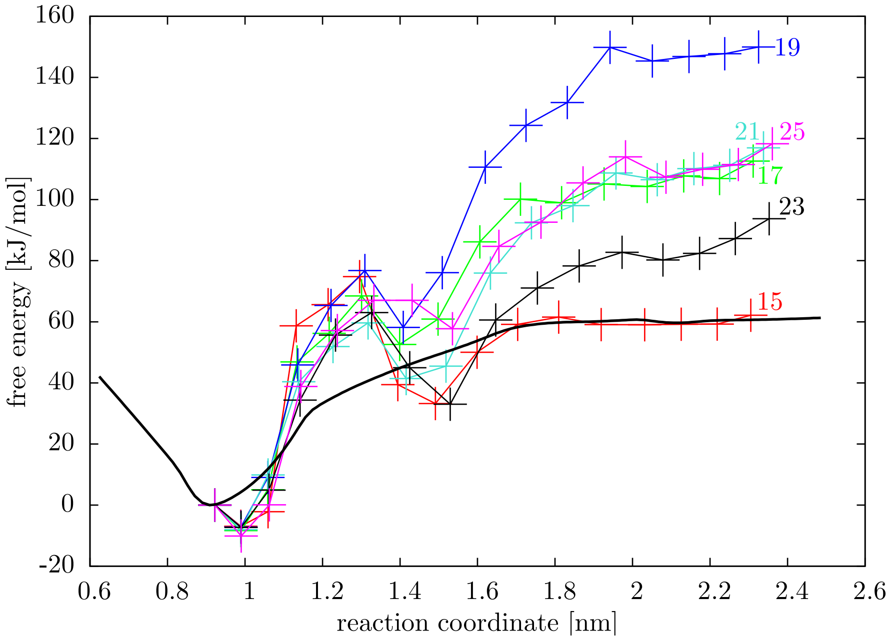

Figure 3.25: Free energy profile at different iterations. To avoid confusion, the plot just contains every second iteration up from iteration 15 which represents a reordering of the path. Crosses represent the actual positions of the images, while the thick black line shows the profile gained by one-dimensional umbrella integration. For the latter, the reaction coordinate is the protein ligand centre of mass distance. In order to compare profiles gained from NEB optimisations and umbrella integration the reaction coordinate of the NEB profiles is scaled according to equation (3.71).

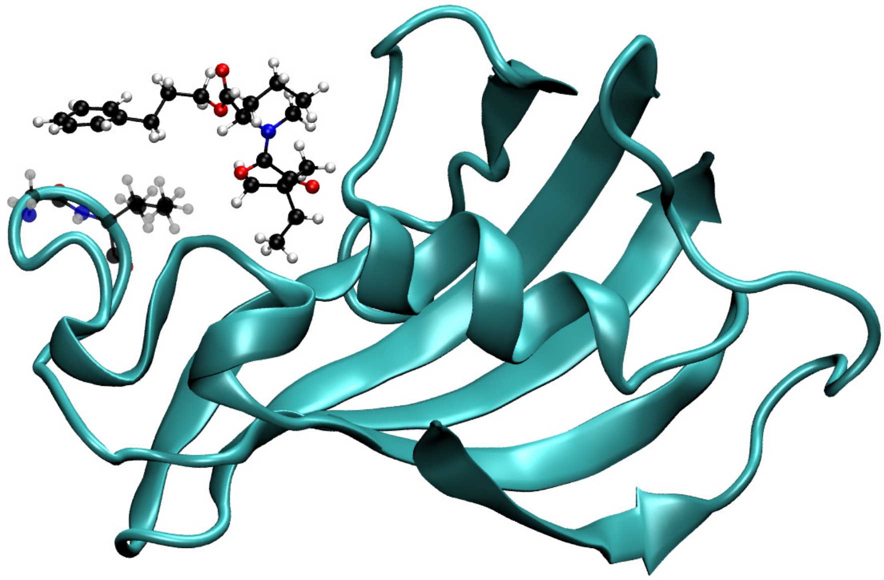

Figure 3.26: Intermediate minimum structure at iteration 15. The ligand's phenyl group hydrophobically interacts with residues of the protein which are illustrated in grayed colours. Graphic generated with the visualization tool VMD.[49]

4

CONCLUSIONS AND OUTLOOK

This chapter draws conclusions and discusses future development

Contents

4.1 Conclusion

The main task of computational chemistry is to find reaction mechanisms. Such a mechanism can be described as a minimum free energy path (MFEP) in the reaction coordinate space RCS, which consists of the coordinates of the atoms playing an important roll during the reaction. Unfortunately, the free energy surface, which includes statistical information of all atoms not included in the RCS, is not directly accessible. This work uses umbrella integration,[16,33,34] to calculate gradients and Hessians from biased molecular dynamics simulations, so-called umbrella sampling. In the first part these values are used for an iterative search of saddle points. The MFEP is then constructed by following the gradient down to the minima. This procedure has the drawbacks that it needs good guesses for the saddle points to start because of the small convergence radius of the Newton–Raphson method and that is inherently serial. Each step is based on information gained by the previous one.

To overcome these drawbacks, in the second part of the results chapter a Newton–Raphson scheme for nudged elastic band NEB optimisations is developed which uses gradients and Hessians of the underlying potential. NEB optimisations start from an initial guess of the path, discretize it in a number of conformations (images) and iteratively approach the minimum energy path (MEP). In the free energy surface gradients and Hessians can be obtained by umbrella integration. At each conformation independent umbrella sampling simulations have to be done. This makes the method intrinsically parallel. In addition it is usually easier to find good guesses for a reaction path than for the saddle points. The proof of concept is done by applying the method to the well studied system of alanine dipeptide.

The algorithm depends on the non-physical parameters bias for umbrella sampling simulation, spring force and maximal step length. Successful optimisations with simple systems imply that, while the bias of the molecular dynamics simulations seems to be less problematic, spring force and maximal step length have crucial influences on the convergence. Weak spring forces lead to an unequal distribution of the images while strong spring forces reduce the convergence radius of the Newton–Raphson method. Small values for the maximal step length slow down the convergence while large values may lead to faster convergence but increase the danger of leaving the convergence radius. Here further methodical work is required.

The choice of the initial path is in general very crucial for the convergence for any NEB optimisation. This work could only archive convergence from initial paths gained by linear interploation of Cartesian coordinates for the simple test systems of the Müller–Brown potential and the reordering of a two-dimensional Lennard–Jones cluster. However, in the case of the Lennard–Jones cluster, only if the interpolation was done between all known local minima. For optimisation within the free energy surface of alanine dipeptide a linear interpolation of the torsion angles was necessary.

As a system with realistic complexity the binding of FKBP-type peptidyl-prolyl cis-trans isomerase with a ligand is performed. Unfortunately, the convergence properties of the NEB optimisation were unsatisfactory. There may exist a range of parameter sets for which convergence may be archived; different choice of the RCS may be useful. However, to achieve the aim of the overall project to develop a method which can be used generally to find intrinsic reaction coordinates with little or no previous knowledge of the particular system further work is required.

To make the method applicable for realistic systems it would be necessary to develop a systematic way of either determining good parameters or finding better initial paths. Experience so far implies that the second point has more potential. However, even if good parameters and initial paths are available, it is still questionable if the method could be used competitively. First, because the necessary sampling time increases quadratically when approaching the minima, and at secondly because approaching the minima in small steps may lead to an oversampling of areas of little interest.

4.2 Outlook

In this work an algorithm to find the MFEP using umbrella integration and NEB optimisations was developed. Unfortunately, for a system with realistic complexity optimisations failed to converge to a final path. Using the algorithm for a less complex system already showed that the choice of certain parameters has a crucial impact on convergence of the algorithm. Further work may develop systematic approaches to determine these parameters, and to achieve convergence for realistic systems as well.

Another crucial condition for convergence is the initial path. Further work may develop reliable methods to find initial paths within the convergence area of the method. Then the method developed in this work could probably serve for refinement of the intrinsic reaction coordinate.

The Newton–Raphson based optimiser developed in this work, which shows quadratic convergence for NEB calculations in the potential energy surface, relies on the gradient and Hessians at each step at each window of the chain of states. While the Hessians do not require more computational effort in the case of umbrella integration, Hessians of the potential energy may become unreasonably costly. Further work will use this optimiser to find the MEP of realistic systems, but in combination with updated Hessians. In doing so, the author does perhaps not expect quadratic convergence, but still a significant improvement over established methods for NEB optimisation.

In this work it was shown that removing translational components from the NEB optimisation step yields important improvement for convergence. Also Excluding the rotational part from the step promises further improvements to this work.

Part III

APPENDIX

5

ACKNOWLEDGEMENTS

Reaching the point where not much is left to tell, it surprises me that this section turns out to be the most difficult one to write. Although I often have to use the first person singular or some paraphrases of it for grammatical reasons, no single idea or individual operation in this work would have been possible without the groundwork and inspiration of others. The discussions I had with colleges and friends, the comfort, support and the time that friends, family and colleagues have given me are indispensable for anybody to complete such a work. It seems impossible to mention all persons I am indebted to. Please accept my apologies if you do not find your contribution sufficiently recognized in the following paragraphs.

At first I have to thank the Deutsche Forschungsgesellschaft for financing my project through the special research center SFB 716 at the University of Stuttgart. In particular I thank Prof. Johannes Kästner, not only for mentoring my thesis, but also for the confidence of assigning the project to me. The whole work was carried out and was only possible in very close cooperation with him. It is surely courageous to invest time and money in an unknown graduate from another faculty. I hope he found something useful in this lucky bag.

Special thanks to Prof. Dr. Bernd Engels for taking over the responsibility of being the second examiner and to Prof. Dr. Joris van Slageren for being the exam's chairman.

Besides the very inspiring discussions during lunch and tea time with all institute members, I want to mention Judith and Jan by name for helping me in areas where my mathematical and chemical knowledge came up against its limitations. I was lucky to benefit from a very inspiring work style in the group of Dr. Marcelo Martí at the University of Buenos Aires. They gave me a very different idea of what it means to work creatively and scientifically. Unfortunately, I only got to know them during the last part of the project. I am also thankful for many favours, which were done for me and good glasses of wines provided by Max, Laura and Laszlo.

I thank my parents for giving me the opportunity to study. They laid the foundations on which I could build up my knowledge and abilities. Although our ways are now spread more and more over the world, I would not have been able to get to the point where I am without the company of my study group from my student days. Thank you to my friends and all residents of the “orangene Rita” for the time and parties we had together. Art is also very important to endure the absurdism we face every day. Besides the work of countless artists I have been able to enjoy in the last few years I especially have to thank those people like Violeta, Antonio, Melanie, Tina and others who spent their time to actively make music with me.

Matthias Bohner

Stuttgart, Germany, 19th January 2015

BIBLIOGRAPHY

[1] K. Fukui. The path of chemical reactions – the IRC approach. *Acc. Chem. Res*, 14:363, 1981.

[2] K. Fukui. Variational principles in a chemical reaction. *Int. J. Quantum Chem.*, 20:633, 1981.

[3] R. D. Ruth. A canonical integration technique. *IEEE Trans. Nucl. Sci*, 30(4):2669, 1983.

[4] P. J. Channell and C. Scovel. Symplectic integration of hamiltonian systems. *Nonlinearity*, 3(2):231, 1990.

[5] H. Yoshida. Construction of higher order symplectic integrators. *Phys. Lett. A*, 150(5):262, 1990.

[6] S. Toxvaerd. Molecular dynamics at constant temperature and pressure. *Phys. Rev. E*, 47(1):343, 1993.

[7] S. Toxvaerd, O. J. Heilmann, and J. C. Dyre. Energy conservation in molecular dynamics simulations of classical systems. *J. Chem. Phys.*, 136:224106, 2012.

[8] A. D. MacKerell Jr., D. Bashford, R. L. Bellott, R. L. Dunbrack Jr., J. D. Evanseck, M. J. Field, S. Fischer, J. Gao, H. Guo, S. Ha, D. Joseph-McCarthy, L. Kuchnir, K. Kuczera, F. T. K. Lau, C. Mattos, S. Michnick, T. Ngo, D. T. Nguyen, B. Prodhom, W. E. Reiher III, B. Roux, M. Schlenkrich, J. C. Smith, R. Stote, J. Straub, M. Watanabe, J. Wiorkiewicz-Kuczera, D. Yin, and M. Karplus. All-atom empirical potential for molecular modeling and dynamics studies of proteins. *J. Phys. Chem. B*, 102:3586, 1998.

[9] W. D. Cornell, P. Cieplak, C. I. Bayly, I. R. Gould, K. M. Merz, D. M. Ferguson, D. C. Spellmeyer, T. Fox, J. W. Caldwell, and P. A. Kollman;. A second generation force field for the simulation of proteins, nucleic acids and organic molecules. *J. Am. Chem. Soc.*, 117(19):5179–5197, 1995.

[10] W. L. Jorgensen, J. Chandrasekhar, J. D. Madura, R. W. Impey, and M. L. Klein. Comparison of simple potential functions for simulating liquid water. *J. Chem. Phys.*, 79:926, 1983.

[11] S. Nosé. A unified formulation of the constant temperature molecular dynamics methods. *J. Chem. Phys.*, 81:511, 1984.

[12] S. Nosé. A molecular dynamics method for simulations in the canonical ensemble. *Mol. Phys.*, 52:255, 1984.

[13] W. G. Hoover. Canonical dynamics: Equilibrium phase-space distributions. *Phys. Rev. A*, 31:1695, 1985.

[14] G. J. Martyna, M. L. Klein, and M. Tuckerman. Nosé–hoover chains: The canonical ensemble via continuous dynamics. *J. Chem. Phys.*, 97:2635, 1992.

[15] J. G. Kirkwood. Statistical mechanics of fluid mixtures. *J. Chem. Phys.*, 3:300, 1935.

[16] J. Kästner. Umbrella integration in two or more reaction coordinates. *J. Chem. Phys.*, 131:034109, 2009.

[17] Y. Zhang, H. Liu, and W. Yang. Free energy calculation on enzyme reactions with an efficient iterative procedure to determine minimum energy paths on a combined ab initio QM/MM potential energy surface. *J. Chem. Phys.*, 112:3483, 2000.

[18] B. Ensing, A. Laio, F. L. Gervasio, M. Parrinello, and M. L. Klein. A minimum free energy reaction path for the e2 reaction between fluoro ethane and a fluoride ion. *J. Am. Chem. Soc.*, 126:9492, 2004.

[19] P. Fleurat-Lessard and T. Ziegler. Tracing the minimum-energy path on the free-energy surface. *J. Chem. Phys.*, 123:084101, 2005.

[20] L. Maragliano, A. Fischer, E. Vanden-Eijnden, and G. Ciccotti. String method in collective variables: Minimum free energy paths and isocommittor surfaces. *J. Chem. Phys.*, 125:024106, 2006.

[21] I. V. Khavrutskii, K. Arora, and C. L. Brooks III. Harmonic fourier beads method for studying rare events on rugged energy surfaces. *J. Chem. Phys.*, 125:174108, 2006.

[22] H. Hu, Z. Lu, and W. Yang. Qm/mm minimum free-energy path: Methodology and application to triosephosphate isomerase. *J. Chem. Theory Comput.*, 3:390, 2007.

[23] L. Maragliano and E. Vanden-Eijnden. On-the-fly string method for minimum free energy paths calculation. *Chem. Phys. Lett.*, 446:182, 2007.

[24] H. Hu, Z. Lu, J. M. Parks, S. K. Burger, and W. Yang. Quantum mechanics/molecular mechanics minimum free-energy path for accurate reaction energetics in solution and enzymes: Sequential sampling and optimization on the potential of mean force surface. *J. Chem. Phys.*, 128:034105, 2008.

[25] B. H. Mahan. Activated complex theory of bimolecular reactions. *J. Chem. Edu.*, 51(11):709, 1974.

[26] A. Arnaldsson. *Calculation of quantum mechanical rate constants directly from ab initio atomic forces.* PhD thesis, University of Washington, 2007.

[27] R. H. Swendsen and J. Wang. Replica monte carlo simulation of spin-glasses. *Phys. Rev. Lett.*, 57:2607, Nov 1986.

[28] A. Amadei, A. B. M. Linssen, B. L. De Groot, D. M. F. Van Aalten, and H. J. C. Berendsen. An efficient method for sampling the essential subspace of proteins. *J. Biomol. Struct. Dyn.*, 13(4):615, 1996.

[29] G. M. Torrie and J. P. Valleau. Nonphysical sampling distributions in monte carlo free-energy estimation: Umbrella sampling. *J. Comput. Phys.*, 23:187–199, 1977.

[30] A. Laio and M. Parrinello. Escaping free-energy minima. *Proc. Natl. Acad. Sci. U.S.A.*, 99:12562–12566, 2002.

[31] C. Dellago, P. G. Bolhuis, and D. Chandler. Efficient transition path sampling: Application to lennard-jones cluster rearrangements. *J. Chem. Phys.*, 108:9236, 1998.

[32] P. G. Bolhuis, D. Chandler, C. Dellago, and P. L. Geissler. Transition path sampling: Throwing ropes over rough mountain passes, in the dark. *Ann. Rev. Phys. Chem.*, 53:291, 2002.

[33] J. Kästner and W. Thiel. Bridging the gap between thermodynamic integration and umbrella sampling provides a novel analysis method: "umbrella integration". *J. Chem. Phys.*, 123:144104, 2005.

[34] J. Kästner and W. Thiel. Analysis of the statistical error in umbrella sampling simulations by umbrella integration. *J. Chem. Phys.*, 124:234106, 2006.

[35] J. Kästner. Umbrella integration with higher-order correction terms. *J. Chem. Phys.*, 136:234102, 2012.

[36] M. U. Bohner and J Kästner. An algorithm to find minimum free-energy paths using umbrella integration. *J. Chem. Phys.*, 137:034105, 2012.

[37] H. Jónsson, G. Mills, and K. W. Jacobsen. *Classical and Quantum Dynamics in Condensed Phase Simulations*, chapter Nudged Elastic Band Method for Finding Minimum Energy Paths of Transitions, page 385. World Scientific, 1998.

[38] G. Henkelman and H. Jónsson. Improved tangent estimate in the nudged elastic band method for finding minimum energy paths and saddle points. *J. Chem. Phys.*, 113:9978, 2000.

[39] G. Henkelman, B. P. Uberuaga, and H. Jónsson. A climbing image nudged elastic band method for finding saddle points and minimum energy paths. *J. Chem. Phys.*, 113:9901, 2000.

[40] J.-W. Chu, B. L. Trout, and B. R. Brooks. A super-linear minimization scheme for the nudged elastic band method. *J. Chem. Phys.*, 119:12708, 2003.

[41] P. Plessow. Reaction path optimization without neb springs or interpolation algorithms. *J. Chem. Theory Comput.*, 9:1305–1310, 2013.

[42] W. E, W. Ren, and E. Vanden-Eijnden. String method for the study of rare events. *Phys. Rev. B*, 66:052301, 2002.

[43] B. Peters, A. Heyden, A. T. Bell, and A. Chakraborty. A growing string method for determining transition states: Comparison to the nudged elastic band and string methods. *J. Chem. Phys.*, 120:7877, 2004.

[44] S. K. Burger and W. Yang. Quadratic string method for determining the minimum-energy path based on multiobjective optimization. *J. Chem. Phys.*, 124:054109, 2006.

[45] S. Fischer and M. Karplus. Conjugate peak refinement : an algorithm for finding reaction paths and accurate transition states in systems with many degrees of freedom. *Chem. Phys. Lett.*, 194:252, 1992.

[46] N. Gonzalez-Garcia, J. Pu, A. Gonzalez-Lafont, J. M. Lluch, and D. G. Truhlar. Searching for saddle points by using the nudged elastic band method: An implementation for gas-phase systems. *J. Chem. Theory Comput.*, 2:895, 2006.

[47] I. T. Todorov, W. Smith, K. Trachenko, and M. T. Dove. Dl_poly_3: new dimensions in molecular dynamics simulations via massive parallelism. *J. Mat. Chem.*, 16(20):1911, 2006.

[48] P. Sherwood, A. H. de Vries, M. F. Guest, G. Schreckenbach, C. R. A. Catlow, S. A. French, A. A. Sokol, S. T. Bromley, W. Thiel, A. J. Turner, S. Billeter, F. Terstegen, S. Thiel, J. Kendrick, S. C. Rogers, J. Casci, M. Watson, F. King, E. Karlsen, M. Sjøvoll, A. Fahmi, A. Schäfer, and C. Lennartz. Quasi: A general purpose implementation of the qm/mm approach and its application to problems in catalysis. *J. Mol. Struct. (THEOCHEM)*, 632:1, 2003.

[49] W. Humphrey, A. Dalke, and K. Schulten. Vmd: visual molecular dynamics. *J. of mol. Graph.*, 14(1):33, 1996.

[50] J. Kästner, J. M. Carr, T. W. Keal, W. Thiel, A. Wander, and P. Sherwood. DL-FIND: an open-source geometry optimizer for atomistic simulations. *J. Phys. Chem. A*, 113:11856, 2009.

[51] S. Metz and W. Thiel. A combined qm/mm study on the reductive half-reaction of xanthine oxidase: Substrate orientation and mechanism. *J. Am. Chem. Soc.*, 131:14885–14902, 2009.

[52] T. P. M. Goumans, C. R. A. Catlow, W. A. Brown, J. Kästner, and P. Sherwood. An embedded cluster study of the formation of water on interstellar dust grains. *Phys. Chem. Chem. Phys.*, 11:5431, 2009.

[53] J. Kästner and P. Sherwood. The ribosome catalyses peptide bond formation by providing high ionic strength. *Mol. Phys.*, 108:293, 2010.

[54] J. B. Rommel, T. P. M. Goumans, and J. Kästner. Locating instantons in many degrees of freedom. *J. Chem. Theory Comput.*, 7:690, 2011.

[55] J. Rommel, Y. Liu, H.-J. Werner, and J. Kästner. Role of tunneling in the enzyme glutamate mutase. *J. Phys. Chem. B*, 116:13682, 2012.

[56] J. Kästner. The path length determines the tunneling decay of substituted carbenes. *Chem. Eur. J.*, 19:8207–8212, 2013.

[57] J. Nocedal. Updating quasi-newton matrices with limited storage. *Math. Comput.*, 35:773, 1980.

[58] D. C. Liu and J. Nocedal. On the limited memory bfgs method for large scale optimization. *Math. Program.*, 45:503, 1989.

[59] D. Sheppard, R. Terrell, and G. Henkelman. Optimization methods for finding minimum energy paths. *J. Chem. Phys.*, 128:134106, 2008.

[60] E. Süli and D. F. Mayers. *An introduction to numerical analysis.* Cambridge university press, 2003.

[61] K. Müller and L. D. Brown. Location of saddle points and minimum energy paths by a constrained simplex optimization procedure. *Theor. Chim. Acta*, 53:75, 1979.

[62] M. U. Bohner, J. Zeman, J. Smiatek, A. Arnold, and J. Kästner. Nudged-elastic band used to find reaction coordinates based on the free energy. *J. Chem. Phys.*, 140(7):074109, 2014.

[63] D. W. Marquardt. An algorithm for least-squares estimation of nonlinear parameters. *J. SIAM*, 11(2):431, 1963.

[64] M. U. Bohner, J. Meisner, and J. Kästner. A quadratically-converging nudged elastic band optimizer. *J. Chem. Theory Comput.*, 9:3498–3504, 2013.

[65] M. Hanke-Bourgeois. *Grundlagen der numerischen Mathematik und des wissenschaftlichen Rechnens*, volume 1. Teubner Stuttgart, 2002.

[66] B. Hess, C. Kutzner, D. Van Der Spoel, and E. Lindahl. Gromacs 4: Algorithms for highly efficient, load-balanced and scalable molecular simulation. *J. Chem. Theory Comp.*, 4(3):435, 2008.

[67] M. Bonomi, D. Branduardi, G. Bussi, C. Camilloni, D. Provasi, P. Raiteri, D. Donadio, F. Marinelli, F. Pietrucci, R. A. Broglia, and M. Parrinello. Plumed: A portable plugin for free-energy calculations with molecular dynamics. *Comp. Phys. Com.*, 180(10):1961 – 1972, 2009.

[68] http://www.rcsb.org/pdb/.

[69] D. A. Holt, J. I. Luengo, D. S. Yamashita, H. Oh, A. L. Konialian, H. Yen, L. W. Rozamus, M. Brandt, M. J. Bossard, M. A. Levy, D. S. Eggleston, J. Liang, L. W. Schultz, T. J. Stout, and J. Clardy. Design, synthesis and kinetic evaluation of high-affinity FKBP ligands and the x-ray crystal structures of their complexes with FKBP12. *J. Am. Chem. Soc.*, 115:9925, 1993.

[70] DOI:10.2210/pdb1fkg/pdb.

[71] M. L. Lamb, J. Tirado-Rives, and W. L. Jorgensen. Estimation of the binding affinities of fkbp12 inhibitors using a linear response method. *Bio. Med. Chem.*, 7(5):851, 1999.

[72] J. M. J. Swanson, R. H. Henchman, and J. A. McCammon. Revisiting free energy calculations: A theoretical connection to MM/PBSA and direct calculation of the association free energy. *Biophysical Journal*, 86:67, 2004.

[73] H. Fujitani, Y. Tanida, M. Ito, G. Jayachandran, C. D. Snow, M. R. Shirts, E. J. Sorin, and V. S. Pande. Direct calculation of the binding free energies of fkbp ligands. *J. Chem. Phys.*, 123:084108, 2005.

[74] J. Wang, Y. Deng, and B. Roux. Absolute binding free energy calculations using molecular dynamics simulations with restraining potentials. *Biophys. J.*, 91:2798, 2006.

[75] F. M. Ytreberg. Absolute FKBP binding affinities obtained via nonequilibrium unbinding simulations. *J. Chem. Phys.*, 130:164906, 2009.

[76] J. Wang, P. Cieplak, and P. A. Kollman. How well does a restrained electrostatic potential (resp) model perform in calculating conformational energies of organic and biological molecules? *J. Comp. Chem.*, 21(12):1049, 2000.

[77] J. Wang, R. M. Wolf, J. W. Caldwell, P. A. Kollman, and D. A. Case. Development and testing of a general amber force field. *J. Comp. Chem.*, 25(9):1157, 2004.

[78] J. Wang, W. Wang, P. A. Kollman, and D. A. Case. Automatic atom type and bond type perception in molecular mechanical calculations. *J. Mol. Graph. Mod.*, 25(2):247, 2006.

[79] G. J. Martyna, D. J. Tobias, and M. L. Klein. Constant pressure molecular dynamics algorithms. *J. Chem. Phys.*, 101:4177, 1994.

[80] G. J. Martyna, M. E. Tuckerman, D. J. Tobias, and M. L. Klein. Explicit reversible integrators for extended systems dynamics. *Mol. Phys.*, 87(5):1117, 1996.

[81] C. Bergonzo, A. J. Campbell, R. C. Walker, and C. Simmerling. A partial nudged elastic band implementation for use with large or explicitly solvated systems. *Int. J. Quant Chem.*, 109(15):3781, 2009.

[82] S. Smidstrup, A. Pedersen, K. Stokbro, and H. Jónsson. Improved initial guess for minimum energy path calculations. *J. Chem. Phys.*, 140(21):214106, 2014.

List of Figures

5.0 Publications

Scientific articles where the author was invoked:

- M. U. Bohner and J. Kästner, *An algorithm to find minimum free-energy paths using umbrella integration*, J. Chem. Phys. **137**, 034105, (2012)
- M. U. Bohner, J. Meisner and J. Kästner, *A Quadratically-Converging Nudged Elastic Band Optimizer*, J. Chem. Theory Comput. **9** 3498, (2013)
- M. U. Bohner, J. Zeman, J. Smiatek, A. Arnold, and J. Kästner, *Nudged-elastic band used to find reaction coordinates based on the free energy*, J. Chem. Phys. **140**, 074109 (2014)

Erklärung über die Eigenständigkeit der Dissertation

Ich versichere, dass ich die vorliegende Arbeit mit dem Titel *Using Umbrella Integration to Find Minimum Free Energy Paths* selbständig verfasst und keine anderen als die angegebenen Quellen und Hilfsmittel benutzt habe; aus fremden Quellen entnommene Passagen und Gedanken sind als solche kenntlich gemacht.

Declaration of Authorship

I hereby certify that the dissertation entitled *Using Umbrella Integration to Find Minimum Free Energy Paths* is entirely my own work except where otherwise indicated. Passages and ideas from other sources have been clearly indicated.

Name/Name: Matthias Ulrich Bohner

Unterschrift/Signed: ______________________________

Datum/Date: 19th January 2015